





รายงายวิจัยฉบับสมบูรณ์

โครงการผลกระทบเนื่องจากสนามแม่เหล็กป^{ั่}นป่วนในตัวกลางระหว่างดาวเคราะห์ต่อการเคลื่อนที่ของอนุภาค พลังงานสูงจากดวงอาทิตย์

โดย

ดร.ปิยเนตร ฉุยฉาย และคณะ

รายงายวิจัยฉบับสมบูรณ์

โครงการผลกระทบเนื่องจากสนามแม่เหล็กป^{ั่}นป่วนในตัวกลางระหว่างดาวเคราะห์ต่อการเคลื่อนที่ของอนุภาค พลังงานสูงจากดวงอาทิตย์

ผู้วิจัย สังกัด

- 1. ดร.ปิยเนตร ฉุยฉาย มหาวิทยาลัยแม่ฟ้าหลวง
- 2. ศ.ดร.เดวิด รูฟโฟโล มหาวิทยาลัยมหิดล

สนับสนุนโดยสำนักงานคณะกรรมการอุดมศึกษา

และสำนักงานกองทุนสนับสนุนงานวิจัย

(ความเห็นในรายงานนี้เป็นของผู้วิจัย สกอ. และ สกว.ไม่จำเป็นต้องเห็นด้วยเสมอไป)

บทคัดย่อ

รหัสโครงการ: MRG5280239

ชื่อโครงการ: โครงการผลกระทบเนื่องจากสนามแม่เหล็กปั่นป่วนในตัวกลางระหว่างดาวเคราะห์

ต่อเคลื่อนที่ของอนุภาคพลังงานสูงจากดวงอาทิตย์

ชื่อนักวิจัย และสถาบัน: ดร.ปิยเนตร ฉุยฉาย

สำนักวิชาวิทยาศาสตร์ มหาวิทยาลัยแม่ฟ้าหลวง

Email Address: piyanate@gmail.com

ระยะเวลาโครงการ: 2 ปี

บทคัดย่อ:

ในตัวกลางระหว่าดาวเคราะห์ สนามแม่เหล็กปั่นป่วนมีอิทธิพลต่อการขนส่งอนุภาคที่มีประจุพลังงาน สูง ที่ผ่านมามีการศึกษาพบว่า แบบจองสนามแม่เหล็กปั่นป่วนแบบสององค์ประกอบ (2D+slab) เป็น แบบจำลองที่นิยมใช้และใกล้เคียงกับสนามแม่เหล็กปั่นป่วนในระบบสุริยะ โดยปกติเราพบลักษณะการฟุ้งของ อนุภาคที่มีประจุในสนามแม่เหล็กปั่นป่วนเมื่ออนุภาคเคลื่อนที่เป็นเวลานาน บ่อยครั้งในการศึกษา อนุภาคถูก สมมติให้เคลื่อนที่ตามเส้นสนามแม่เหล็ก และเกิดการฟุ้งเนื่องจากการเดินสุ่มของสนามแม่เหล็ก อย่างไรก็ ตามบางทฤษฎีได้กล่าวถึงการขนส่งอนุภาคในแนวตั้งฉาก เช่น nonlinear guiding center (NLGC) ทฤษฎีนี้มี การใส่กลไกการเดินข้ามสนามแม่เหล็กของอนุภาค ซึ่งทำให้เกิดการแยกตัวระหว่างอนุภาคและเส้น สนามแม่เหล็กที่สัมพันธ์กับตำแหน่งเริ่มต้น ในงานวิจัยนี้เราจึงสนใจศึกษากลไกที่อนุภาคที่มีประจุแยกตัวกับ เส้นสนามแม่เหล็กที่สัมพันธ์กับศูนย์กลางการเคลื่อนที่ของอนุภาคที่ตำแหน่งเริ่มต้น รวมทั้งผลกระทบ เนื่องจากการลดจำนวนมิติของความแปรปรวนในสนามแม่เหล็ก เราทำการจำลองเชิงตัวเลขสำหรับเส้นทาง

เดินอนุภาคที่มีประจุในสนามแม่เหล็กปั่นป่วนในหลายกรณี จากนั้นหาเส้นทางเดินสนามแม่เหล็กที่มี
จุดเริ่มต้นเดียวกับจุดศูนย์กลางการเลื่อนที่ของอนุภาค ทำการคำนวณสถิติของการแยกตัวระหว่างศูนย์กลาง
การเคลื่อนที่ของอนุภาคและเส้นสนามแม่เหล็ก ในงานวิจัยนี้เราสนใจศึกษาผลกระทบของ มุมชั้วเริ่มต้น
พลังงานของอนุภาค ความแรงของสนามแม่เหล็ก สัดส่วนของความแปรปรวน และการลดจำนวนมิติของ
ความแปรปรวน ที่มีต่อการแยกตัว นอกจากนั้นในงานวิจัยนี้เราได้พัฒนาเทคนิคการวัดและแก้ไขค่า Taylor
microscale ซึ่งเป็นค่าที่พบในสนามแม่เหล็กปั่นป่วนในอวกาศ เราจะลองข้อมูลสนามแม่เหล็กที่ขึ้นกับเวลาจาก
รูปแบบของสเปกตรัมที่เราออกแบบสำหรับสนามแม่เหล็กแบบปั่นป่วน ซึ่งเรานำข้อมูลสนามแม่เหล็กที่ได้จาก
จำลองมาหาค่า correlation function และ structure function จากนั้นใช้วิธีการฟิตและการประมาณนอกช่วง
เพื่อประมาณค่า Taylor microscale ในตอนท้ายเราแสดงการประยุกต์ใช้เทคนิคนี้กับข้อมูลจากยานอวกาศ

คำหลัก: อนุภาคพลังงานสูง, สนามแม่เหล็กปั่นป่วน, การฟุ้ง, การลอยเลื่อน

ABSTRACT

Project Code: MRG5280239

Project Title: The effect of turbulent magnetic fields in interplanetary space on

the motion of solar energetic particles

Investigator: Dr. Piyanate Chuychai

School of Science, Mae Fah Luang University

E-mail Address: piyanate@gmail.com

Project Period: 2 years

Abstract:

In interplanetary space, the transport of energetic charged particles is influenced by a turbulent magnetic field. Previous studies have shown that a two-component (2D+slab) magnetic model of turbulence is a useful model for the magnetic field in the heliosphere. Normally, the diffusive behavior of charged particles in a turbulent magnetic field is observed when they approach the long time limit. The charged particles are often assumed to follow and diffuse according to the random walk of the field lines but some theories of perpendicular particle transport, such as nonlinear guiding center theory (NLGC), implicitly assume some true crossfield diffusion in which particles separate from the field line connected to their initial location. In this work, we study the mechanism by which charged particles separate from their initial magnetic field lines and also the effect of reduced dimensionality of the magnetic field on crossfield motion of the charged particles. Here we perform numerical simulations of charged particle trajectories in several cases of magnetic turbulence such as pure slab turbulence, Gaussian 2D field+slab turbulence, and 2D+slab turbulence. Then we trace their corresponding magnetic field lines which start at the initial guiding centers of the charged particles. After that we compute statistics of the mean squared average transverse separation between guiding centers of the particles and field lines. We will examine the effects of the initial pitch angle, particle energy, fraction of 2D and slab lines in order to understand the separation behavior. Furthermore, we develop the measuring and correcting techniques for Taylor microscale which is one of length scales that we can find from turbulent magnetic field in space. Time series of the signal generated from known spectrum of turbulent magnetic field lead us to the correlation function and structure function. Fitting and extrapolation methods are used in other to estimate the Taylor microscale. The application of this technique to real spacecraft data of solar wind is also presented.

Keywords: energetic charged particles, turbulent magnetic field, diffusion, drift.

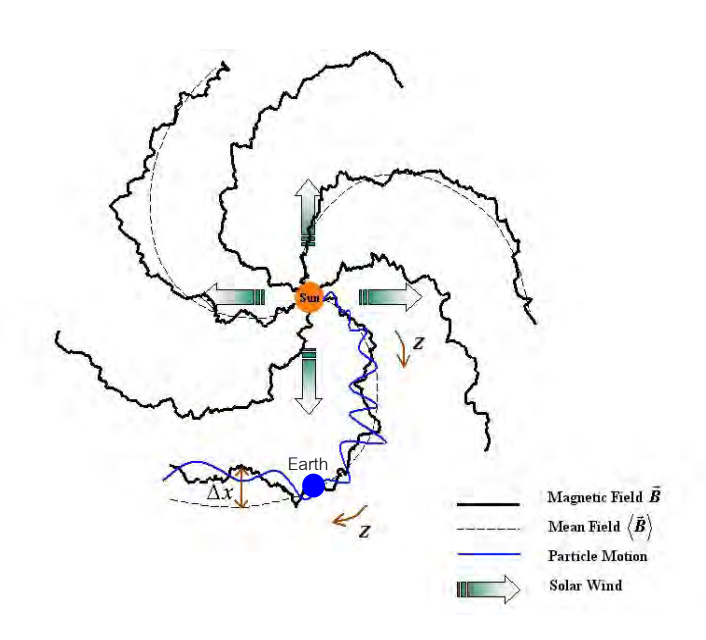
หน้าสรุปโครงการ (Executive Summary) ทุนพัฒนาศักยภาพในการทำงานวิจัยของอาจารย์รุ่นใหม่

1. ความสำคัญและที่มาของปัญหา

ดวงอาทิตย์ประกอบไปด้วยสนามแม่เหล็ก และก๊าซร้อนที่แตกตัวเป็นไอออนซึ่งเราเรียกว่าพลาสมา (plasma) พลาสมาบนดวงอาทิตย์นี้ส่วนหนึ่งถูกกักด้วยเส้นสนามแม่เหล็กวงปิดบนดวงอาทิตย์ พลาสมาอีกส่วนมีพลังงานเพียง พอที่จะไหลออกมาอย่างต่อเนื่องสู่ตัวกลางระหว่างดาวเคราะห์ (interplanetary space) ด้วยความเร็วโดยเฉลี่ยประมาณ 400 km/s ซึ่งเราเรียกพลาสมาส่วนนี้ว่าลมสุริยะ (solar wind) การไหลของลมสุริยะมีลักษณะปั้นป่วนและในขณะเดียวกัน ได้ลากเอาสนามแม่เหล็กออกมาสู่ตัวกลางระหว่างดาวเคราะห์ด้วย เนื่องจากการหมุนของดวงอาทิตย์และความปั้นปวนของ ลมสุริยะ ลักษณะของสนามแม่เหล็กระหว่างดาวเคราะห์จึงมีลักษณะเป็นเกลียวกันหอยและมีความปั้นป่วน ดังแสดงในรูปที่ ่ 1 นอกจากนี้ดวงอาทิตย์มีการประทุและปลดปล่อยอนุภาคพลังงานสูง (solar energetic particles) สู่ตัวกลางระหว่างดาว เคราะห์ ซึ่งส่วนใหญ่เป็นอนุภาคที่มีประจุไฟฟ้า ที่มีค่าตั้งแต่ระดับพลังงาน keV ถึงระดับ GeV ซึ่งอนุภาคเหล่านี้มีผลต่อ ชั้นบรรยากาศของโลก เมื่อเกิดการปะทุอย่างรุนแรงที่ดวงอาทิตย์หรือที่เราเรียกว่าพายุสุริยะ โดยทั่วไปตามทฤษฎีพิสิกส์ พื้นฐานทางแม่เหล็กไฟฟ้า เมื่ออนุภาคที่มีประจุอยู่ในสนามแม่เหล็กจะเคลื่อนที่เป็นเกลียวรอบสนามแม่เหล็ก โดยลักษณะ การเกลียวขึ้นอยู่กับความเข้มของสนามแม่เหล็ก ความเร็วของอนุภาค และมุมระหว่างทิศทางการเคลื่อนที่ของอนุภาคกับ ทิศของสนามแม่เหล็ก ดั้งนั้นอนุภาคพลังงานสูงที่ปลดปล่อยออกมาจากดวงอาทิตย์จึงเคลื่อนที่เกลียวรอบสนามแม่เหล็ก เช่นเดียวกัน แต่เนื่องจากสนามแม่เหล็กระหว่างดาวเคราะห์มีลักษณะปั้นป่วน การเคลื่อนที่ของอนุภาคจึงมีลักษณะซับซ้อน ้กว่าการเคลื่อนที่แบบทั่วไป เนื่องจากสนามแม่เหล็กเป็นสิ่งที่กำหนดทิศทางการขนส่งอนุภาคสู่ตัวกลางระหว่างดาวเคราะห์ ดังนั้นการศึกษาอิทธิพลของสนามแม่เหล็กปั่นป่วนต่ออนุภาคที่เคลื่อนที่ในอวกาศ จึงมีความสำคัญในการนำไปสู่การอธิบาย กลไกและปรากฏการณ์ต่างๆที่มีการสังเกตและเก็บข้อมูลจากยานอวกาศ เช่น ปรากฏการณ์การเปลี่ยนแปลงความเข้ม อย่างรวดเร็วของอนุภาคพลังงานสูง (dropouts) และการลดลงของรังสีคอสมิคในกาแลกซีเนื่องจากลมสุริยะ (solar modulation) นอกจากนี้งานวิจัยนี้จะทำให้เราเกิดองค์ความรู้ใหม่ทางฟิสิกส์ จึงคาดว่าผลที่ได้จากการวิจัยยังสามารถนำไป ประยุกต์ใช้สำหรับการเคลื่อนที่ของอนุภาคในสนามแม่เหล็กปั้นป่วนในห้องทดลอง เช่น ในการพยายามผลิตพลังงานจาก การควบคุมปฏิกิริยานิวเคลียร์ฟิวชัน และในสถานการณ์อื่นๆได้อีกด้วย

จากการศึกษาที่ผ่านมา นักวิทยาศาสตร์ได้ให้ความสนใจที่จะอธิบายกลไลการเคลื่อนที่หรือการขนส่งอนุภาคใน อวกาศและแบ่งได้เป็นสองกลุ่มใหญ่ ๆ กลุ่มแรกคือศึกษาถึงสิ่งที่เป็นสาเหตุให้อนุภาคเคลื่อนที่นั่นคือสนามแม่เหล็กปนั่นป่วน เนื่องจากทางเดินของอนุภาคมีลักษณะเกลียวรอบสนามแม่เหล็ก ดังนั้นจึงประมาณได้ว่าศูนย์กลางการเกลียวรอบสนามแม่เหล็กของอนุภาค (guiding center) มีเส้นทางประมาณหรือใกล้เคียงกับเส้นสนามแม่เหล็ก ดังนั้นนักวิทยาศาสตร์ กลุ่มนี้จึงมุ่งที่จะเข้าใจเส้นทางเดินของสนามแม่เหล็ก ก่อนที่จะศึกษาการเคลื่อนที่ของอนุภาคโดยตรง จึงหันมาศึกษาปัญหากรพุ้งของเส้นทางเดินของสนามแม่เหล็กจากแนวสนามแม่เหล็กเฉลี่ยซึ่งมีลักษณะปัญหาที่ซับซ้อนน้อยกว่าศึกษาการเคลื่อนที่ของอนุภาคโดยตรง จึงได้มีการสร้างแบบจำลองสนามแม่เหล็กแบบปั่นป่วน และสร้างทฤษฎีต่าง ๆเพื่อที่จะเข้าใจ และอธิบายเส้นทางเดินของอนุภาค แต่เราพบว่าการศึกษาเพียงการพุ้งของเส้นสนามแม่เหล็กทำให้เราเข้าใจการเคลื่อนที่ของอนุภาคเพียงแค่บางส่วนเท่านั้น และเมื่อเปรียบเทียบกับการขนส่งหรือการฟุ้งของอนุภาคโดยตรงยังมีความแตกต่างอยู่ มาก เนื่องจากการเคลื่อนที่ของอนุภาคโดยตรง โดยพยายามทำการจำลองและสร้างทฤษฎีที่สามารถประยุกต์ได้กับอนุภาคโดยตรง แต่ เนื่องจากงานวิจัยที่ผ่านมายังไม่เข้าใจกลไกที่เกิดเนื่องจากลักษณะสนามแม่เหล็กปั่นป่วนโดยตรงที่ซัดเจน จึงทำให้ทฤษฎีที่

ได้มาในปัจจุบันยังไม่สมบรูณ์ และไม่ครอบคลุมปัญหาโดยทั่วไป ดังนั้นในงานวิจัยนี้จึงมุ่งเน้นที่จะศึกษาและหา ความสัมพันธ์ระหว่างเส้นสนามแม่เหล็ก และเส้นทางเดินของอนุภาคโดยใช้การจำลองเชิงตัวเลขและปรับปรุงทฤษฏีที่ อธิบายและนำไปประยุกต์ใช้กับการขนส่งของอนุภาคในอวกาศให้สมบูรณ์และครอบคลุมปัญหาโดยทั่วไปมากขึ้น นอกจากนี้เรายังสนใจปัญหาทั้งที่เป็นแบบสนามแม่เหล็กปั่นป่วนที่ไม่ขึ้นกับเวลา (static turbulent magnetic field) และ แบบที่ขึ้นกับเวลา (dynamical turbulent magnetic field) ซึ่งในแบบหลังจะใกล้เคียงกับสถานการณ์จริงมากขึ้น



รูปที่ 1 แสดงโครงสร้างสนามแม่เหล็กและลมสุริยะ

2. วัตถุประสงค์

- 2.1 เพื่อเข้าใจความสัมพันธ์ระหว่างการเคลื่อนที่ของอนุภาคที่มีประจุและเส้นสนามแม่เหล็กปั่นป่วน
- 2.2 เพื่อหาผลกระทบของการลอยเลื่อนและการเคลื่อนที่ข้ามเส้นแม่เหล็กของอนุภาคที่มีประจุเนื่องจากความ ป^{ั่}นปวนของเส้นสนามแม่เหล็กทั้งในเชิงวิเคราะห์และเชิงตัวเลข
- 2.3 เพื่อสร้างแบบจำลองสำหรับสนามแม่เหล็กแบบปั่นป่วนที่ขึ้นกับเวลาและศึกษาการเดินสุ่มของเส้น สนามแม่เหล็กปั่นป่วนที่เคลื่อนที่
- 2.4 เพื่อหาความสัมพันธ์ระหว่างสนามแม่เหล็กที่ขึ้นกับเวลาและการเคลื่อนที่ของอนุภาคที่มีประจุ

3. ระเบียบวิธีวิจัย

โครงการนี้มีการศึกษาแบ่งได้เป็นสองส่วนคือ

3.1 การศึกษาความสัมพันธ์ระหว่างเส้นสนามแม่เหล็กและเส้นทางเดินของอนุภาค

ระเบียบวิธีการวิจัยในส่วนนี้จะแบ่งออกเป็นการจำลองเชิงตัวเลขด้วยชุดคอมพิวเตอร์ที่ต่อแบบขนาน (parallel computing) เพื่อให้มีประสิทธิ์ภาพการทำงานสูง และอีกส่วนคือการคำนวณเชิงวิเคราะห์เพื่อสร้างทฤษฎีมาอธิบายผลที่ได้ จากการจำลองเชิงตัวเลข การสร้างทฤษฎีนี้จะช่วยนำไปประยุกต์ใช้ในงานวิจัยในอนาคตได้ง่ายขึ้น ในส่วนที่เป็นการจำลอง

เชิงตัวเลขจะเป็นการจำลองเส้นทางเดินสนามแม่เหล็กปั่นป่วนและการจำลองเส้นทางเดินของอนุภาคในสนามแม่เหล็ก ปั่นป่วนชุดเดียวกับที่หาเส้นทางเดินของสนามแม่เหล็ก โดยเราจะใช้แบบจำลองสนามแม่เหล็กแบบสององค์ประกอบเพื่อ สร้างชุดของสนามแม่เหล็กในอวกาศ จากนั้นแก้สมการเชิงอนุพันธ์ของเส้นสนามแม่เหล็ก (field line equations) เพื่อหา เส้นทางเดินของสนามแม่เหล็ก โดยทำการกำหนดจุดเริ่มต้นของเส้นสนามแม่เหล็กในบริเวณต่างๆ จากนั้นโปรแกรมจะ คำนวณเส้นทางเดินของสนามแม่เหล็กซึ่งมีจำนวนมากและใช้เนื้อที่ในการเก็บข้อมูลมากเพื่อให้ได้สถิติที่ดีเมื่อนำไป วิเคราะห์ข้อมูล จากนั้นทำการจำลองอีกครั้งโดยใช้สนามแม่เหล็กชุดเดียวกับที่ทำการจำลองหาเส้นสนามแม่เหล็ก แต่หา เส้นทางเดินของอนุภาคที่มีตำแหน่งเริ่มต้นที่เดียวกับจุดเริ่มต้นของสนามแม่เหล็กดังกล่าวข้างต้น แก้สมการเชิงอนุพันธ์นิว ต้น-ลอเรนซ์ (Newton-Lorentz equation) ผลที่ได้จะเป็นตำแหน่งเส้นทางเดินของอนุภาคที่เคลื่อนที่อยู่ใกล้เคียงกับเส้น สนามแม่เหล็กที่เราหามาได้ข้างต้น จากนั้นจะวิเคราะห์หาความสัมพันธ์ของเส้นทางเดินของอนุภาค

3.2 การสร้างแบบจำลองสนามแม่เหล็กปั่นป่วนที่ขึ้นกับเวลาและศึกษาการเดินสุ่ม

เช่นเดียวกับการศึกษาในส่วนแรก ระเบียบวิธีการวิจัยในส่วนนี้จะแบ่งออกเป็นการจำลองเชิงตัวเลขด้วยชุด คอมพิวเตอร์ที่ต่อแบบขนานและอีกส่วนคือการคำนวณเชิงวิเคราะห์เพื่อสร้างทฤษฎีมาอธิบายผลที่ได้จากการจำลองเชิง ตัวเลข เราจะใช้หลักการคำนวณหาเส้นสนามแม่เหล็กเช่นเดียวกับหัวข้อ 3.1 เพียงแต่เราจะทำการปรับปรุงฟังก์ชันในการ สร้างชุดสนามแม่เหล็กปั่นป่วนแบบสององค์ประกอบให้ขึ้นกับเวลา ซึ่งแบบจำลองของสนามแม่เหล็กปั่นป่วนที่อยู่กับเวลาที่ เราจะทำการศึกษาในโครงการวิจัยนี้มีอยู่สองแบบคือแบบ random sweeping และ แบบ damping ดังนั้นเราจึงต้อง ออกแบบการสร้างชุดสนามแม่เหล็กที่ขึ้นกับเวลาเชิงตัวเลข เพื่อให้เข้ากับแบบจำลองดังกล่าว ในการศึกษาในส่วนนี้เราจะ เก็บข้อมูลของเส้นสนามแม่เหล็กที่เวลาและตำแหน่งต่าง ๆแล้วมาวิเคราะห์ทางสถิติเพื่อนำมาประยุกต์ใช้กับการเคลื่อนที่ ของอนุภาคในอวกาศ ซึ่งในการศึกษาส่วนนี้จะมีลักษณะใกล้เคียงกับธรรมชาติมากขึ้นเนื่องจากแท้จริงแล้วสนามแม่เหล็กใน อวกาศมีการเปลี่ยนแปลงตามเวลา

4. แผนการดำเนินงานวิจัยตลอดโครงการในแต่ละช่วง 6 เดือน

4.1 แผนงานเดือนที่ 1-6

- 4.1.1 ศึกษาค้นคว้าและรวบรวมข้อมูล เพื่อที่จะทราบแนวทางในป[ั]จจุบัน และนำมาประยุกต์ ออกแบบ งานวิจัยที่กำลังจะดำเนินการ
- 4.1.2 จัดซื้ออุปกรณ์ และสร้างชุดการคำนวณเชิงตัวเลข ได้อุปกรณ์พร้อมสำหรับทำวิจัย
- 4.1.3 ออกแบบเงื่อนไขค่าเริ่มต้นและค่าคงที่ต่างๆเพื่อนำไปคำนวณเชิงตัวเลข และทำการจำลองเส้น สนามแม่เหล็กปั่นป่วนและการเคลื่อนที่ของอนุภาคที่เส้นสนามแม่เหล็กนั้น เก็บข้อมูล เพื่อให้ได้ ข้อมูลเส้นทางเดินสนามแม่เหล็กและอนุภาคที่มีความสัมพันธ์กัน

4.2 แผนงานเดือนที่ 7-12

- 4.2.1 วิเคาระห์หาความสัมพันธ์ทางสถิติระหว่างเส้นสนามแม่เหล็กปั่นป่วนกับการเคลื่อนที่ของอนุภาค เพื่อเข้าใจถึงกลไกทางฟิสิกส์ของอนุภาคในเส้นสนามแม่เหล็กป^{ั่}นป่วน
- 4.2.2 เผยแพร่ผลงาน และเรียบเรียงผลงานเพื่อการตีพิมพ์สำหรับบทความแรก

4.3 แผนงานเดือนที่ 13-18

- 4.3.1 ออกแบบการคำนวณเชิงตัวเลขเพื่อสร้างฟังก์ชันสนามแม่เหล็กที่ขึ้นกับเวลา เพื่อให้ได้ชุด สนามแม่เหล็กป^{ั่}นป่วนที่เปลี่ยนแปลงไปตามเวลา
- 4.3.2 จำลองเส้นสนามแม่เหล็กปั่นป่วนที่ขึ้นกับเวลา และเก็บข้อมูล เพื่อนำไปวิเคราะห์ทางสถิต

4.4 แผนงานเดือนที่ 19-24

- 4.4.1 วิเคาระห์ข้อมูลและสร้างทฤษฎีการฟุ้งของสนามแม่เหล็กปั่นป่วนที่ขึ้นกับเวลา และนำผลที่ได้ เปรียบเทียบกับกรณีที่ไม่ขึ้นกับเวลาและการเคลื่อนที่ของอนุภาค เพื่อเข้าใจถึงกลไกทางฟิสิกส์ ของการเปลี่ยนแปลงตามเวลาของเส้นสนามแม่เหล็กปั่นป่วน และการเคลื่อนที่ของอนุภาคใน สนามแม่เหล็กปั่นป่วนที่ขึ้นกับเวลา
- 4.4.2 เผยแพร่ผลงาน และเรียบเรียงผลงานเพื่อการตีพิมพ์บทความที่สอง

5. ผลงาน/หัวข้อเรื่องที่คาดว่าจะตีพิมพ์ในวารสารวิชาการระดับนานาชาติในแต่ละปี

ปีที่ 1: ชื่อเรื่องที่คาดว่าจะตีพิมพ์:

Separation of charged particle trajectories from turbulent magnetic field lines ชื่อวารสารที่คาดว่าจะตีพิมพ์: Astrophysical Journal (impact factor = 6.405)

ปีที่ 2: ชื่อเรื่องที่คาดว่าจะตีพิมพ์:

Dynamical magnetic field turbulence and implications for the transport of charged particles in interplanetary space

ชื่อวารสารที่คาดว่าจะตีพิมพ์: Astrophysical Journal (impact factor = 6.405)

6. งบประมาณโครงการ (ตามระยะเวลาโครงการที่ได้เสนอรับทุน)

รายการค่าใช้จ่าย	จำนวนเงิน (บาท)			
1.1361.150.1E		ปีที่ 1	ปีที่ 2	รวม
1. หมวดค่าตอบแทน				
- ค่าตอบแทนหัวหน้าโครงการ (5,000	บาท/เดือน)	60,000	60,000	120,000
2. หมวดค่าวัสดุ / ครุภัณฑ์				
- เครื่องคอมพิวเตอร์จำนวน 2 ชุด เพื่อเ	าการคำนวณ	96,000	-	96,000
แบบขนาน (cluster)*				
- แผ่น DVDs เพื่อเก็บข้อมูลสำรอง		2,000	3,000	5,000
,				
3. หมวดค่าใช้สอย				
- ค่าใช้จ่ายในการตีพิมพ์วารสาร Astro	hysical Journal	-	80,000	80,000
- ค่าไปรษณีย์และโทรศัพท์		3,000	5,000	8,000
- ค่าหนังสือและค่าถ่ายเอกสาร		7,000	12,000	19,000
- การเดินทางเพื่อรายงานความก้าวหนึ่	าและ	12,000	20,000	32,000
สัมมนาอื่นๆ				
รวมงบประมาณโครงการ		180,000	180,000	360,000

Contents

	Page
Thai Abstract	i
English Abstract	iii
Executive Summary	v
Contents	X
List of Figures	xii
List of Tables	xvi
Chapter 1 Introduction	
1.1 Overview	1
1.2 Objectives	3
Chapter 2 Model of Turbulent Magnetic Field	
2.1 Two-Component Magnetic Turbulence	4
2.1.1 Slab Fluctuation	5
2.1.2 Two Dimensional (2D) Fluctuations	7
2.2 Turbulent Magnetic Field with Taylor Microscale	12
Chapter 3 Methodology	
3.1 Generation of magnetic field	15
3.1.1 Turbulence Magnetic Field	15
3.1.2 Simple Gaussian 2D Field	17
3.1.3 Turbulent Magnetic Field with Taylor Microscale	17
3.2 Particle Simulations	19
3.3 Magnetic Field Line Simulations	20
3.4 Simulation and Analysis Method for Separation between	
Charged Particles and Field Lines	20

Contents

	Page
Chapter 4 Effect of Reduced Dimensionality of the Magnetic Field	
Fluctuations on the Cross-Field Motion of Charged	
Particles	
4.1 Simulation Setup	23
4.2 Results	24
4.3 Conclusions and Discussion	28
Chapter 5 Separation of Charged Particles from Their Turbulent	
Magnetic Field Lines	
5.1 Separation of Charged Particles and Field Lines in Guassian	
2D Field + Slab Turbulence	30
5.2 Separation of Charged Particles and their field lines in	
2D+Slab tubuelence	38
Chapter 6 Technique for Measuring and Correcting the Taylor	
Microscale	
6.1 Correlation Function and Structure Function	44
6.2 Extrapolation Method	48
6.3 Correction Ratio	52
6.4 Applying the Technique to Spacecraft Data	53
6.5 Conclusions	56
References	57
Output	60
Appendix	62

List of Figure

Figure	Page
Figure 1.1 Structure of interplanetary magnetic field and solar wind with	
moving charged particle.	1
Figure 2.1 Illustration of the slab fluctuation, which depends only on the z	
coordinate. The arrows demonstrate the slab fluctuation \vec{b}_{slab} .	5
Figure 2.2 Example of a slab power spectrum.	6
Figure 2.3 Example of two trajectories of magnetic field lines in pure slab	
turbulence.	7
Figure 2.4 Schematic contour plot of $a(x, y)$. The solid arrows show the	
2D field, \vec{b}_{2D} , and the dashed arrows show examples of the	
directions of $\overrightarrow{\nabla}a(x,y)$ for both positive and negative potential	
functions. The 2D field must lie along the equipotential lines of	
the potential function. For a positive potential function, the 2D	
field is in a counter-clockwise direction, while a 2D field having	
a negative potential function is in the clockwise direction.	8
Figure 2.5 Example of a trajectory of a magnetic field line in pure 2D	
turbulence.	9
Figure 2.6 Sample of magnetic field lines in 2D+slab magnetic field	
turbulence that start at the difference locations. The field lines	
near O-point are trapped along some distance before they	
diffuse while the field line near X-point quickly spread at the	
beginning (Chuychai et al. 2007).	10
Figure 2.7 Magnetic field line trajectories for a single 2D island, with	
$\vec{B} = B_0 \hat{z} + \vec{b}_{2D}(x, y)$. The surface plot at bottom shows the	
potential function $a(x, y)$ of the 2D field (Chuychai et al.	
2007).	11

List of Figures (Cont.)

Figure	Page
Figure 2.8 Example of two magnetic field lines in a single 2D Gaussian	
island plus slab turbulence. The red field line started deep inside	
the island, whereas the blue field line was initially located	
outside the island. The surface plot at bottom shows the	
potential function $a(x, y)$ of the 2D field (Chuychai et al.	
2007).	12
Figure 3.1 The power spectrum for a number of values of q in the	
dissipation range.	18
Figure 3.2 Illustration of a particle orbit, magnetic field line and guiding	
center (Wikee 2013).	21
Figure 3.3 The diagram of separation between the guiding center and	
magnetic field line (Wikee 2013).	22
Figure 4.1 The mean squared separation between guiding centers of 100	
MeV particles starting at $r_0 = 0.5\lambda$ with their field lines in the	
pure 2D field. The value close to r_0^2 implies confinement to flux	
surface.	25
Figure 4.2 The mean squared separation between guiding centers of 10	
MeV particles starting at $r_0=0.1\lambda$ with their field lines in the	
pure 2D field.	26
Figure 4.3 The mean squared separation between guiding centers of 100	
MeV particles and their field lines in pure slab turbulence. The	
low value indicates confinement of the particle to remain near	
the same field line.	27
Figure 4.4 The mean squared separation spreading between guiding	
centers of 100 MeV particles and their field lines in Gaussian	
2D field + slab turbulence. The continual increase indicates	
unconstrained cross-field motion in this fully three-dimensional	
case.	28

List of Figures (Cont.)

Figure	Page
Figure 5.1 Example of the trajectory of a charged particle in our model;	
red line demonstrates trajectory of magnetic field line, black	
line and blue line demonstrate trajectories of charged particle	
and its guiding centers, respectively.	31
Figure 5.2 The results of the separation of charged particles and their	
corresponding field lines in the log-log scale.	32
Figure 5.3 The profile of the 2D Gaussian magnetic field along the	
distance from the center of the flux tube.	34
Figure 5.4 Showing shape of drift speed of guiding center due to the	
gradient of the magnetic field, radius of curvature of the	
magnetic field line and the summation of the gradient drift and	
curvature drift in arbitrary units.	35
Figure 5.5 Showing the separation of the charged particles at a) inside the	
2D island and b) outside the 2D island.	36
Figure 5.6 The mean squared perpendicular displacement and time in the	
final range.	37
Figure 5.7 Examples of 20 MeV particle trajectories (BLACK lines), their	
guiding centers (BLUE dots), and their initial field lines (RED	
lines) in a) pure slab turbulence and b) 10% 2D+ 90% slab	
turbulence. Note that in our simulations the time scale is in units	
of λ/c and the length scale is in units of λ , where λ is the slab	
coherence scale and c is the speed of light.	38
Figure 5.8 The results from the simulations of 100 MeV protons in a) pure	
slab and b) 2D+slab turbulence. The statistics in the plots show	
the spreading of particles from field lines as a function of time.	39
Figure 5.9 The results of the separation of charged particles and their	
corresponding field lines when we vary particle energy.	40

List of Figures (Cont.)

Figure	Page
Figure 5.10 The results of the separation of charged particles and their	
corresponding field lines when we vary initial pitch angles.	41
Figure 5.11 The results of the separation of charged particles and their	
corresponding field lines when we vary particle 2D fraction.	42
Figure 5.12 The results of the separation of charged particles and their	
corresponding field lines when we vary magnetic field	
strength.	42
Figure 6.1 The structure function computed from the time series data for a	
number of values of q . The bottom curve is associated with a	
q value of -5 and the higher curves are determined with	
q = -4, -3, -2, and -1 , respectively.	47
Figure 6.2 The correlation function near the origin. The top curve is	
determined from $q = -5$ and the next curves are calculated	
using $q = -4, -3, -2$, and -1 , respectively.	48
Figure 6.3 Taylor microscale from parabolic fit of the correlation function	
near the origin for each τ_{fit} for a number of q . Axes are in	
units of τ_d .	50
Figure 6.4 Values of τ_{TS} determined by linear extrapolation from the data	
in Figure 6.3 at the origin (i.e., the intercept). Plotted are the	
extrapolated Taylor microscale values determined from a range	
of $ au_{max}$.	51
Figure 6.5 Correction ratio versus $1/ q $ for number of different Δt values.	53
Figure 6.6 The left column shows the plots before applying the correlation	
ratio to the Taylor mocroscale λ_T and the right column shows	
the Taylor microscale (λ'_T) after applying correlation ratio.	55

List of Tables

Table	Page
Table 3.1 Showing index q which we vary for each case and their Taylor	
scales when we fix dissipation scale ($\tau_d = 2.5 \text{ s}$).	19
Table 4.1 Saturation values for 100 MeV particles in the pure 2D field	
when we vary the location of the initial positions.	26

Chapter 1

Introduction

1.1 Overview

The Sun consists of magnetic field and ionized gas called plasma. Some plasma on the Sun is trapped by Sun's magnetic field and some part continuous flows out into interplanetary space with the speed approximately to 400 km/s which we call this part as solar wind. The flow of solar wind is turbulent and at the same time it drags the Sun's magnetic field into the space. Due to the rotation of the Sun and turbulence of the solar wind, the characteristic of interplanetary of magnetic field is achemedian spiral and turbulent as shown in Figure 1.1. The Sun also releases high energy particle called solar energetic particles into interplanetary space. Most of them are charged particles from keV to GeV. These particles effect to the Earth's atmosphere. Since the magnetic field is turbulent, the spectrum has the shape as Kolmogorov spectrum with has the slope -5/3 in inertial range. In this range the energy transfer from large to small scales. This is also the range that the plasma loses the energy called dissipation range. Taylor microscale is found as the scale that related to this range and observed from multi-spacecraft.

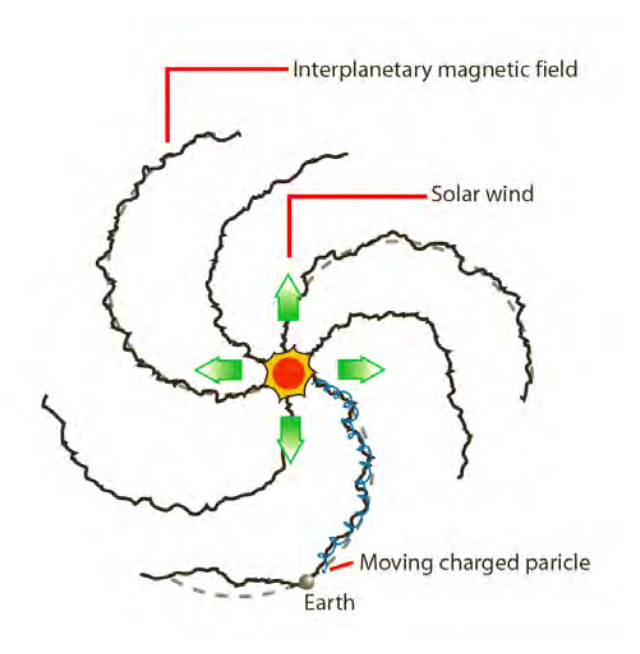


Figure 1.1 Structure of interplanetary magnetic field and solar wind with moving charged particle.

According to fundamental of electromagnetic field, when charged particles are in the magnetic field, they move as helical orbit around the magnetic field. The shape of spiral depends on the strength of magnetic field, particle's speed and the angle between the charged particle and the direction of magnetic field. Therefore, the energetic particles released from the Sun also orbit around the magnetic field. Since the magnetic field direction is the quantity that controls the transport of charged particles, the study of effect of the turbulent magnetic field to the charged particles in space is important to explain the mechanism and the phenomena that we can observe from the spacecraft data such as dropouts and solar modulation. Moreover, this research leads us to new knowledge about basic physics which might be able to apply to the motion of charged particles in turbulent magnetic field in laboratory.

From the previous study, the scientists are interested to explain the mechanism of the particle transport in the space. They can be divided into two big groups. The first one focuses the trajectories of the turbulent magnetic field line instead of the motion of charged particles. They assume that the guiding centers of particles are very close to the magnetic field line trajectories. They model several kind of magnetic turbulence and study the diffusion of field lines. This problem is less complicated than examining the motion of charged particle directly. However, we cannot understand all mechanisms if we only study the field lines. When we compare the real transport of the particles, they are still some different from field line theory. Another group of scientist studies the motion of charged particles in turbulent magnetic field directly and try to create the theory to explain the transport. Recently, there is no theory that can completely explain the mechanism and cover all general problems.

Therefore, this research examines the relationship between field line trajectories and the motion of the particle by using the numerical simulation and develops the theory to apply to particle transport in the interplanetary space. Furthermore, we also use method of generating field lines above to crate the signals which depend on time. Then we use the statistics properties that found in turbulent magnetic field to develop the technique to measure the Taylor microscale in real data from spacecraft.

1.2 Objectives

- To understand the relationship between the motion of particle and turbulent magnetic field.
- To find the drift and cross-field motion effects of charged particles due to the turbulence of magnetic field in both numerical and analytic calculation.
- To model the spectrum and generate the time-series signal to study the characteristic of length scale of turbulence of magnetic field.

Chapter 2

Model of Turbulent Magnetic Field

Since this research focus on the effect of turbulent magnetic fields in interplanetary space on the motion of solar energetic particles, in this chapter we present the model of magnetic field that we use. One is two-component magnetic turbulence to study the separation and another one is turbulent magnetic field with Taylor microscale to find the technique of measurement. We also assume that the magnetic field is static and homogeneous.

2.1 Two-Component Magnetic Turbulence

The two-component model was motivated by the observation that solar wind fluctuations are concentrated at nearly parallel and nearly perpendicular wave number (Matthaeus, Goldstein, & Roberts 1990). For the parallel component, the wave vector is parallel to the direction of the mean field and the fluctuation of the magnetic field in this component is perpendicular to both the parallel wave vector and the mean field. This is motivated by Alfóenic or slab like waves in the solar wind propagating along the mean field. We call this component the "slab" component. Another component, which is motivated by laboratory experiments, is called "two-dimensional (2D)" turbulence, which has a wave vector perpendicular to the mean magnetic field. The magnetic fluctuation in this component is also perpendicular to both the wave vector and the mean field. This component gives long correlation lengths in the direction of the mean field. The analysis of solar wind data by Matthaeus, Goldstein, & Roberts (1990) showed that the power spectrum of the solar wind turbulence is composed of these two components. Furthermore, the two-component model provides a good explanation of the parallel transport of SEPs (Bieber et al. 1994; Bieber, Wanner, & Matthaeus 1996; Dröge 2000), providing a solution to the long-standing discrepancy between theoretical and observed scattering mean free paths.

Two-component magnetic model can be generally written as

$$\vec{B}(x, y, z) = B_0 \hat{z} + \vec{b}_{slab}(z) + \vec{b}_{2D}(x, y). \tag{2.1}$$

The total magnetic field consists of the uniform mean field $(B_0\hat{z})$ and the transverse fluctuations $(\vec{b}_{slab} \text{ and } \vec{b}_{2D})$ which are in the perpendicular direction to the mean field. For the fluctuations, the slab (one dimensional) fluctuation depends on the z coordinate while the two dimensional (2D) fluctuation depends on the x and y coordinates (Chuychai 2004). Next, we introduce the characteristic of each type of magnetic field that we use in this research.

2.1.1 Slab Fluctuation

From the definition of the slab field, the fluctuation depends only on z. Therefore, if we consider the slab fluctuation in the x-y plane at each z, \vec{b}_{slab} is the same along that plane but different from the field on other planes as shown in Figure 2.1.

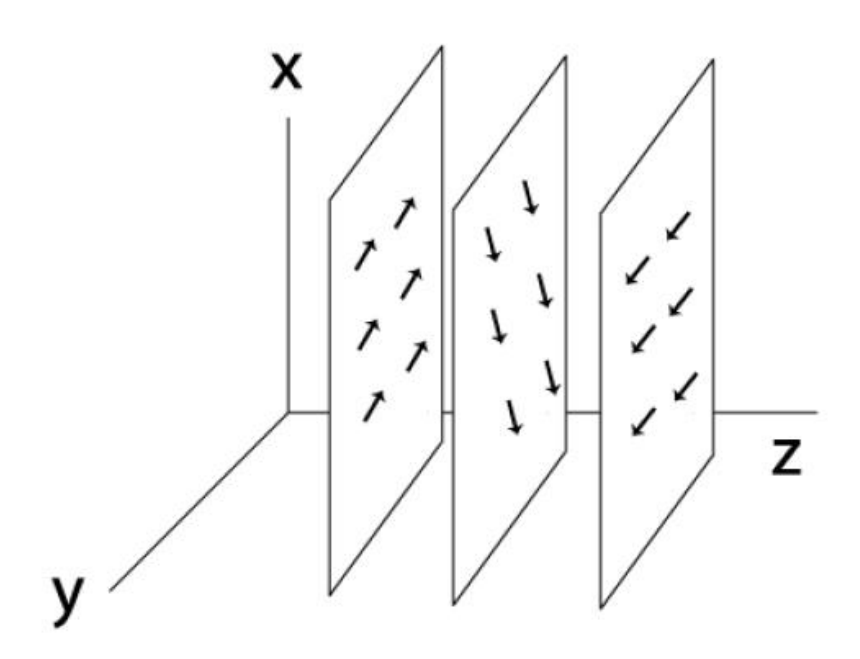


Figure 2.1 Illustration of the slab fluctuation, which depends only on the z coordinate. The arrows demonstrate the slab fluctuation \vec{b}_{slab} .

For the slab fluctuation, since the magnetic field is turbulent, the power spectrum is specified by a Kolmogorov spectrum, including an energy containing range and an inertial range with a 5/3 power law index, as

$$P_{\chi\chi}^{slab}(k_z) = P_{yy}^{slab}(k_z) = \frac{C}{[1+(k\lambda)^2]^{5/6}}$$
 (2.2)

where λ is a coherence length and C is constant. See the shape of spectrum in Figure 2.2. To generate the slab magnetic field, we first numerically compute the field in Fourier space by using the power spectrum and a random phase, and then transform them back to real space via and inverse Fourier transform. Finally, we will have the magnetic field data over detailed grid in the simulation box. Figure 2.3 shows the example of trajectories of magnetic field lines from pure slab turbulence $[B_0\hat{z} + \vec{b}_{slab}(z)]$.

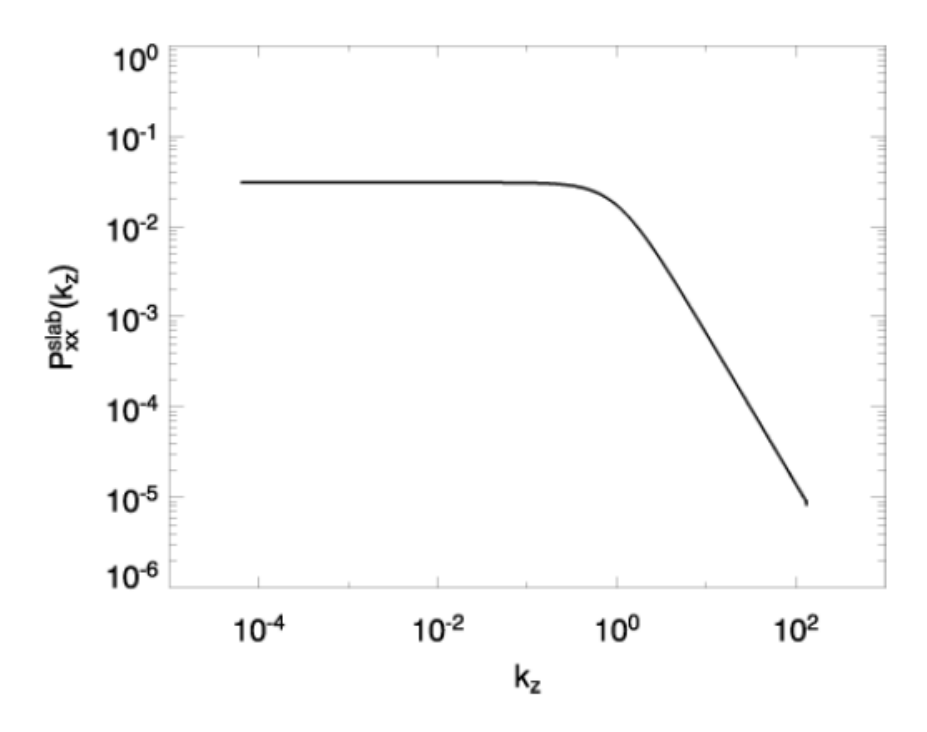


Figure 2.2 Example of a slab power spectrum.

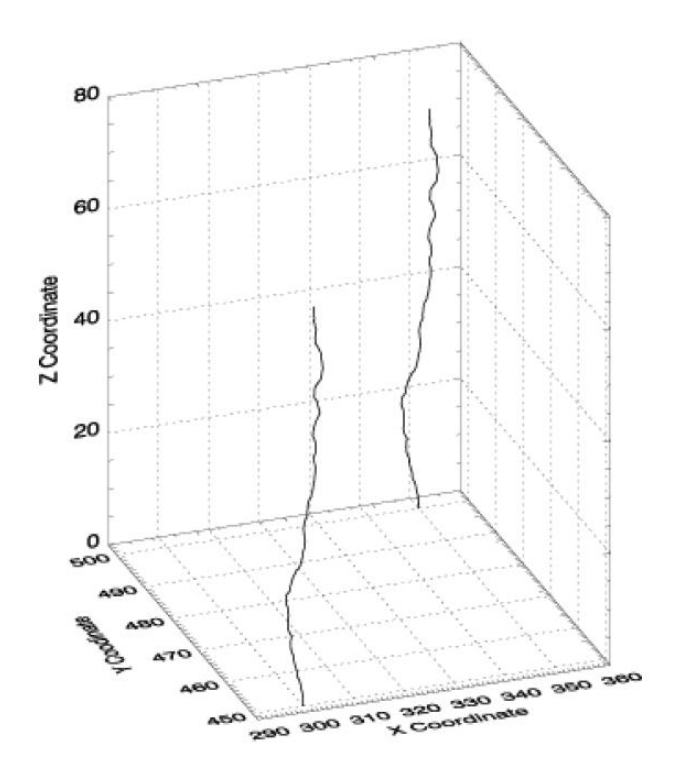


Figure 2.3 Example of two trajectories of magnetic field lines in pure slab turbulence.

2.1.2 Two Dimensional (2D) Fluctuations

For 2D field, the fluctuation depends only x and y coordinate. Since $\vec{\nabla} \cdot \vec{B} = 0$, we have $\vec{B} = \vec{\nabla} \times [a(x,y)\hat{z}]$, where a(x,y) is the vector potential. In this work, we create 2D field in two cases. For the first case, the 2D field is turbulent. To generate this type of fluctuation, we need to specify power spectrum in wave number space. Another case is simple 2D field which model as only one single island. Here the potential function is simply defined by a Gaussian function.

I. Two dimensional (2D) Turbulence

From $\vec{B} = \vec{\nabla} \times [a(x,y)\hat{z}]$, we can write 2D turbulence as $\vec{b}_{2D} = \vec{\nabla} a(x,y) \times \hat{z}$. From this relation, we can clearly see that the 2D field must be in the direction perpendicular to the gradient of the potential function and also to the z direction. Therefore, the direction of the 2D field must be along the equipotential line of a(x,y) as shown in Figure 2.4. A 2D field that has

a positive value of a(x, y) is in a counterclockwise direction while one that has a negative value has a clockwise direction. When we consider the pure 2D turbulence $[B_0\hat{z} + \vec{b}_{2D}(z)]$, the field lines conserve the value of the potential function and move along the contour of a(x, y). The example is shown as Figure 2.5.

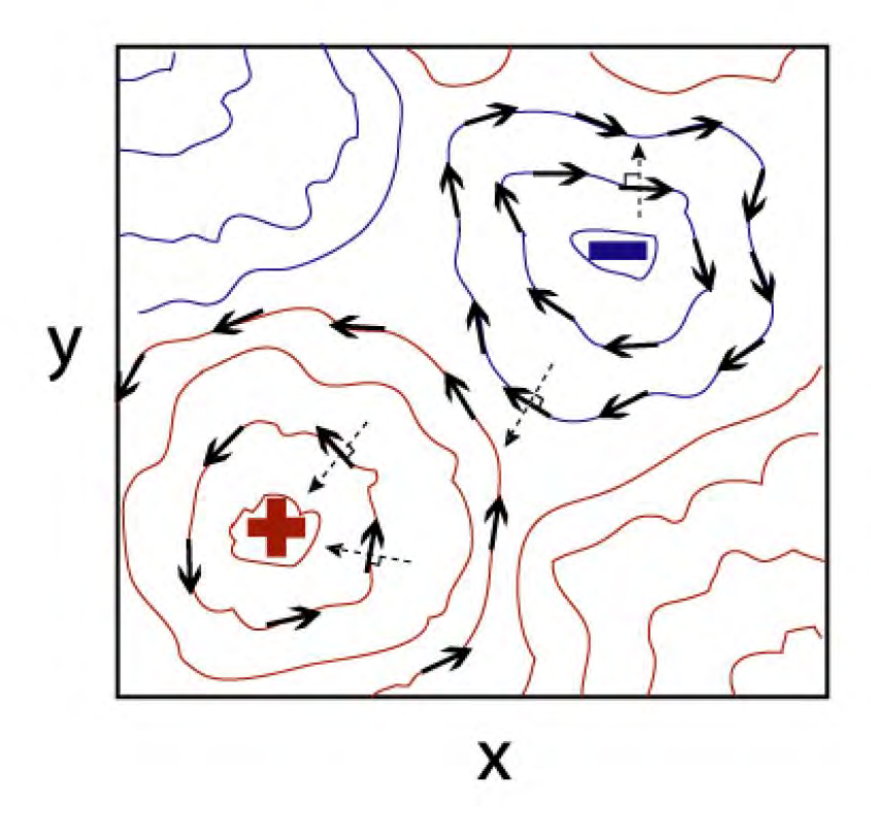


Figure 2.4 Schematic contour plot of a(x, y). The solid arrows show the 2D field, \vec{b}_{2D} , and the dashed arrows show examples of the directions of $\vec{\nabla}a(x, y)$ for both positive and negative potential functions. The 2D field must lie along the equipotential lines of the potential function. For a positive potential function, the 2D field is in a counter-clockwise direction, while a 2D field having a negative potential function is in the clockwise direction.

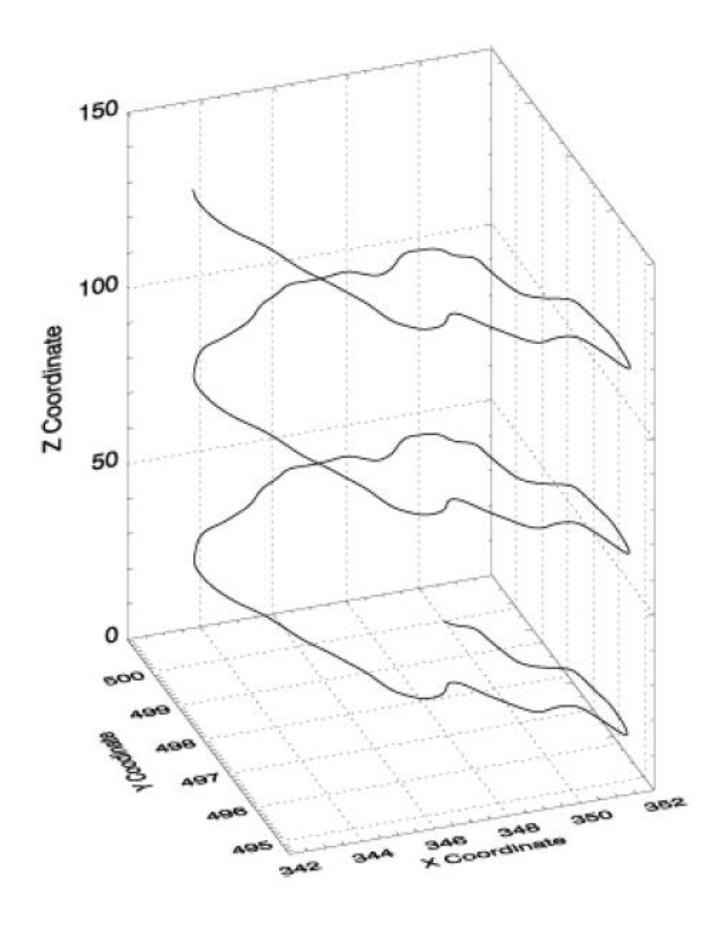


Figure 2.5 Example of a trajectory of a magnetic field line in pure 2D turbulence.

Finally, when we add both slab and 2D turbulence into the mean field, the trajectories of magnetic field lines look like Figure 2.6. In our simulation, to model the 2D+slab turbulence similar to solar wind condition, we usually use 20% of slab turbulence and 80% of 2D turbulence.

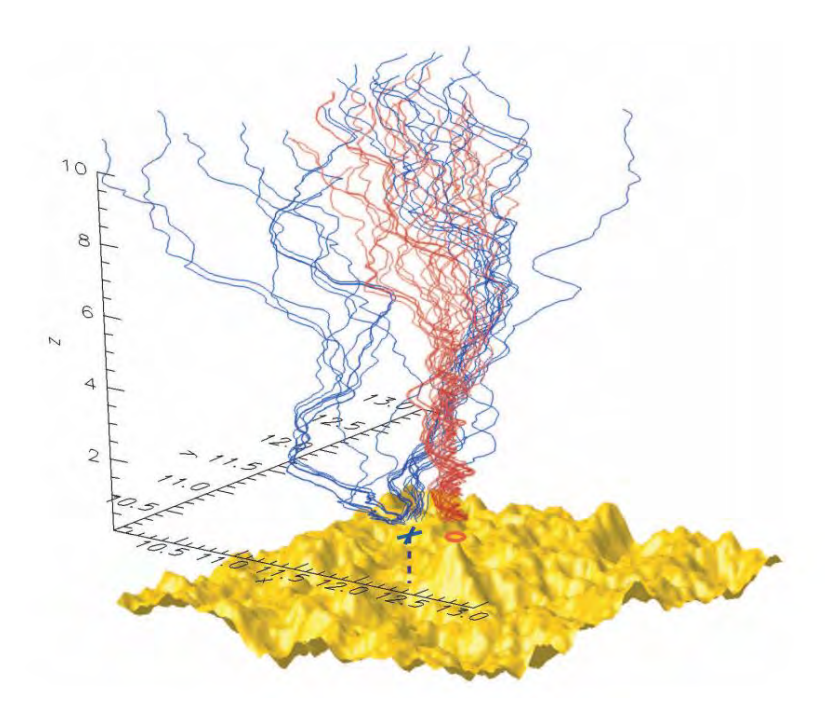


Figure 2.6 Sample of magnetic field lines in 2D+slab magnetic field turbulence that start at the difference locations. The field lines near O-point are trapped along some distance before they diffuse while the field line near X-point quickly spread at the beginning (Chuychai et al. 2007).

II. Simple Gaussian 2D Field

To understand the mechanism of separation between charged particles and their field lines, we also create a simple model for 2D field. For the simple case, we model 2D field as a Gaussian function while the slab field is turbulent (Chuychai et al. 2005; Tooprakai et al. 2007). That would provide us more understanding about the mechanism of the motion of the charged particles when we vary the initial pitch angles. The potential function for simple 2D case can be written as

$$a(r) = A_0 \exp\left[-\frac{r^2}{2\sigma^2}\right],\tag{2.3}$$

where A_0 is the central maximum value, σ determines the width of the Gaussian, and the distance r is measured from the axis of the flux tube. Without the slab field, the field line trajectories in this model, $B_0\hat{z} + \vec{b}_{2D}(x,y)$, have helical orbits along a cylindrical surface of constant a(x,y) with a constant angular frequency as a function of z. The contour of a(x,y) in this model is circle and field line move along the surface of constant a(x,y) as shown in Figure

2.7. Then when we add slab turbulence, the example of trajectories are in Figure 2.8. The field lines start inside 2D island are trapped at the beginning and later become diffusive due to slab turbulence. For the field lines start outside, they quickly spread due to slab turbulence.

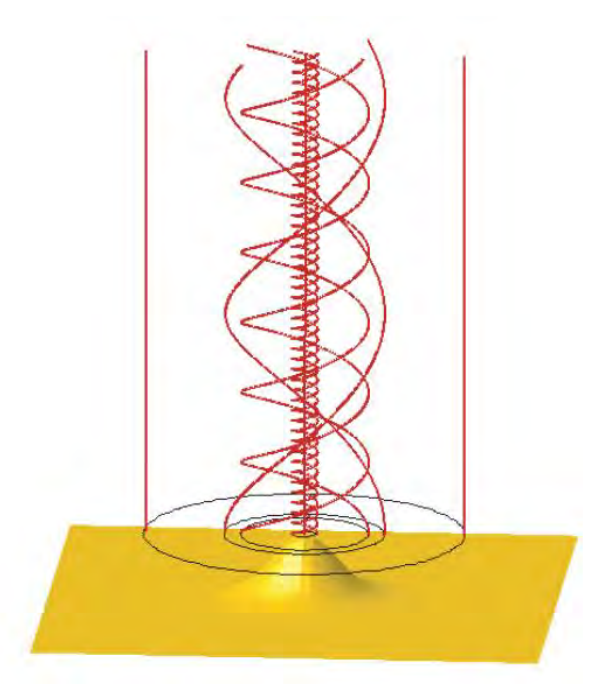


Figure 2.7 Magnetic field line trajectories for a single 2D island, with $\vec{B} = B_0 \hat{z} + \vec{b}_{2D}(x, y)$. The surface plot at bottom shows the potential function a(x, y) of the 2D field (Chuychai et al. 2007).

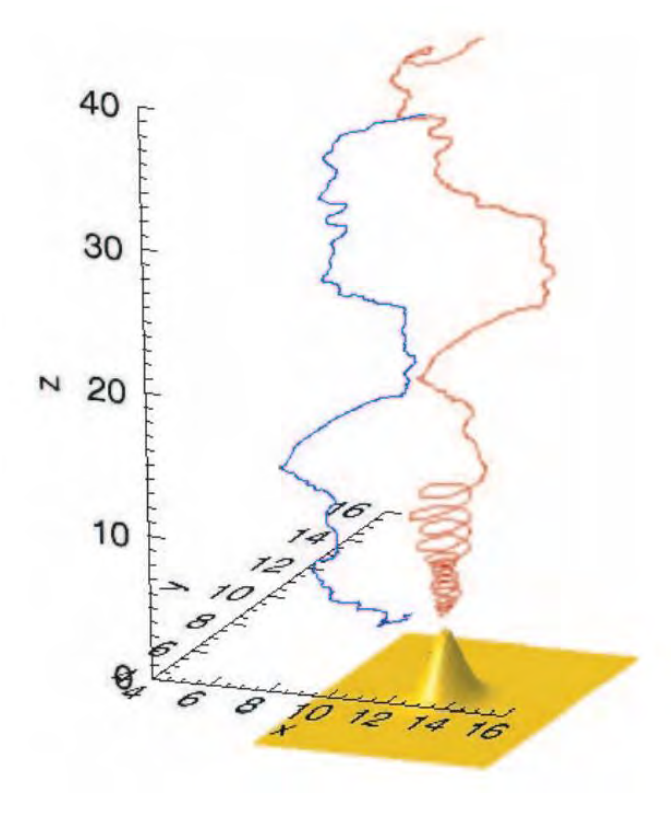


Figure 2.8 Example of two magnetic field lines in a single 2D Gaussian island plus slab turbulence. The red field line started deep inside the island, whereas the blue field line was initially located outside the island. The surface plot at bottom shows the potential function a(x, y) of the 2D field (Chuychai et al. 2007).

2.2 Turbulent Magnetic Field with Taylor Microscale

In this section, we specify the magnetic field with microscale in order to develop the measuring technique and apply to spacecraft data (Chuychai et al. 2014). We use synthetic data generated using a known spectrum, and then employ a typical methodology to evaluate the Taylor microscale. The spectrum is constructed with inertial and dissipation ranges that have been independently controlled, and have generally different power law indices. To be specific, we let the inertial range have a spectral index of -5/3, while the dissipation range has an adjustable spectral index q. The particular functional form of the spectrum is

$$P(f) = \begin{cases} \frac{c}{[1 + (f\tau_0)^2]^{\frac{5}{6}}}, & \text{where } f_{min} < f \le f_d \\ \frac{c}{[1 + (f_d\tau_0)^2]^{\frac{5}{6}}} \left(\frac{f_d}{f}\right)^q, & \text{where } f_d < f \le f_e \\ 0, & \text{where } f_e < f \le f_{max}, \end{cases}$$
 (2.4)

where q < 0 (See the shape of spectrum is presented in Figure 3.1). The reasons for these choices are as follows: First, the flat spectral region at very low frequencies $f\tau_0 \ll 1$ is designed to make the signal time stationary. This is unrealistic for the solar wind, which has very low frequency components due to, eg, solar rotation and solar cycle (see e.g., Matthaeus and Goldstein 1982). However we are not concerned with very low frequency effects here. Second, the inertial range with Kolmogorov spectral index of $\sim 5/3$ is found for higher frequencies, at $f\tau_0 > 1$. Third, there is a discontinuous jump at the top of the inertial range at frequency f_a , the slope steepening from -5/3 to -q, in qualitative accord with observations (Leamon et al. 2008; Alexandrova et al. 2009; Sahraoui et al. 2009). Finally at high frequencies $f > f_e$ we set the spectrum to zero, for numerical rather than physical reasons, to provide a very smooth trigonometric interpolation of the signal at the grid scale.

Adopting illustrative values that are representative of the solar wind at 1AU, we assume that the spectrum starts from $f_{min} = 1.22 \times 10^{-5}$ Hz and is flat until $f_0 = \frac{1}{\tau_0} = 3.906 \times 10^{-4}$ Hz, a "bendover" frequency often associated with the correlation scale or coherence time. Thereafter the spectrum has an inertial range with a 5/3 power law index, until a second break point is encountered at $f_d = 1/\tau_d = 0.4$ Hz. For historical reasons, this breakpoint, which terminates the power law MHD-scale inertial range, is often referred to as the "dissipation scale" (Leamon et al. 1998), although it is also possible that it characterizes dispersion rather than dissipation (Gary and Borovsky 2004). In the hydrodynamic case for which the eddy turnover time and viscous dissipation time scales become equal at the dissipation scale, for the solar wind or other low-collisionality astrophysical plasmas, it is unclear whether the fluctuations become critically damped at the breakpoint/dissipation scale. For example, the inertial range is typically found to terminate near the proton gyroscales, and while some dissipation may occur at such scales, further kinetic plasma dynamics may transfer energy to higher frequencies until much smaller electron scales are encountered (Alexandrova et al. 2009; Sarhaoui et al. 2009). It has been argued that a substantial fraction of actual dissipation may occur due to electrons. In any

case the scale f_d corresponds to the onset of kinetic processes and the end of the Kolmogoroff-like inertial range. It is, however, the kinematic properties of the spectrum that come into play in the current study, rather than the dynamical origin of the spectral forms.

In our model development, beyond the breakpoint f_d , we extend the dissipation range with power law index q until $f_e = 16.0$ Hz which may be considered, in the solar wind application, to be associated with the electron dissipation scale. The spectrum cuts off completely at f_{max} =25.6 Hz. To decide upon these numerical values, here we assume that the dissipation scale and electron dissipation scale correspond to the proton and electron inertial scales, respectively. Thus we set $\frac{f_e}{f_d}$ = 40 to be consistent with the ratio of electron and proton inertial scales in MHD, which is about $\sqrt{m_p/m_e}$ = 42.9 (see e.g., Sahraoui et al. 2009).

Chapter 3

Methodology

We generate magnetic field, which is static and homogeneous by using 2D+slab model of magnetic field turbulence. To study the separation between magnetic field line and charged particle trajectories, we simulate magnetic field lines corresponding to the initial guiding centers of the charged particles by numerically solving field line equation while the trajectories of particles is traced by solving equation of motion. After that the data are collected and analyzed by using new statistical approach. For the part of generating turbulent magnetic field with Taylor microscale, we show the method how to generate the spectrum and transform to time series in real space which are analogous to spacecraft data.

3.1 Generation of magnetic field

3.1.1 Turbulence Magnetic Field

Since the magnetic field in interplanetary is turbulent, we simulate magnetic field by setting up magnetic field parameters and specify power spectrum. In our simulations, we generate the magnetic field in the simulation box. We need to consider the effects of the simulation box, representations of turbulent field, and suitable length scale for simulated field lines. For turbulence case, the magnetic field is generated in wave number space (k-space) before conversion to real space. We instead define the power spectrum as a function in k-space, which is the Fourier transform of the magnetic correlation function $R_{ij}(\vec{r}) = \langle b_i(0)b_j(\vec{r}) \rangle$. The spectrum that we usually use for the magnetic turbulence is a Komolgorov spectrum over a wide range of wave numbers. The magnetic fluctuations in equation (2.1) are composed of slab and 2D turbulence. Because the slab turbulence depends only on z and the 2D turbulence depends on x and y positions, we separately generate them in k_z and (k_x , k_y) spaces, respectively. After that, the magnetic field in Fourier space is converted to position space by an inverse fast Fourier transform. For numerical computation, we cannot generate the magnetic fluctuations continuously in space due to the limitation of the computer. Thus the magnetic field

is constructed only on the grid points in the simulation box. To avoid bias due to a periodicity effect, we have to generate the magnetic field in a large (but finite) box. Therefore, in this part, the parameters that we need to input are the sizes in x, y, and z directions of the simulation box (L_x , L_y , and L_z), the number of grid points (N_x , N_y , and N_z), the total root-mean-squared fluctuation (δb), the fraction of 2D and slab energy, the shapes of the 2D and slab power spectra, and coherence lengths (λ_z an λ_\perp).

Slab Turbulence

For slab turbulence, we set the power spectrum for simulations as

$$P_{xx}^{slab}(k_z) = P_{yy}^{slab}(k_z) = \frac{C^{slab}}{[1 + (k_z \lambda)^2]^{5/6}},$$
 (3.1)

where C^{slab} is a normalization constant that depends on the slab energy and λ is the parallel coherence length. From the function of the slab spectrum, the slab magnetic fluctuations in k_z space are

$$b_x^{slab}(k_z) = \sqrt{P_{xx}^{slab}(k_z)} \exp[i\phi(k_z)]$$
 (3.2)

$$b_y^{slab}(k_z) = \sqrt{P_{yy}^{slab}(k_z)} \exp[i\phi(k_z)], \tag{3.3}$$

where ϕ is a random phase number and k_z is a discrete number which is $k_z = j2\pi/L_z$, for $j = 1, 2, 3, ..., N_z/2 - 1$.

2D Turbulence

For 2D turbulence, we instead specify the power spectrum $A(k_x, k_y)$ because the power spectra $P_{xx}^{slab}(k_x, k_y)$ and $P_{yy}^{slab}(k_x, k_y)$ can be written in terms of $A(k_x, k_y)$ as

$$A(k_{\perp}) = \frac{c^{2D}}{[1 + (k_{\parallel}\lambda_{\perp})^2]^{7/3}}.$$
 (3.4)

From the relationship between magnetic fluctuation and potential function in k-space, the 2D fluctuations in (k_x, k_y) are

$$b_x^{2D}(k_x, k_y) = -ik_y \sqrt{A(k_\perp)} \exp[i\phi(k_x, k_y)]$$
(3.5)

$$b_y^{2D}(k_x, k_y) = ik_x \sqrt{A(k_\perp)} \exp[i\phi(k_x, k_y)], \qquad (3.6)$$

3.1.2 Simple Gaussian 2D Field

Since we can specify the function of simple Gaussian 2D Field directly in real space. From equation (2.3), we write potential function in Cartesian coordinate

$$a(x,y) = A_0 \exp\left[-\frac{(x-x_0)^2 + (y-y_0)^2}{2\sigma^2}\right],\tag{3.7}$$

where x_0 and y_0 are center of the Gaussian island. From the relationship $\vec{b}_{2D} = \vec{\nabla} a(x, y) \times \hat{z}$, we can write

$$b_x = \frac{\partial a(x, y)}{\partial y} = \frac{-(y - y_0)a(x, y)}{\sigma^2}$$
(3.8)

$$b_{y} = -\frac{\partial a(x,y)}{\partial x} = \frac{(x - x_{0})a(x,y)}{\sigma^{2}}.$$
(3.9)

3.1.3 Turbulent Magnetic Field with Taylor Microscale

Once we have specified the shape of spectrum as equation (2.4), we can generate realizations of the signal in the frequency domain, F(f), as

$$F(f) = \sqrt{P(f)} \exp[i\phi]$$
 (3.10)

where ϕ is a random phase. Then a fast Fourier transform (FFT) is used to convert the function F(f) into the real time domain. In the simulations reported here, we employ this approach to obtain 2^{22} data points for the time series.

We next compute the Taylor microscale from the data set we generated by employing the definition equation (2.4). In Table (3.1), we give the Taylor microscale values for a range of dissipation scale indices q corresponding to the generic power spectrum shown in Figure 3.1. (Note that the spectra are given here as Fourier amplitudes squared, which can easily be converted to power spectral density.) We will treat these expected values of the Taylor microscale as the true or exact Taylor microscale values for the synthetic time series data. To examine and test our extrapolation method, we use only one-eighth of the original data. The

purpose of defining this subset is that any consistent method will provide good (and even convergent) values of τ_{TS} when the time resolution Δt of the estimates is very fine, i.e., the spectral cutoff is resolved and $\Delta t f_{max} < 1/2$. However, our motivation is to obtain reasonably accurate values of τ_{TS} when the effective resolution of the data sampling is adjusted so that we are not in this asymptotic regime – a circumstance that is more likely to be realized in practice when analyzing spacecraft data.

With the subset of our discrete time series, we compute the second order structure function. This can be used to obtain an estimate of the correlation function. We then determine the radius of curvature from correlation function and an estimate of the Taylor microscale. In the following section, we will demonstrate an extrapolation technique (Weygand et al. 2007, 2009, 2010, 2011) to estimate Taylor microscale from a series of parabolic fits of the correlation function near the origin. The details of the technique we use to analyze are given in Chapter 6.

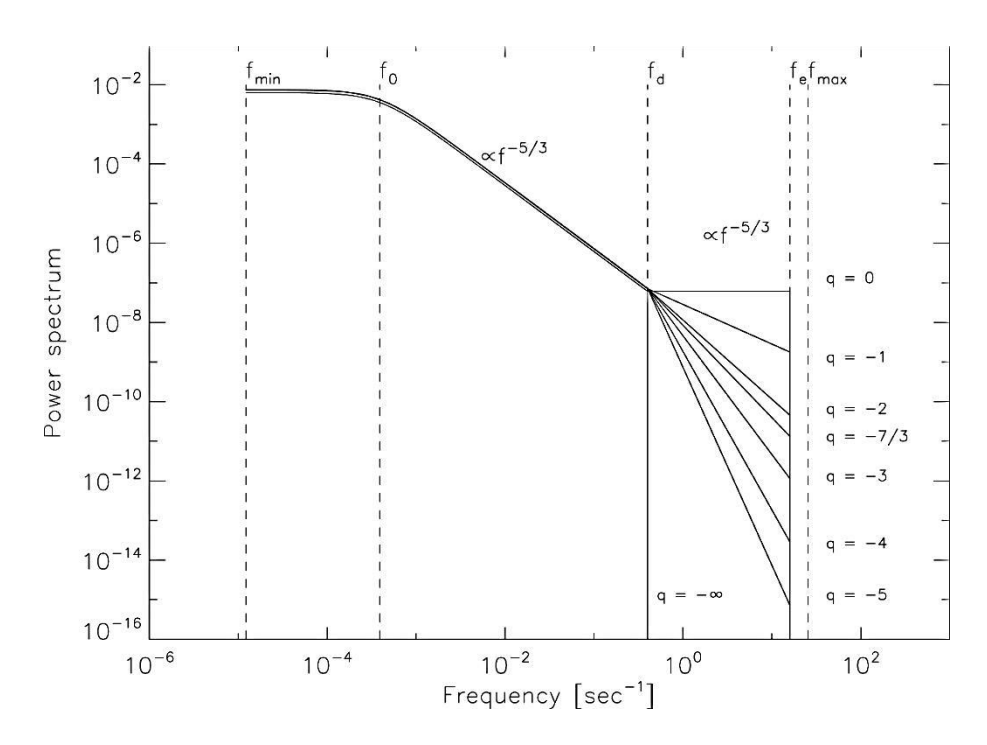


Figure 3.1 The power spectrum for a number of values of q in the dissipation range.

Table 3.1 Showing index q which we vary for each case and their Taylor scales when we fix dissipation scale ($\tau_d = 2.5 \text{ s}$).

Case	$ au_{TS}^{expect}$ [s]	$ au_{TS}^{expect} \left[au_d ight]$
$q = -\infty$	6.569	2.63
q = -5	5.097	2.04
q = -4	4.368	1.75
q = -3	2.869	1.15
q = -7/3	1.607	0.64
q = -2	1.095	0.44
q = -1	0.095	0.028

3.2 Particle Simulations

For the charged particle q and mass m, moving with velocity (\vec{v}) a magnetic field (\vec{B}) , without electric field (\vec{E}) , we can write motion equation by Newton's Lorentz force (\vec{F}_B) :

$$\vec{F}_B = m \frac{d\vec{v}}{dt} = q(\vec{v} \times \vec{B}). \tag{3.11}$$

For our work, we a bit adapt equation (3.11) for simulation (Tooprakai et al., 2007),

$$\frac{d\vec{v}'}{dt'} = \alpha(\vec{v}' \times \vec{B}'),\tag{3.12}$$

where $\alpha = (qB_0\tau_0)/(\gamma m_0)$ and the quantities \vec{v}' , \vec{B}' , and t' are normalized quantities which have units as scale to the speed of light (c), the mean magnetic field (B_0) , the time scale $\tau_0 = \lambda/c$, respectively. Note that λ is the slab turbulence coherence length.

We can find trajectories of the charged particles, when we know the equation of motion of the charged particles. In this work, we use Newton's Lorentz force equation to find positions of the charged particles by using fourth-order Runge-Kutta method with adaptive time stepping regulated by a fifth-order error estimate step (Press, Teukolsky, Vetterling & Flannery, 1992; Dalena, Chuychai, Mace, Greco, Qin & Matthaeus, 2012).

3.3 Magnetic Field Line Simulations

When we know the value of the magnetic field at each grid point, we can trace the magnetic field line that is tangent everywhere to the magnetic field (\vec{B}) . The differential equation of the magnetic field line is

$$d\vec{l} \times \vec{B} = 0. \tag{3.13}$$

In Cartesian coordinates, $d\vec{l}$ is (dx, dy, dz) and \vec{B} is (B_x, B_y, B_z) . From equation (3.13), it can be written as

$$\frac{dx}{B_x} = \frac{dy}{B_y} = \frac{dz}{B_z}. (3.14)$$

In our model, we use $\vec{B} = B_0 \hat{z} + b_x \hat{x} + b_y \hat{y}$ so we obtain

$$\frac{dx}{B_x} = \frac{dy}{B_y} = \frac{dz}{B_0}. (3.15)$$

Finally, we can write the differential equation for the magnetic field line as

$$\frac{dx}{dz} = \frac{b_x(x, y, z)}{b_0} = \frac{b_x^{slab}(z) + b_x^{2D}(x, y)}{B_0}$$
(3.16)

$$\frac{dy}{dz} = \frac{b_y(x, y, z)}{b_0} = \frac{b_x^{slab}(z) + b_x^{2D}(x, y)}{B_0}$$
(3.17)

After that the differential equation of the magnetic field line is solved by using fourth order Runge Kutta method with adaptive step size as same as we use in particle simulation to find positions of the magnetic field lines x_{FL} , y_{FL} , z_{FL} .

3.4 Simulation and Analysis Method for Separation between Charged Particles and Field Lines

We simulate 1,000 pairs of particle trajectories (protons) and their initial field lines with starting points located at the initial guiding center (GC) of the particles. As the trajectories of the particles are traced by equation (3.12), their GCs are also computed from the radius of curve of the particle orbits, $\vec{\rho}$:

$$\vec{\rho} = \frac{\vec{B} \times \vec{p}}{qB^2},\tag{3.18}$$

where $\vec{p} = \gamma m_0 \vec{v}$ is the particle momentum. From the radius of curvature and the particle position, we can find the GC from $\vec{r}_{GC} = \vec{r} - \vec{\rho}$ as shown in the Figure 3.2.

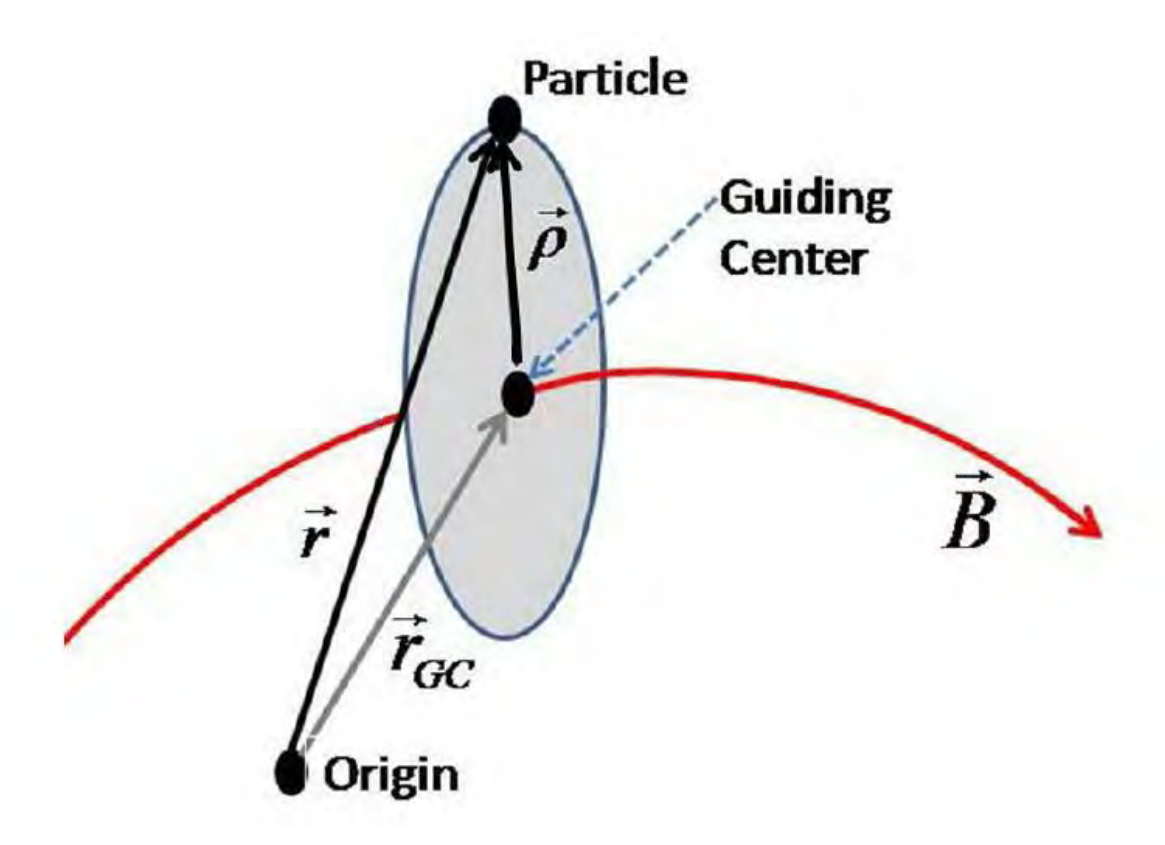


Figure 3.2 Illustration of a particle orbit, magnetic field line and guiding center (Wikee 2013).

After that, we analyze the statistics of spreading between particles and field lines by calculating the mean squared displacement between the position of a particles GC and its field line at the same *z*-coordinate (see Figure 3.3), as a function of time, that is

$$\langle (x_{GC}(t) - x_{FL}[z(t)])^2 \rangle \text{ and } \langle (y_{GC}(t) - y_{FL}[z(t)])^2 \rangle, \tag{3.19}$$

where z(t) is the z-coordinate of the particle GC at time t. Note that x_{FL} and y_{FL} are single valued because we assume transverse fluctuations, so $B_z = B_0$ constant and the field line cannot back track in z. We use linear interpolation to evaluate x_{FL} and y_{FL} at z coordinate of the particle GC at regular time intervals.

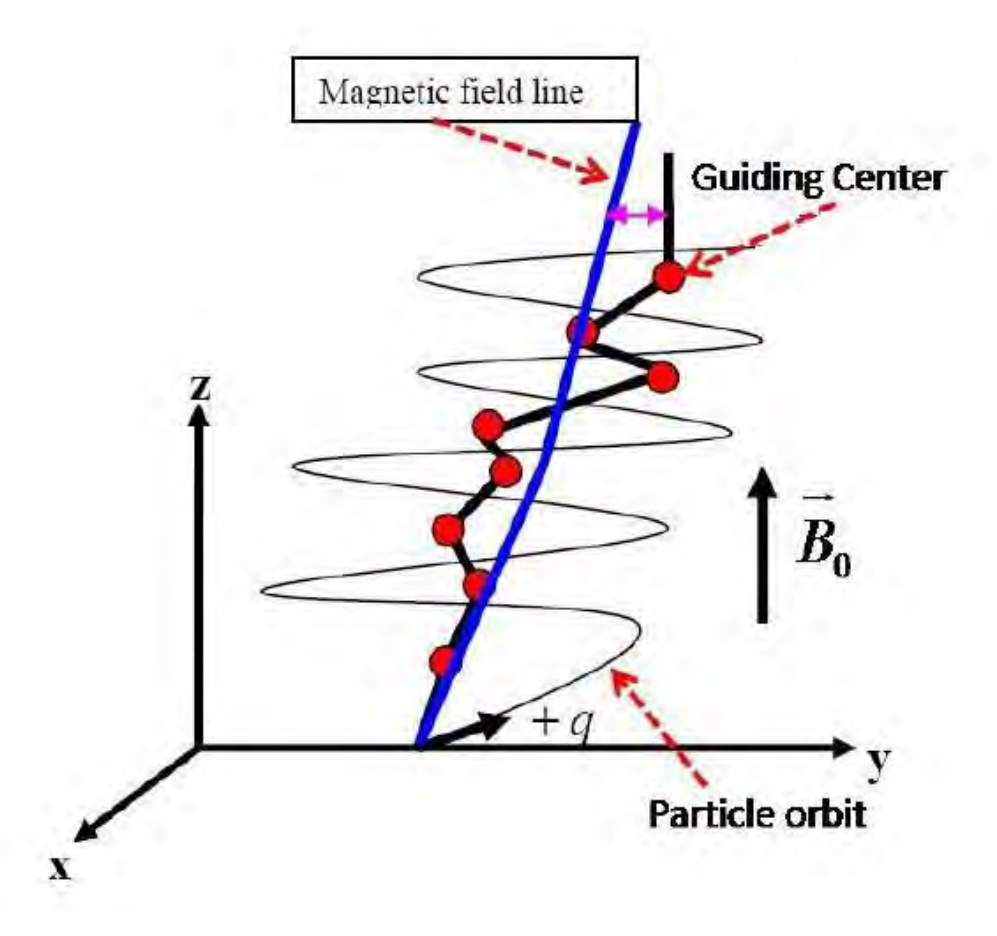


Figure 3.3 The diagram of separation between the guiding center and magnetic field line (Wikee 2013).

Chapter 4

Effect of Reduced Dimensionality of the Magnetic Field Fluctuations on the Cross-Field Motion of Charged Particles

In interplanetary space, the transport of energetic charged particles is influenced by a turbulent magnetic field. Previous studies have shown that a two-component (2D+slab) magnetic model (Matthaeus, Goldstein, and Roberts 1990; Bieber, Wanner, and Matthaeus 1996) of turbulence is a useful model for the magnetic field in the heliosphere. Normally, the diffusive behavior of charged particles in a turbulent magnetic field is observed when they approach the long time limit. The charged particles are often assumed to follow and diffuse according to the random walk of the field lines but some theories of perpendicular particle transport, such as nonlinear guiding center theory (NLGC) (Matthaeus et al. 2003; Ruffolo et al. 2008; Ruffolo et al. 2012), implicitly assume some true cross-field diffusion in which particles separate from the field line connected to their initial location. Furthermore, such cross-field diffusion is of specific interest because it is the only way that particles can diffuse across boundaries of magnetic field topology, such as the heliospheric current sheet and boundaries of interplanetary magnetic flux ropes. Jokipii et al. (1993) and Jones et al. (1998) derived a theorem showing that charged particles in an arbitrary electromagnetic field with at least one ignorable spatial coordinate remain forever tied to a given magnetic flux surface. In this work, we consider charged particles in one- and two-component magnetic fields to illustrate the effect of reduced dimensionality of magnetic fluctuations on the cross-field motion. A simple 2D flux tube and slab turbulence are used for fluctuations with we can turn the dimensionality on and off.

4.1 Simulation Setup

In the simulation, we set the box length in the z direction as $10,000\lambda$ and the number of grid points is $N_z = 4,194,304$. The magnetic parameters are $\delta B_{slab}/B_0 = 0.5$, $\sigma = 0.5\lambda$, and $A_0 = 0.8436B_0\lambda$.

The 100 MeV protons were released in random direction distribution. There are three cases that we have explored in our work: particle motion in a pure 2D field, in pure slab turbulence and in 2D+slab fields. These three cases can demonstrate the effect of reduced dimensionality of the magnetic field fluctuations. That is a reduction to one dimensionality can be studied in the case of pure 2D field with azimuthal symmetry $[B_0\hat{z} + \vec{b}_{2D}(r)]$ and in the case of pure slab turbulence $[B_0\hat{z} + \vec{b}_{slab}(z)]$. The 2D+slab case represents fully three dimensional fluctuations. Note that in our results all length scale is in unit of λ and time is in unit of λ/c .

4.2 Results

Case I: Particles in the pure 2D field

We inject all 1,000 protons of 100 MeV at a random angles along certain initial radius (r_0) of the 2D flux tube. The results are shown in Table 1 and Figure 1 for $r_0 = 0.5\lambda$. From the results, we found that $\langle (x_{GC}(t) - x_{FL}[z(t)])^2 \rangle \sim r_0^2$. It can be explained by the drift motion in the azimuthal direction (z direction) while the particles still stay near the flux surface. Figure 4.2 shows similar results for 10 MeV particles started at $r_0 = 0.1\lambda$).

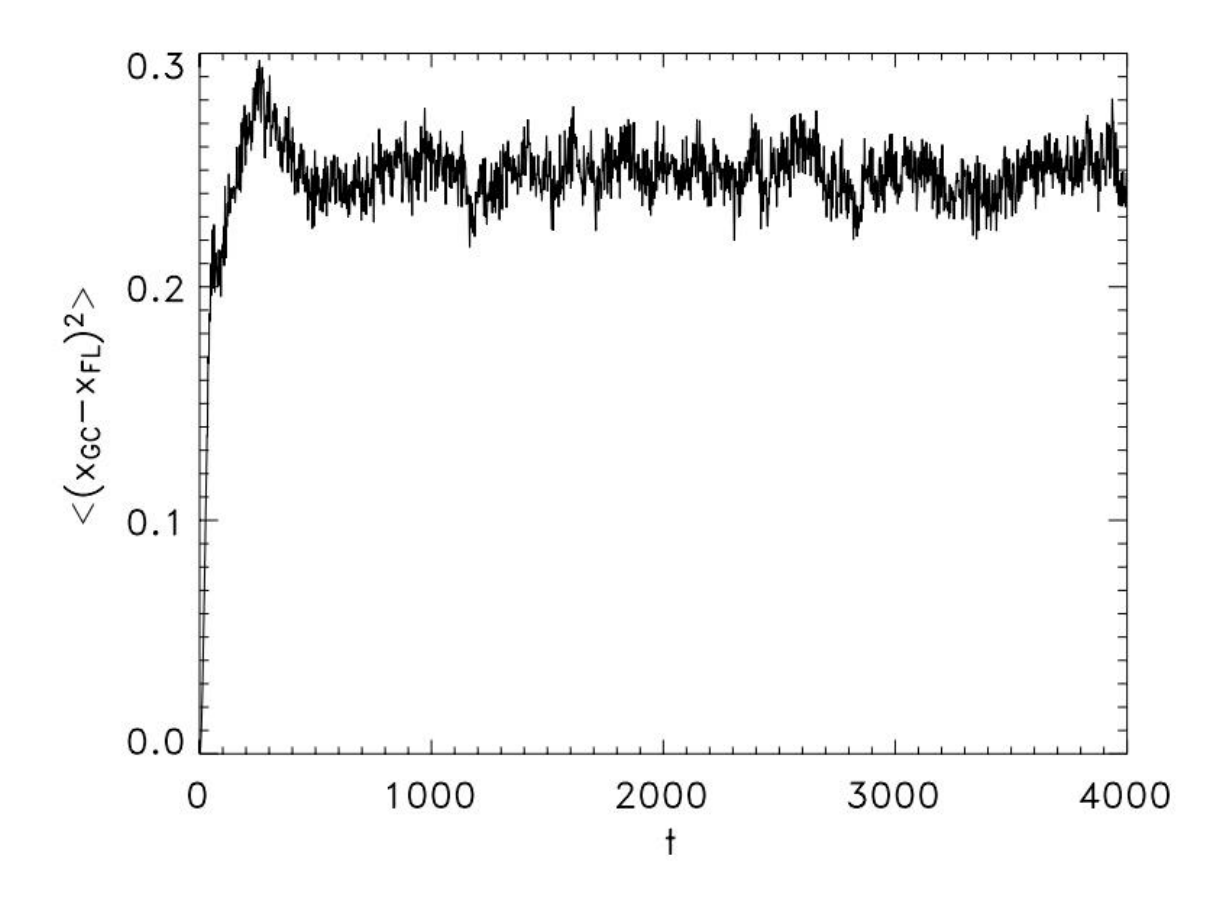


Figure 4.1 The mean squared separation between guiding centers of 100 MeV particles starting at $r_0 = 0.5\lambda$ with their field lines in the pure 2D field. The value close to r_0^2 implies confinement to flux surface.

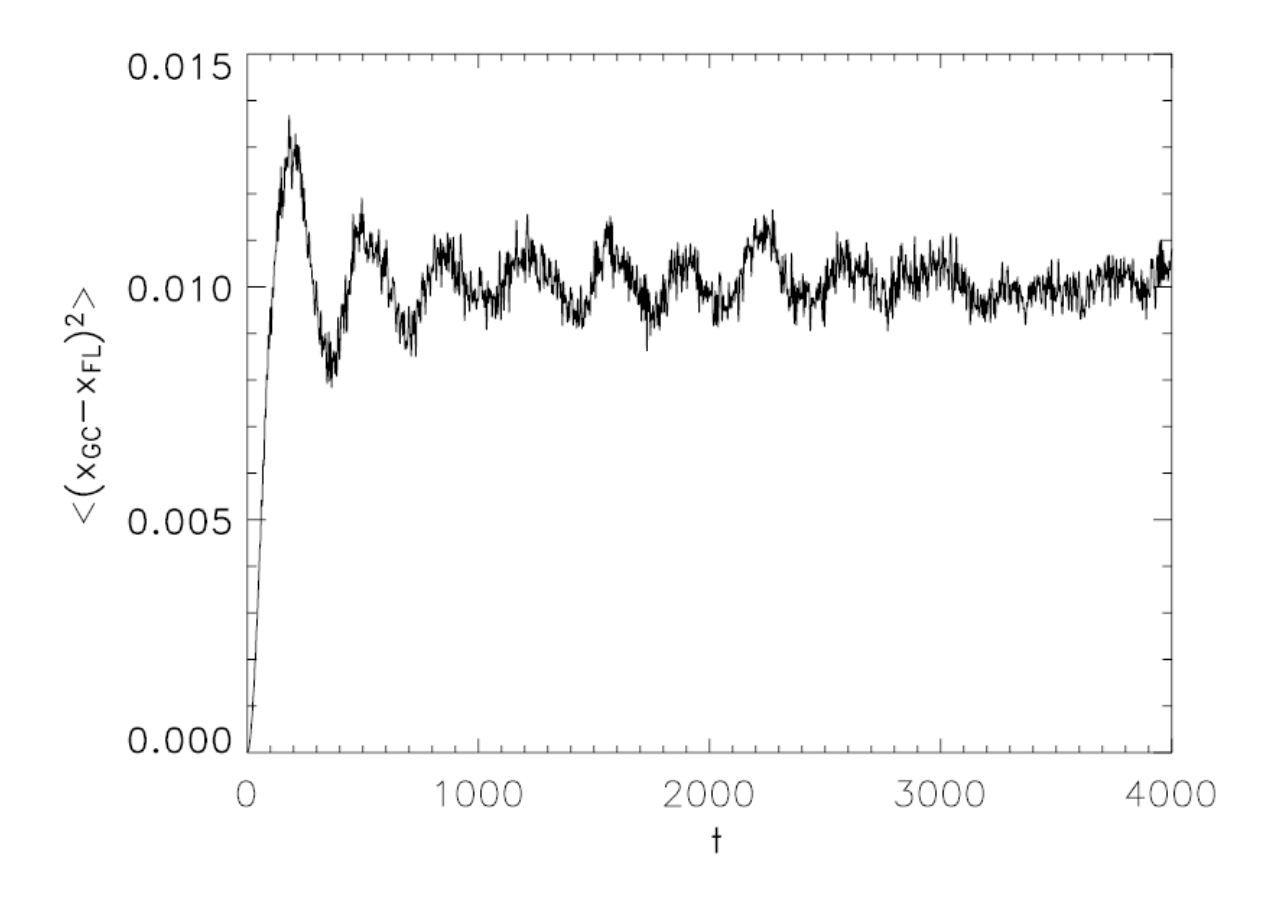


Figure 4.2 The mean squared separation between guiding centers of 10 MeV particles starting at $r_0 = 0.1\lambda$ with their field lines in the pure 2D field.

Table 4.1 Saturation values for 100 MeV particles in the pure 2D field when we vary the location of the initial positions.

r_0	$\langle (x_{GC} - x_{FL})^2 \rangle$	$\langle (y_{GC} - y_{FL})^2 \rangle$
0.1	0.0149	0.0149
0.3	0.0900	0.0902
0.5	0.249	0.250
0.7	0.492	0.493
0.9	0.825	0.826

Case II: Particles in slab turbulence

In this case, the particles are started at random positions in the simulation box. The results in Figure 4.3 show that the particles in slab turbulence have very little separation for their field lines. The particles stick with their initial field lines.

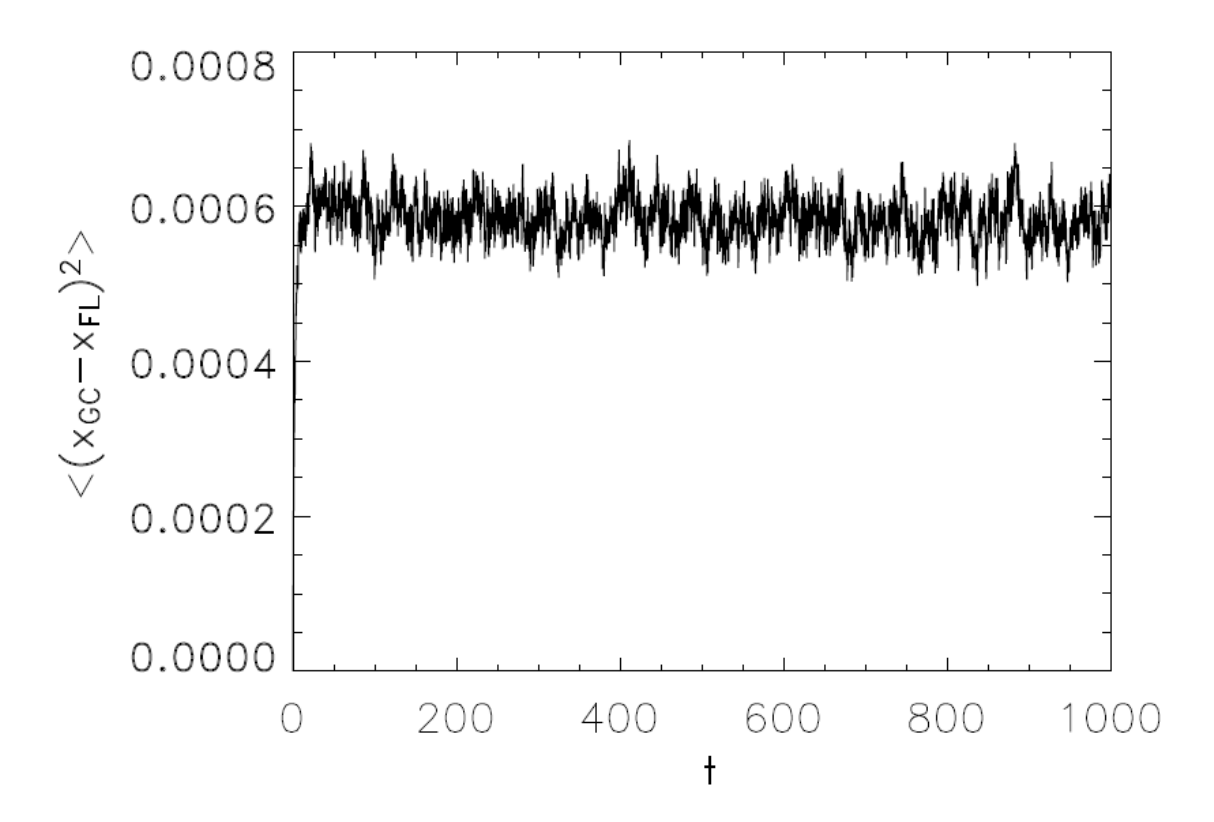


Figure 4.3 The mean squared separation between guiding centers of 100 MeV particles and their field lines in pure slab turbulence. The low value indicates confinement of the particle to remain near the same field line.

Case III: Particles in 2D+slab fields

In the case of three dimensional fluctuations, we can see that the particles have unconstrained cross-field motion illustrated in Figure 4.4.

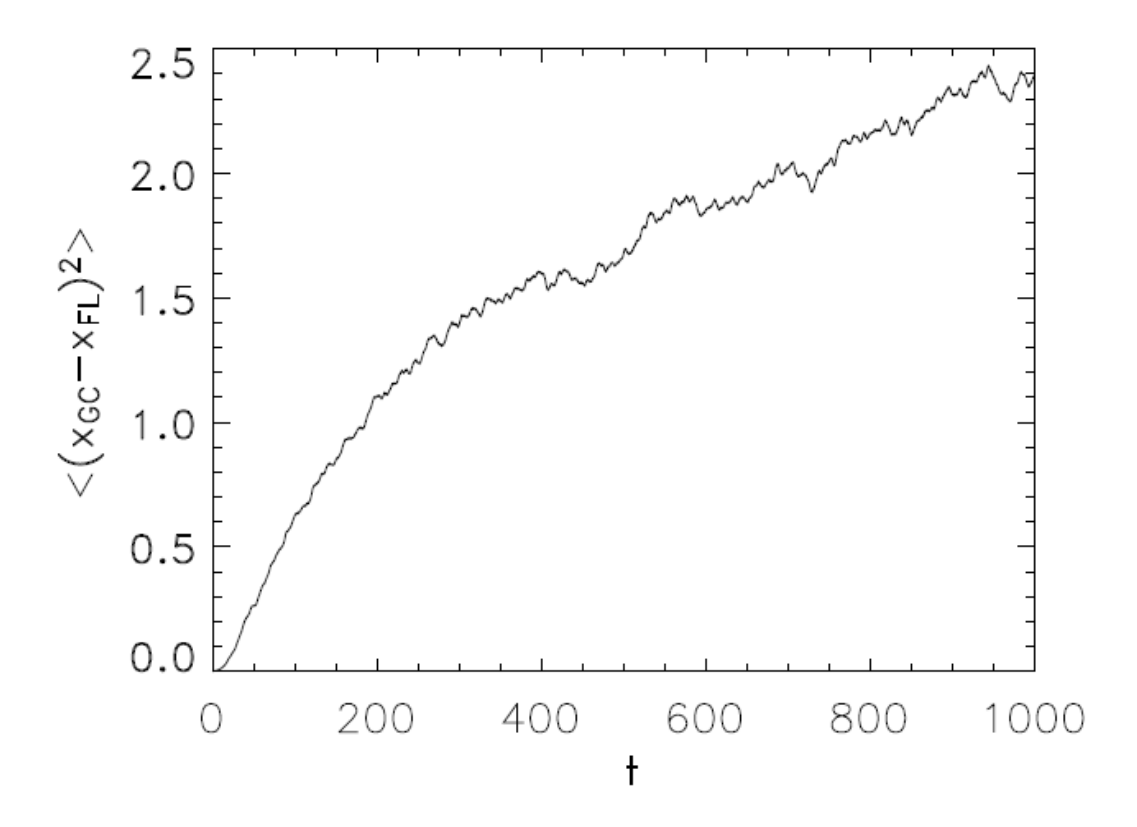


Figure 4.4 The mean squared separation spreading between guiding centers of 100 MeV particles and their field lines in Gaussian 2D field + slab turbulence. The continual increase indicates unconstrained cross-field motion in this fully three-dimensional case.

4.3 Conclusions and Discussion

We have examined the cross-field motion of particles in the one- and two-component magnetic field models. Our results show the effect of reduced of dimensionalities of the magnetic fluctuations on the cross-field motion. When the fluctuations have two ignorable coordinates in one case (pure slab), no cross-field motion can be observed, with particles constrained to remain near one field line, and in another case (pure 2D with azimuthal symmetry), the particles are constrained to remain near on-flux surface. Unconstrained cross-field motion occurs only when the magnetic field has fully three dimensions. These results are consistent with the theorem of Jokipii et al. (1993) and Jones et al. (1998) which states that in an

EM field with an ignorable coordinate, the particle motion remains near a single magnetic flux surface. The particles in the pure slab case stick to their initial field lines because the theorem applied to the ignorable x coordinate constrains the particle to one magnetic flux surface, application to the ignorable y coordinate constrains the same particle to a different flux surface, and the intersection of the two surfaces in simply the original field line. For the pure 2D case, application of the theorem to the ignorable coordinate z coordinate implies a constraint to remain near a flux surface of constant r, which is the same surface. Thus there is no further constraint from the second application of the theorem, the particles are confined on the flux surface but have the drift motions in the z (or ϕ) direction that cause the saturate values in our statistics approximately r_0^2 . This study will help us to understand the cross-field motion of energetic particles in interplanetary space and will play an important role in developing the transport theory of charged particles in magnetic turbulence.

Chapter 5

Separation of Charged Particles from Their Turbulent Magnetic Field Lines

In this chapter we explore the separation of charged particles and magnetic field lines in two cases which are Guassian 2D Field + slab turbulence and 2D+slab turbulence. For simple case, we release the particles at various distances from the center of Guassian island and then study behavior for each case. For 2D + slab turbulence, we vary particle energy, 2D fraction, initial pitch angle, and the fluctuation strength in order to see the effect of separation.

5.1 Separation of Charged Particles and Field Lines in Guassian 2D Field + Slab Turbulence

The 1000 charged particles are released at random initial pitch angles on various distances from the center of the 2D Gaussian island (r_0) as $0.1\lambda, 0.3\lambda, 0.5\lambda, 0.7\lambda$, and 0.9λ (Wikee 2013). For Gaussian function of potential function, we set the width of the Gaussian σ as 0.5λ . We define $b_{2D}^{max}/B_0=1.0$ and $(b_{2D}^{max}/\delta b_{slab})^2=20$ that means the 2D flux tube is very strong compared with slab turbulence. The test particles are designed to represent protons that have energy 100 MeV. In our simulations, all units of lengths are scaled with λ and the unit of the time is scaled by λ/c . Figure 5.1 shows the example of the trajectory of the test charged particle and magnetic field line.

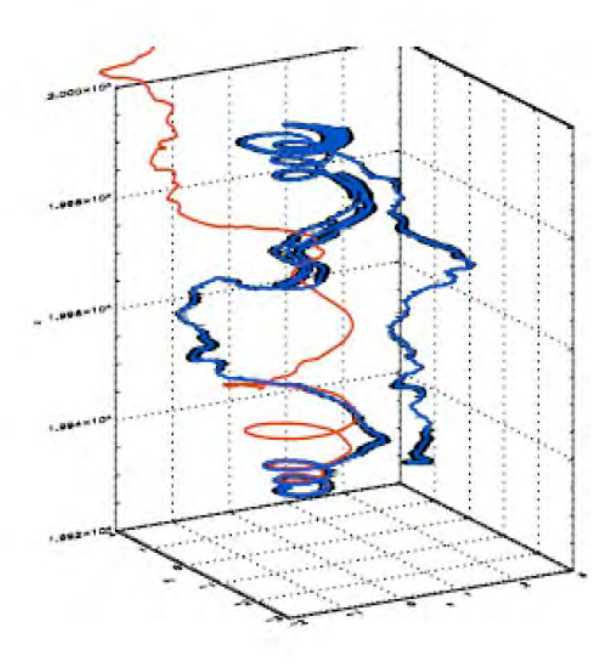


Figure 5.1 Example of the trajectory of a charged particle in our model; red line demonstrates trajectory of magnetic field line, black line and blue line demonstrate trajectories of charged particle and its guiding centers, respectively.

In our work, the simulation results for 1,000 particles show that the separation behaviors between the charged particles and the corresponding field lines can be divided into several regimes as we can see in Figure 5.2. We can explain the mechanism of separation in each regime by relating to the structure of the 2D Gaussian and slab turbulent magnetic field.

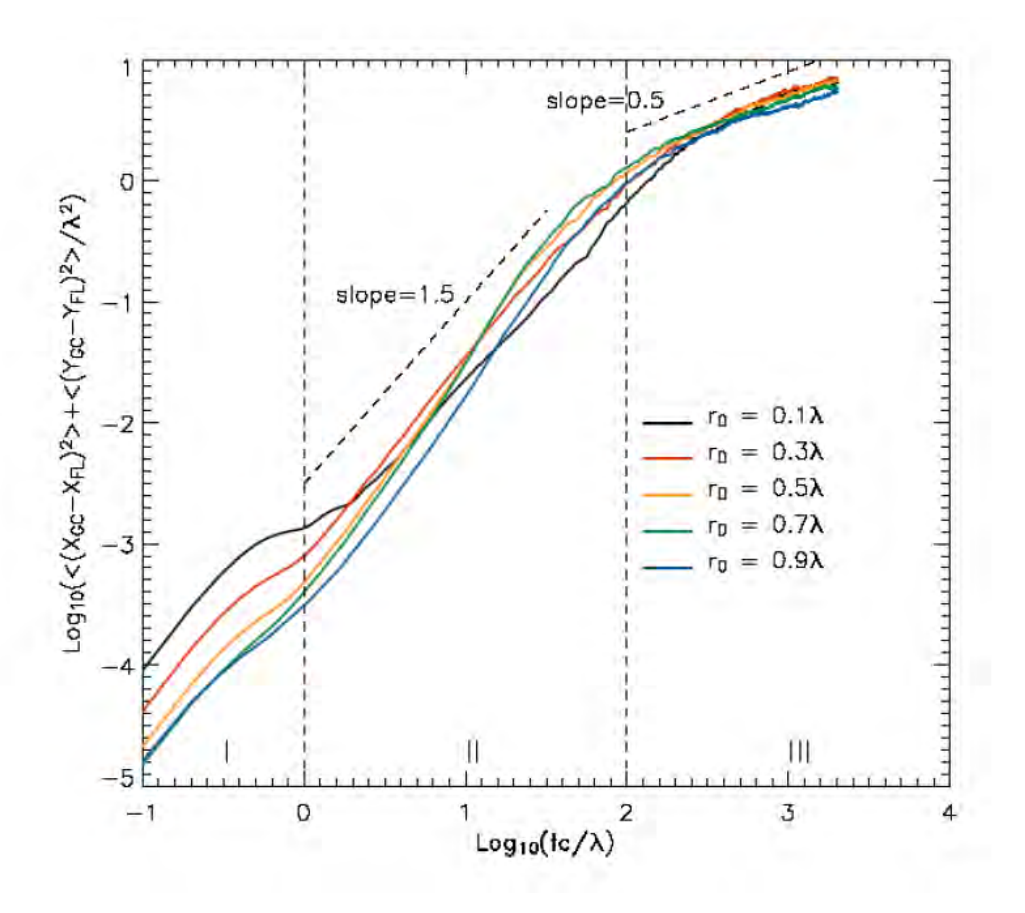


Figure 5.2 The results of the separation of charged particles and their corresponding field lines in the log-log scale.

I. At the initial times (when $tc/\lambda < 1$)

We found that the separation of the charged particles in initial time which are started at the radius of 0.1λ is highest one following by the ones started at 0.3λ and 0.5λ , respectively. For the particles started at 0.7λ and 0.9λ , the separations are very close to each other and lower than the particles started $r_0 = 0.5\lambda$. It seems that the separation of charged particles during this time depend on the structure of 2D field which can be explained by the radius of curvature of the magnetic field and the gradient of magnetic field. The positions of 0.1λ from center of Gaussian function have the lower radius of curvature of the magnetic field lines than the radii as 0.3λ , 0.5λ , 0.7λ and 0.9λ . The curvature is larger when the distance is far from the center. For the gradient of magnetic field, we can see from the profile of the intensity of 2D Gaussian flux can

be seen in Figure 5.3. The gradient depends on the radius from the center of Gaussian 2D field. The maximum of 2D magnetic field is at the width of Gaussian function (σ) and the decrease when the radius towards to the center as well as when they go outside. Next, we compute the effect of curvature and gradient drifts due to 2D Gaussian field in order to explain the results during the beginning time. In general, the drift velocity of guiding center due to the gradient of the magnetic field is represented by

$$\vec{v}_G = \frac{v_\perp^2}{2\omega_c} \frac{\vec{B} \times \nabla \vec{B}}{B^2} \tag{5.1}$$

while the curvature drift is

$$\vec{v}_c = \frac{\gamma m v_{//}^2}{q B^2} \frac{\vec{R}_c \times \vec{B}}{R_c^2}.$$
 (5.2)

Then we plug in the pure Gaussian 2D magnetic field including mean field into equations (5.1) and (5.2) and compute the drift velocity. Then we can find that the magnitude of drift velocity of the guiding center due to the gradient and the curvature drift of the magnetic field are

$$\|\langle \vec{v}_G \rangle\| = \frac{\gamma m v^2}{3q\sigma^2 R_c} \frac{b^{2D}}{B^2} |\sigma^2 - R_c^2|$$
 (5.3)

$$\|\vec{v}_C\| = \frac{\gamma m v^2}{3qR_c B}.\tag{5.4}$$

Then when we consider both effects, the equation for these is

$$\|\langle \vec{v}_G \rangle + \langle \vec{v}_C \rangle\| = \frac{\gamma m v^2}{3qBR_c} \left[\left[\left(\frac{b^{2D}(R_c)}{B\sigma^2} \right) (\sigma^2 - R_c^2) + 1 \right] \right]. \tag{5.5}$$

After that, we insert all magnetic field parameters in our simulation into equations (5.3), (5.4), and (5.5) and make a map to see the effect of the drift for each radius from the center of Gaussian. We found that they give the shapes of drift speed like Figure 5.4. From the drift speed profile, we can see that the curvature drift has more effect than the gradient drift and it is dominated at the small radius from the center of the Gaussian function. When we combine these two effects as in equation (5.5), the particles started near the center of the Gaussian have more drift speed due to 2D field. That is why we can see the charged particles have high separation of

the charged particles when they are released at the small radius as shown in Figure 5.2. Moreover, from the profile in Figure 5.4, the effect of the drift for the particles started at 0.7λ and 0.9λ is slightly different which we can also see this effect in Figure 5.2.

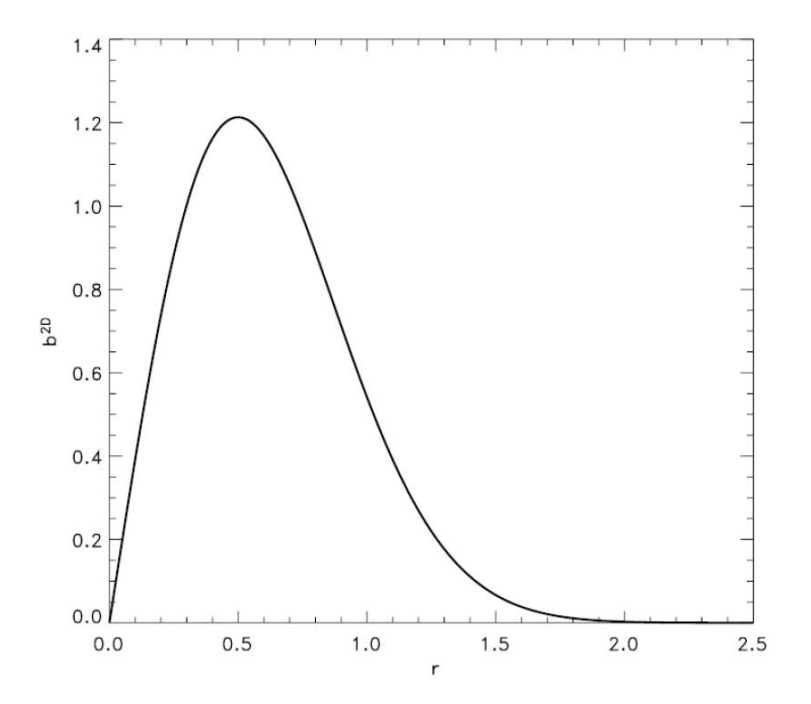


Figure 5.3 The profile of the 2D Gaussian magnetic field along the distance from the center of the flux tube.

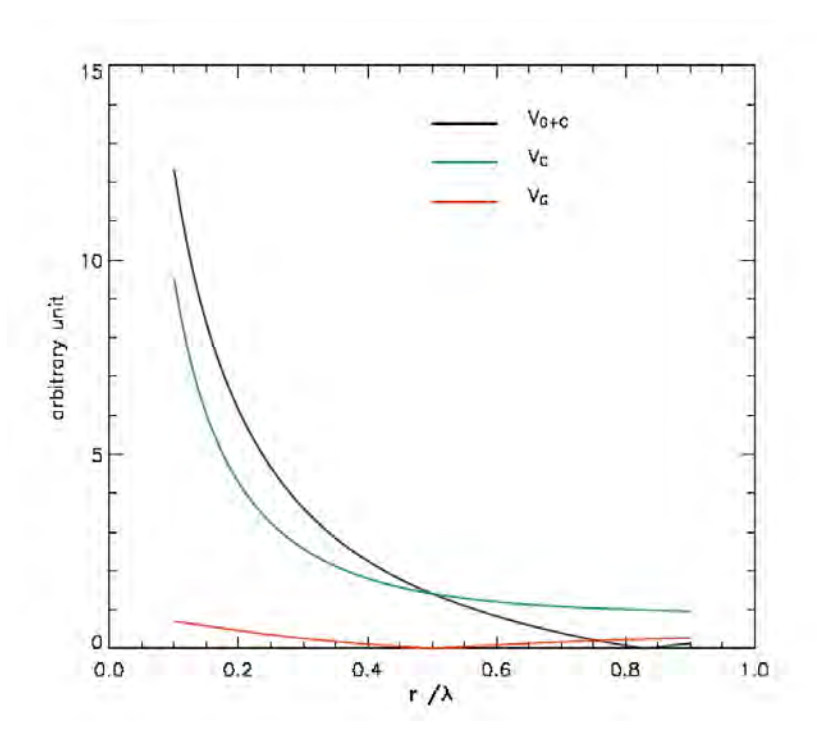


Figure 5.4 Showing shape of drift speed of guiding center due to the gradient of the magnetic field, radius of curvature of the magnetic field line and the summation of the gradient drift and curvature drift in arbitrary units.

II. At intermediate time (when $1 \le tc/\lambda \le 100$)

In this regime, the charged particles follow their corresponding field lines for a while and start to escape from the influence of the 2D flux tube. There are interesting features in this regime. The particles started deeper inside the 2D island have lower separation during this time and the particles started outside 2D island have almost the same slope of the separation. The particles start at $r_0 = 0.1\lambda$ and 0.3λ , at inside 2D islands, have lower separation rate than the others as shown in Figure 5.5a). Here, we can recognize the separation rate by the slope of the graph. The particles started deep inside the 2D island slowly drift out from the field lines because both field lines and the charged particles are trapped inside 2D island. For the behaviors of the particles released outside the 2D island such as at $r_0 = 0.5\lambda$, 0.7λ and 0.9λ , they have almost the same separation rate and there is more the separation rate than the particles started at inside 2D island as shown in Figure 5.5b). That is because these particles quickly move outside and are not

trapped due to the strong 2D field. This corresponds with the suppression of field line and particle diffusion when there is a strong 2D magnetic field as found in previous work (Chuychai et al., 2005, 2007; Tooprakai et al., 2007).

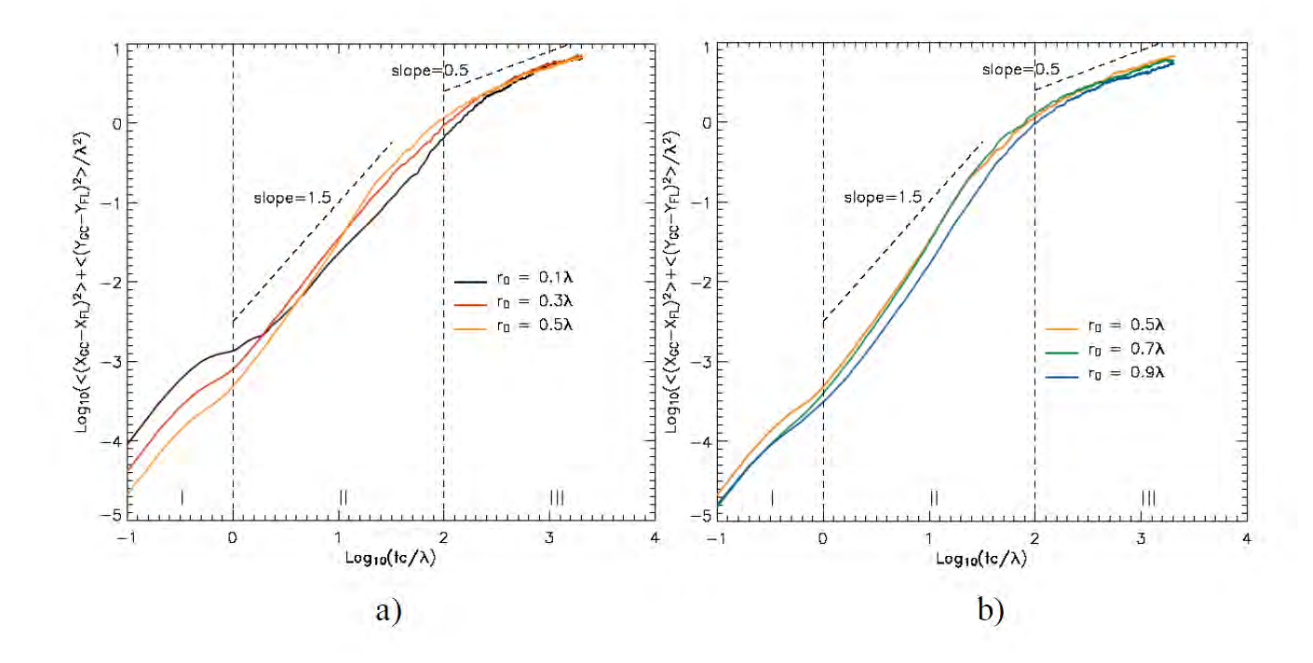


Figure 5.5 Showing the separation of the charged particles at a) inside the 2D island and b) outside the 2D island.

III. At final time (when $tc/\lambda \gg 100$)

From the final range in Figure 5.6, we can see that the charged particles released at radius as 0.1λ , 0.3λ and 0.5λ separate faster than the other radii. It seems the separation is related to the radius of releasing the charged particles. If the charged particles are released inside the center of Gaussian function, they separate from their initial field lines more than the other positions. In this range, the transition of the charged particles and their corresponding magnetic field lines are uncorrelated. Note that the corresponding length scale of the uncorrelation between particles and field lines is in the order of coherence length scale (λ) which, within this length scale, the slab field are still correlated. The charged particles are mainly influenced by slab turbulence and undergo subdiffusive as we can see from the slope = 0.5 in Figure 452. We normally find subdiffusive process when charged particles transport in pure slab magnetic field (Tooprakai et al., 2007).

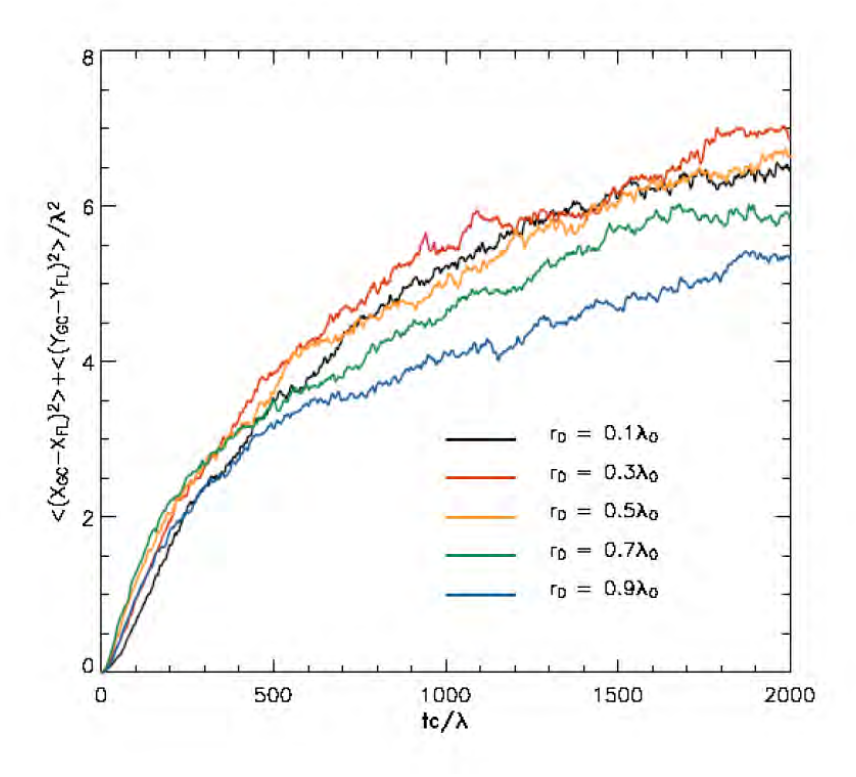


Figure 5.6 The mean squared perpendicular displacement and time in the final range.

From the results in this section, the separation of the charged particles are related with the distance from the center of the Gaussian flux tube (r_0) and where they experience the different structure of the magnetic field. When the charged particles are released at low curvature of the magnetic field line, the separation is more than the others at the initial times. In our results, we show that the separation at the beginning depend on the gradient and curvature drift due to the 2D field. Then, in intermediate time, they slowly drift to outside the 2D flux tube. The sharp gradient of 2D field can be distinct behavior of the particles inside and outside the island in this regime. It corresponds with the suppressed diffusive regime in the previous work (Chuychai et al., 2007; Tooprakai et al., 2007). In addition, for final time the separation of the charged particles is uncorrected with the starting point to release the charged particles. The separation of the charged particles depends on distance from the center of the Gaussian function and becomes subdiffusive, the charged particles are released at outside of 2D Gaussian field $(r_0 = 0.7\lambda)$ and 0.9λ , the separation is lower than the others radius. Finally, this work can help us to understand

more about the relation of the separation between guiding centers of charged particles and magnetic field lines. In the next section, we present the effect of separation in 2D+slab turbulence.

5.2 Separation of Charged Particles and their field lines in 2D+Slab tubuelence

Here we release the charged particles in 2D+slab turbulence inn various cases. We also trace the sample of charged particles and their magnetic field line which are started at the initial GC in pure slab and 2D+slab turbulence cases as shown in Figure 5.7

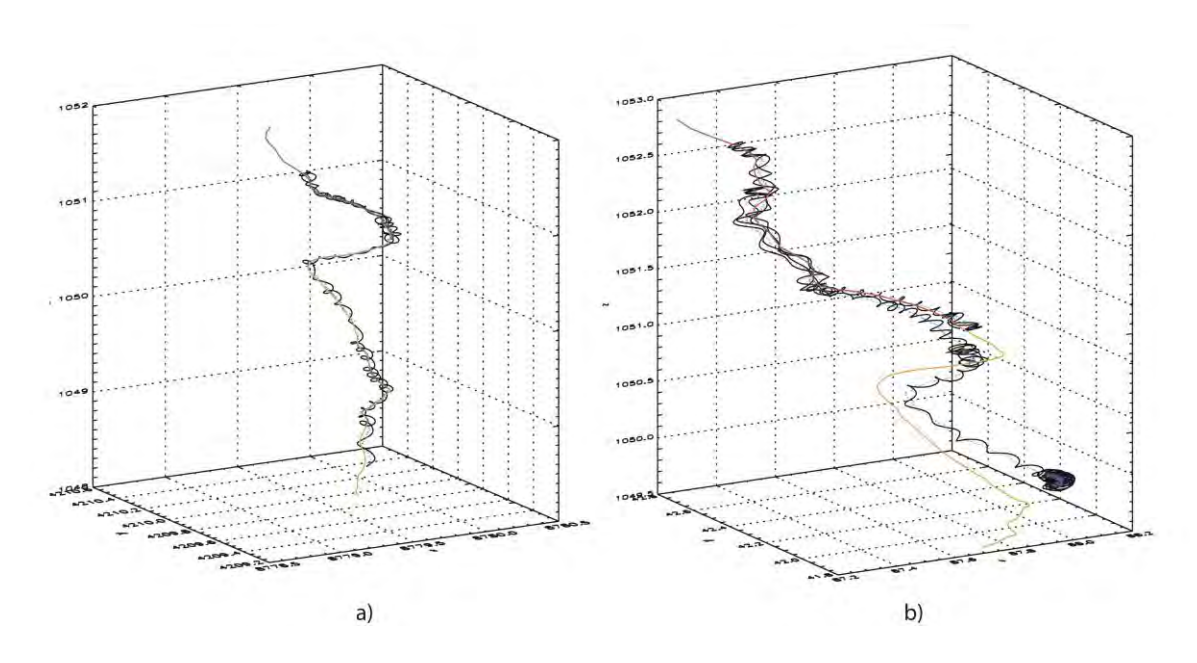


Figure 5.7 Examples of 20 MeV particle trajectories (BLACK lines), their guiding centers (BLUE dots), and their initial field lines (RED lines) in a) pure slab turbulence and b) 10% 2D+ 90% slab turbulence. Note that in our simulations the time scale is in units of λ/c and the length scale is in units of λ , where λ is the slab coherence scale and c is the speed of light.

We can see that the particle in pure slab case ties along the field lines while the particles from 2D+slab turbulence follow the field line at the beginning and then deviate from its field lines at the later time. Figure 5.8 shows the statistics when we release 1,000 particles and compute the mean squared of separation between particle's GCs and their field lines in both pure slab and 2D+slab turbulence. For the pure slab case, the results show that the particles in pure slab turbulence have very little

separation between particle trajectories and their field lines. The particles stick with their initial field lines. This is consistent with the theorem of Jokipii et al. (1993) and Jones et al. (1998). This effect happens when we reduce the dimensionality of the magnetic field. Despite from the particles in 2D+slab case, they diffuse along the time.

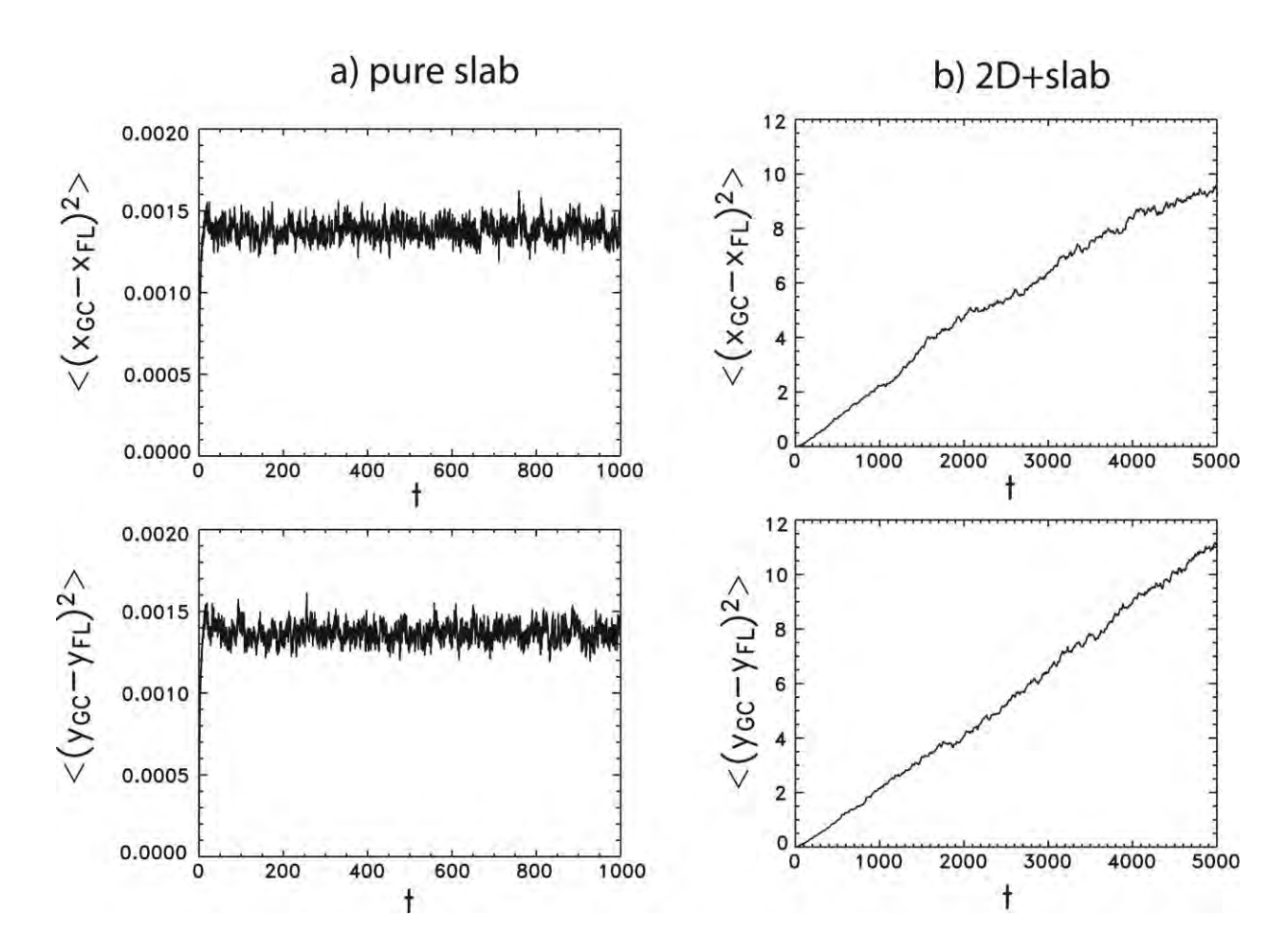


Figure 5.8 The results from the simulations of 100 MeV protons in a) pure slab and b) 2D+slab turbulence. The statistics in the plots show the spreading of particles from field lines as a function of time.

After that we perform the simulations for 1,000 charged particles in various cases to see the effect the many parameters to the separation such as particle energy, initial pitch angle, 2D fraction, and magnetic field strength.

Figure 5.9 shows how different particle energy responds to the separation. From the results we can see that low energy particles have lower separation than high energy particles. At intermediate time, very low energy particles stay or tie to the magnetic field before they leave the field lines as we can see the flat shape of the plot in Figure 5.9 for 10 keV and 1 MeV particles.

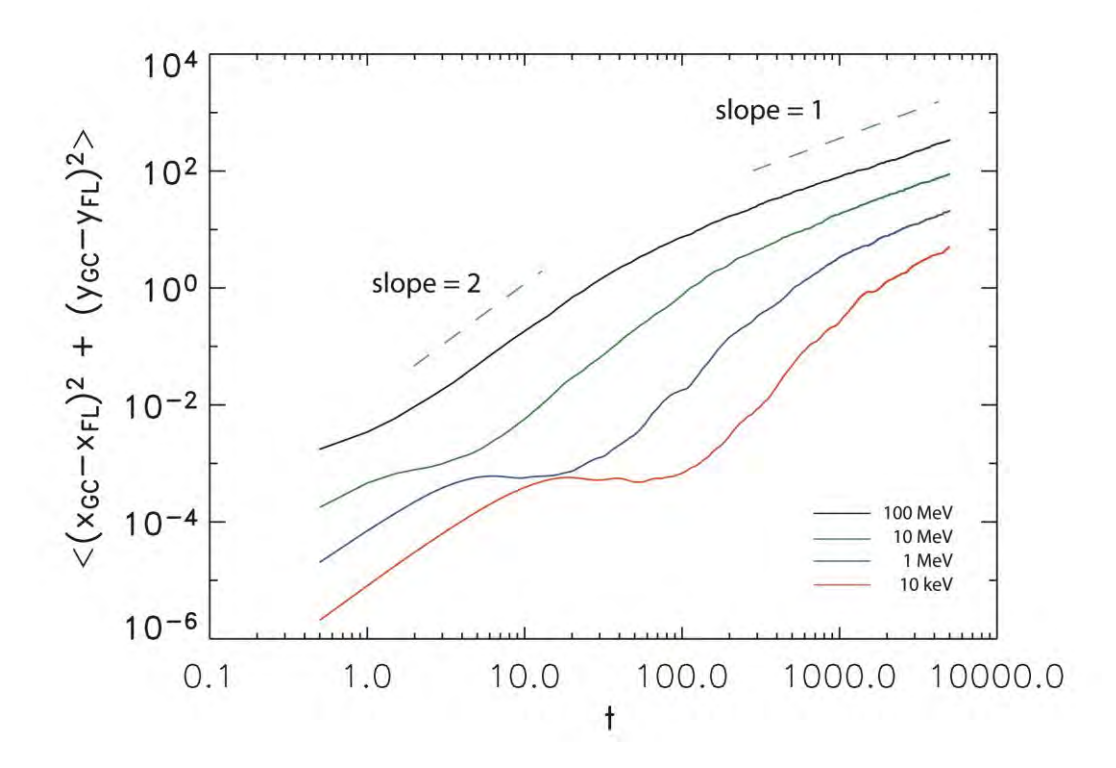


Figure 5.9 The results of the separation of charged particles and their corresponding field lines when we vary particle energy.

Next, we vary the initial pitch angle of the charged particles. The pitch angle is defined by the angle between velocity of particle and magnetic field. From the results in Figure 5.10, we found that the particles moving perpendicular to the magnetic field give more separation than the ones start in the direction parallel to the magnetic field. For long time limit, the separation reaches the same rate for all initial pitch angles.

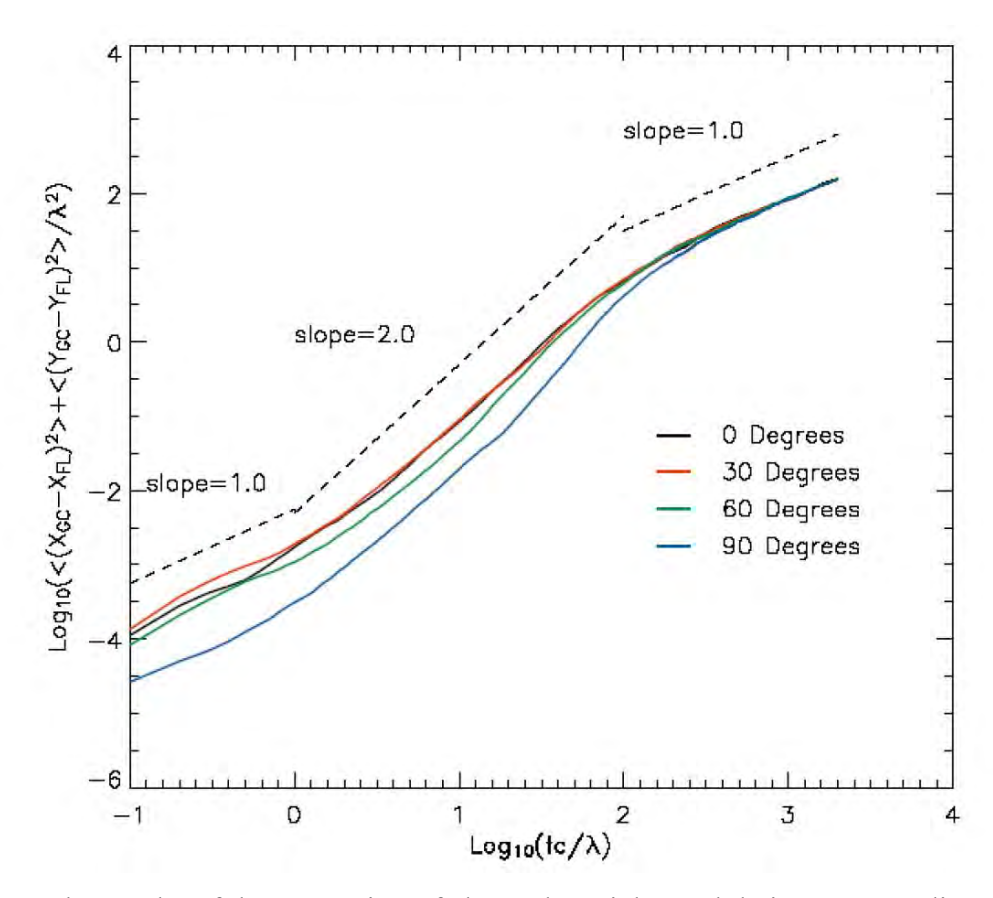


Figure 5.10 The results of the separation of charged particles and their corresponding field lines when we vary initial pitch angles.

We also vary 2D fraction to 10%, 20%, 50%, and 80%. We found that more 2D portion gives high separation as seen in Figure 5.11. Figure 5.12 presents the separation when the magnetic fluctuation is varied. We found that low magnetic fluctuation give less separation than the higher one. Similar to the other cases, the particles and the field lines are independent at long time as we can see from slope =1 of the graph.

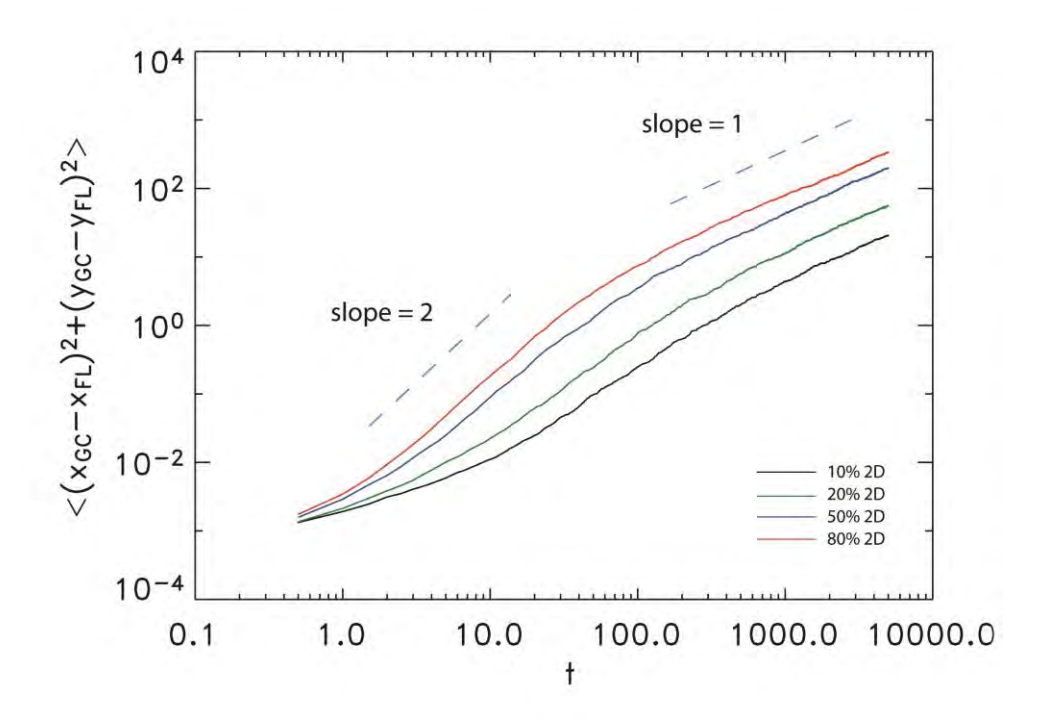


Figure 5.11 The results of the separation of charged particles and their corresponding field lines when we vary particle 2D fraction.

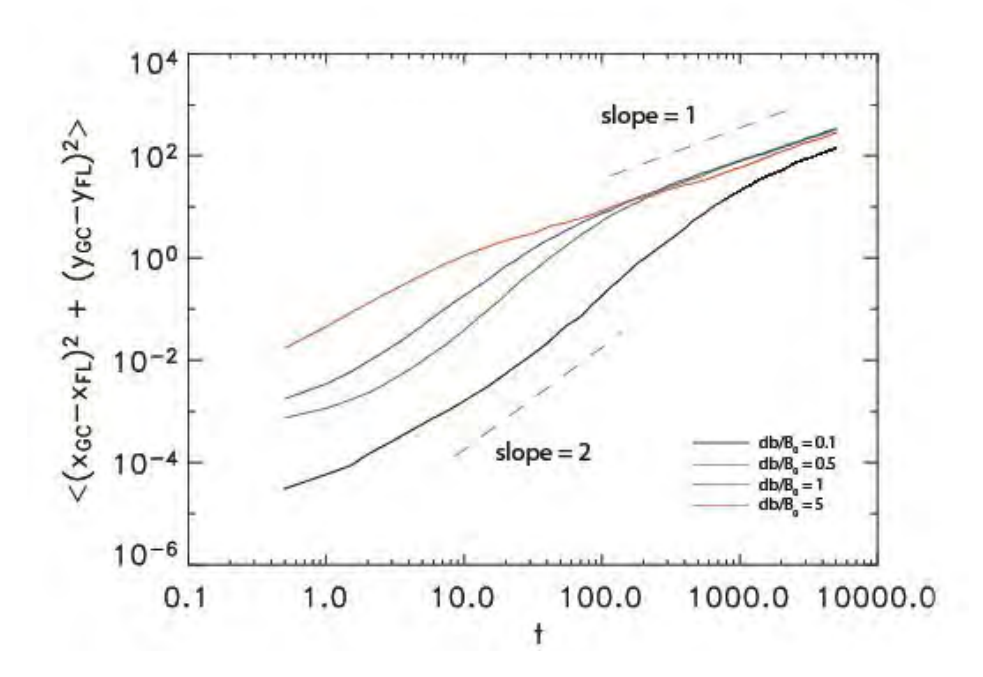


Figure 5.12 The results of the separation of charged particles and their corresponding field lines when we vary magnetic field strength.

For the long time limit, the separation between particles and field is diffusive as indicated by the slope of 1 at the end in all plots which can be explained by nonlinear guiding center theory (NLGC) (Matthaeus et al. 2003; Ruffolo et al. 2012). In this region the particles move independently from their initial field lines. At early times before strong separation, the simulations in most of the cases have a slope close to 2, related to a free streaming regime. The transition between free streaming separation and diffusive (independent) separation occurs at a displacement $\sim \lambda$. We find faster separation for an increasing 2D fraction, which is consistent with the lack of separation for pure slab turbulence, and also find faster separation for lower pitch angles.

Chapter 6

Technique for Measuring and Correcting the Taylor Microscale

This Chapter presents the new technique for measuring and correcting the Taylor microscale. After we generate time series as we discuss in subsection 3.1.3, we calculate the correlation function and the structure function. From parabolic fitting and extrapolation method, we obtain the estimated Taylor microscale. Next, we suggest to apply the correction ratio which depends on index q. Finally we apply with real spacecraft data.

6.1 Correlation Function and Structure Function

Focusing on the time domain, the Taylor microscale can be also view as the radius of curvature at the origin of the autocorrelation function.

$$R(\tau) = \langle F(t)F(t+\tau) \rangle. \tag{6.1}$$

For a small τ expansion and using $R(\tau) = R(-\tau)$, a requirement of time stationarity, the autocorrelation function near the origin, can be determined by

$$R(\tau) \approx 1 - \frac{\tau^2}{2\tau_{TS}^2} + \cdots \tag{6.2}$$

Therefore, one way to obtain the Taylor microscale from measurements is to fit $R(\tau)$ at the origin. However, sometimes the observation data do not have sufficient time resolution near the origin to perform an adequate parabolic fit.

In estimating the correlation function from many samples of data, it is useful to employ the normalized correlation function

$$\hat{R} = \frac{R}{\langle [F(t)]^2 \rangle}.$$
(6.3)

We can also express the data in the second order structure function S_2 , given by

$$S_2(\tau) = \langle [F(t+\tau) - F(t)]^2 \rangle. \tag{6.4}$$

In fact, the normalized correlation function and the second order structure functions are related by

$$\widehat{R}(\tau) = 1 - \frac{S_2(\tau)}{2\langle F(t)^2 \rangle}.$$
(6.5)

Figure 6.1 shows the structure functions for various dissipation range indices *q* that we generated as described in Sections 2.2 and 3.1.3. Several regimes are seen:

- For $\tau \gg \tau_d$, which is associated with the inertial range $(f^{-5/3})$ in Fourier space, one expects to find $S_2 \propto \tau^{2/3}$.
- For $\tau \ll \tau_d$ and with q = -5 and -4, one finds (see Figure 6.1) that $S_2 \propto \tau^2$. This is the regime, in accordance with equation (6.5), in which parabolic curvature of the correlation function is seen near $\tau = 0$.
- For $\tau \ll \tau_d$, but q values of -3 or shallower, the required parabolic behavior is not seen near τ_d , but rather this asymptotic behavior is deferred until $\tau < 1/f_e$. This is due to the fact that the spectrum for this range of q is not steep enough to cause convergence of the Taylor scale estimate. This convergence is now delayed until scales are sampled that are finer than the electron dissipation scale.

This change in behavior of Taylor scale estimates as the dissipation range spectral index is varied is actually very relevant to solar wind observations. For scales smaller than ion inertial length, the solar wind spectral slope is found to be quite variable. For example, Smith et al. (2006b) estimate that dissipation range magnetic spectral indices are broadly distributed with average values $|q| = 2.61 \pm 0.96$ for intervals lacking magnetic clouds, and $|q| = 2.01 \pm 0.84$ for cloud intervals.

A lesson can be learned from the above simple exercise: the asymptotic form of the correlation function embodied in equations (6.2) and (6.5) is not obtained until the sampled spectrum is k^{-4} or steeper. Between spectral indices -4 and -5, the transition to the asymptotic parabolic form migrates towards finer scales, until at k^{-3} , the transition is delayed until separations within the assumed inner cutoff scale are sampled.

From equation (6.5) we can compute the correlation function from the structure function. Figure 6.2 displays the correlation function for various q. From these plots, we can see that the correlation function has a parabolic shape at the origin. At this fixed resolution, the characteristic parabolic shape becomes better defined as the values of |q| are increased.

Suppose now we select a known q and we compute the radius of curvature of the correlation function from data over a range of small separations near the origin $0 < \tau \le \tau_{fit}$. While this value is intended to be small, to attempt to capture the parabolic regime (if present), the specific value τ_{fit} has no physical significance - it is just a maximum lag to be used in a fitting procedure. This choice of a range of data provides an estimate of τ_{TS} ; let us call it $\tau_{TS}^{est}(\tau_{fit})$.

At this point we have obtained an approximate fit, or representation, of the data in this range of τ , given by

$$\hat{R}(\tau) = 1 - \frac{\tau^2}{2\left[\tau_{TS}^{est}(\tau_{fit})\right]^2}.$$
(6.6)

This fit is inexact even if the measurements are perfect, because we expect that the Taylor scale is $\tau_{TS} = \lim_{\tau_{\text{fit}\to 0}} \tau_{\text{TS}}^{\text{est}}(\tau_{\text{fit}})$. It is not practical to compute this limit because the data has finite time resolution Δt , and because there may be limited data available at the shortest time lags. In another section below we will systematically examine the influence of Δt , the data sampling time.

What can be done however is to compute $\tau_{TS}^{est}(\tau_{fit})$ for a range of τ_{fit} , and to examine the trend of the corresponding values of τ_{TS}^{est} as the maximum lag used in the fit becomes smaller. Figure 6.3 illustrates sequences of such fits $\tau_{TS}^{est}(\tau_{fit})$ versus τ_{fit} . Each of these curves approaches the exact value of Taylor scale in the limit of zero τ_{fit} , as expected. This is for an idealized model times series that can be evaluated at any time separation we wish. Consequently, when a range of τ_{TS}^{est} is available, but only for a set of values of τ_{fit} that excludes the origin, one can try to recover a more precise value of τ_{TS} by an extrapolation technique that provides a refined estimate of the radius of curvature at the origin.

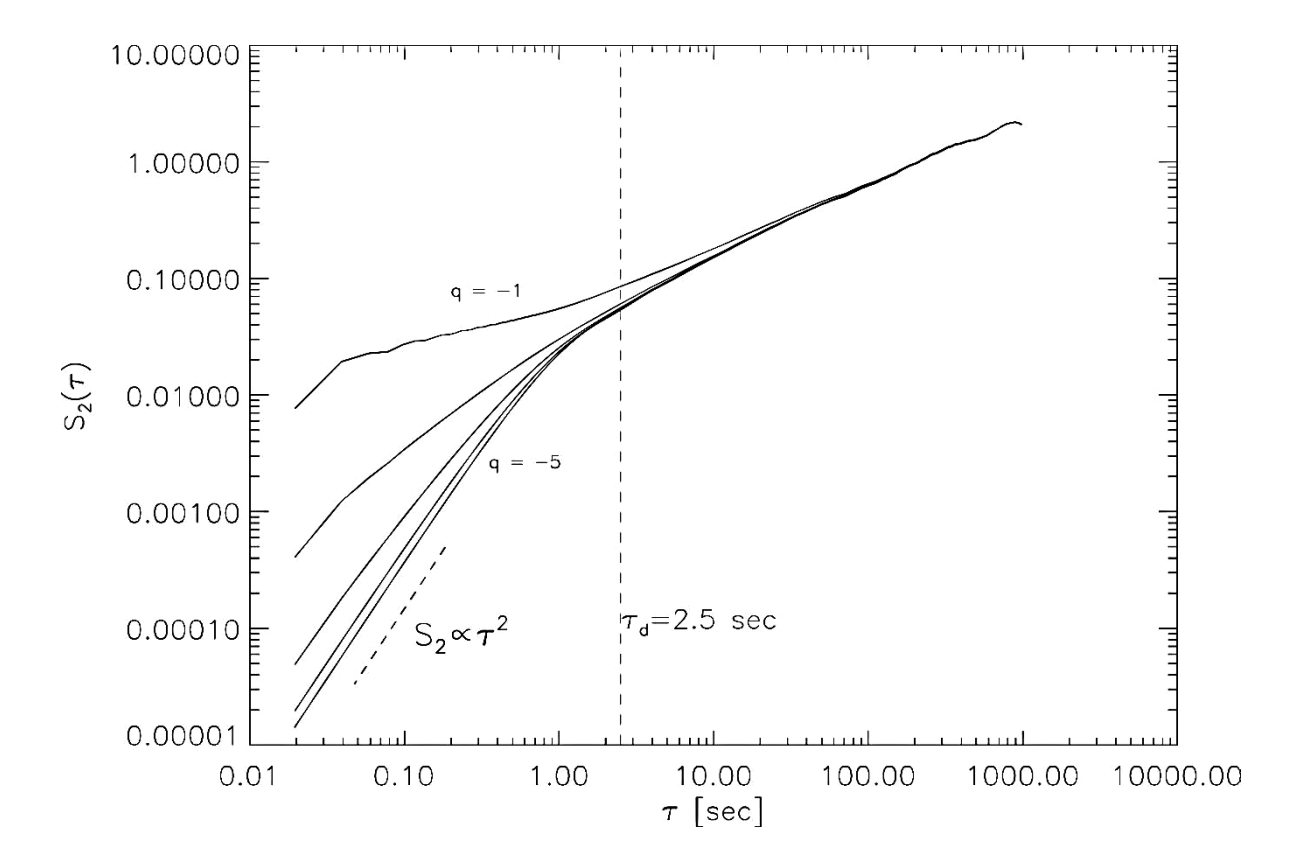


Figure 6.1 The structure function computed from the time series data for a number of values of q. The bottom curve is associated with a q value of -5 and the higher curves are determined with q = -4, -3, -2, and -1, respectively.

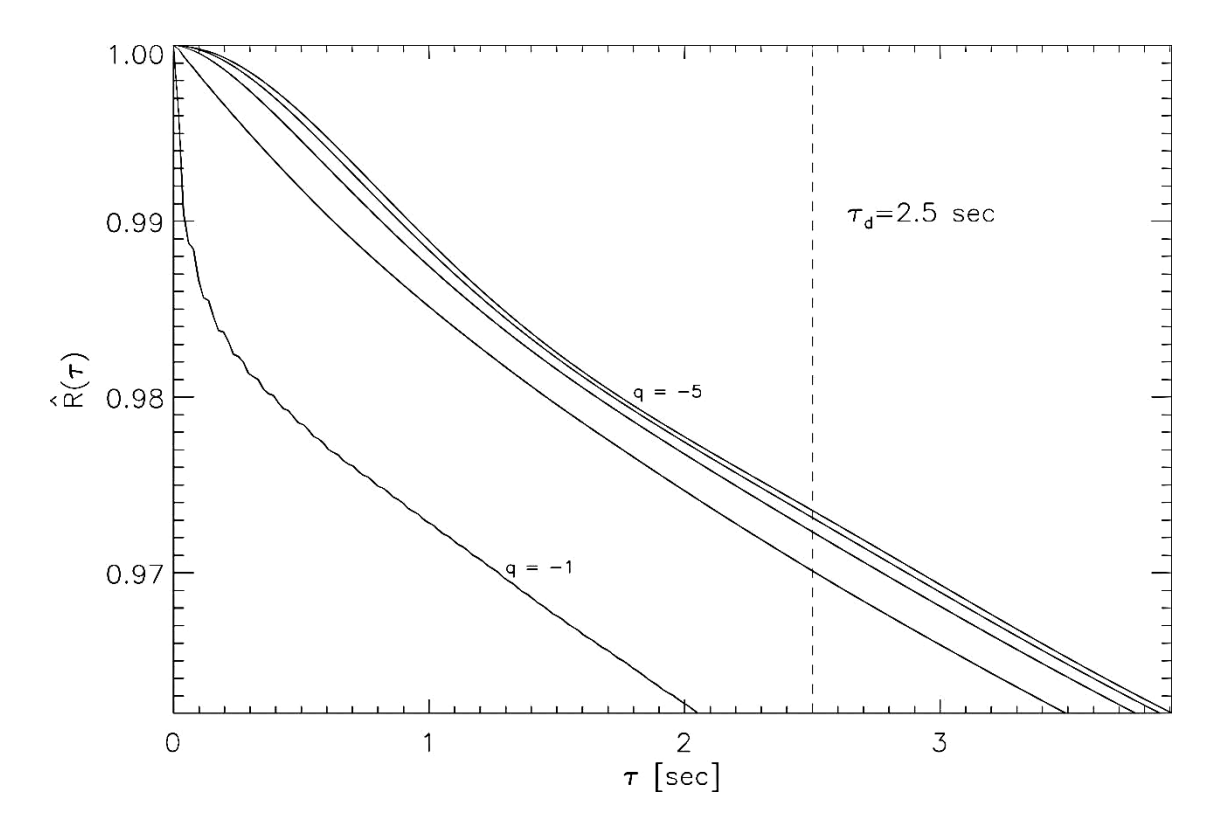


Figure 6.2 The correlation function near the origin. The top curve is determined from q = -5 and the next curves are calculated using q = -4, -3, -2, and -1, respectively.

6.2 Extrapolation Method

To obtain a stable value for the Taylor microscale at $\tau=0$, we apply an extrapolation method based on the Richardson extrapolation technique (see Dahlquist and Bjorck, 2003) in analogy with similar procedures employed in numerical analysis. In the first step we compute a series of parabolic fits to data near the origin, and for varying values of τ_{fit} , up to a largest values of τ_{fit} , say, τ_{max} . Using the available estimated values of Taylor microscale $\tau_{TS}^{est}(\tau_{max})$, for this range of τ_{max} , we can compute a straight-line extrapolation of the Taylor scale back to the origin ($\tau_{fit}=0$). This extrapolation gives a single estimate of a refined value of the Taylor microscale.

Still, it remains unclear which value of τ_{max} we should use. On the one hand; a larger τ_{max} permits the use of more data in the fit process, but a smaller τ_{max} moves us closer to the

asymptotic range in which the formula equation (6.6) for approximating the radius of curvature at the origin becomes more exact.

Therefore we will look for a stable range of values, as follows. Figure 6.4 illustrates the variation of the extrapolated values of Taylor microscale as the value of τ_{max} is varied. In the next step of the method we examine whether for some range of τ_{max} we find a stable value of estimated τ_{TS}^{est} . When working with real data with time cadence Δt , this process is constrained by the temporal resolution, i.e., $\tau_{fit} > \Delta t$. The distribution of number of available estimates at each lag τ can also become an issue. In addition, the quality of the refinement of the Taylor microscale value will depend on the steepness of the spectrum (i.e., q) at the high frequencies.

In the next section we will discuss more details regarding the effects of data resolution and q. For now, (see Figure 6.4) we can make some general statements regarding quality of estimation when a range of estimates is available for time lags near the dissipation (spectral steepening) scale. For large values of q, where the correlation function has a large radius of curvature at the origin (compared to τ_d), we find a value of the Taylor microscale as τ_{max} approaches zero. In contrast, for small values of |q|, we do not obtain a stable value of τ_{TS} after the extrapolation.

One can also see by examining Figure 6.4 how lower time resolution data can have an adverse effect. Larger Δt means that the data close to the origin become unavailable for the extrapolation near τ_{fit} =0. The best we might be able to do in such cases is to choose a stable value in the range of $\tau_{max} \sim \tau_d$. By trying this out with the graphs, we see that this approach yields an underestimate of the Taylor microscale value when q is approximately greater than 4 and an overestimate when |q| is approximately less than 4. Our results suggest that a good estimate of τ_{TS} is obtained by a linear extrapolation to zero lag using the slope of the curves τ_{fit}^{est} evaluated near $\tau_{max} = \tau_d$ (see Figure 6.3). In the next subsection we will discuss how we can further improve this estimate with a correction ratio that takes into account known information about the spectra at higher frequencies.

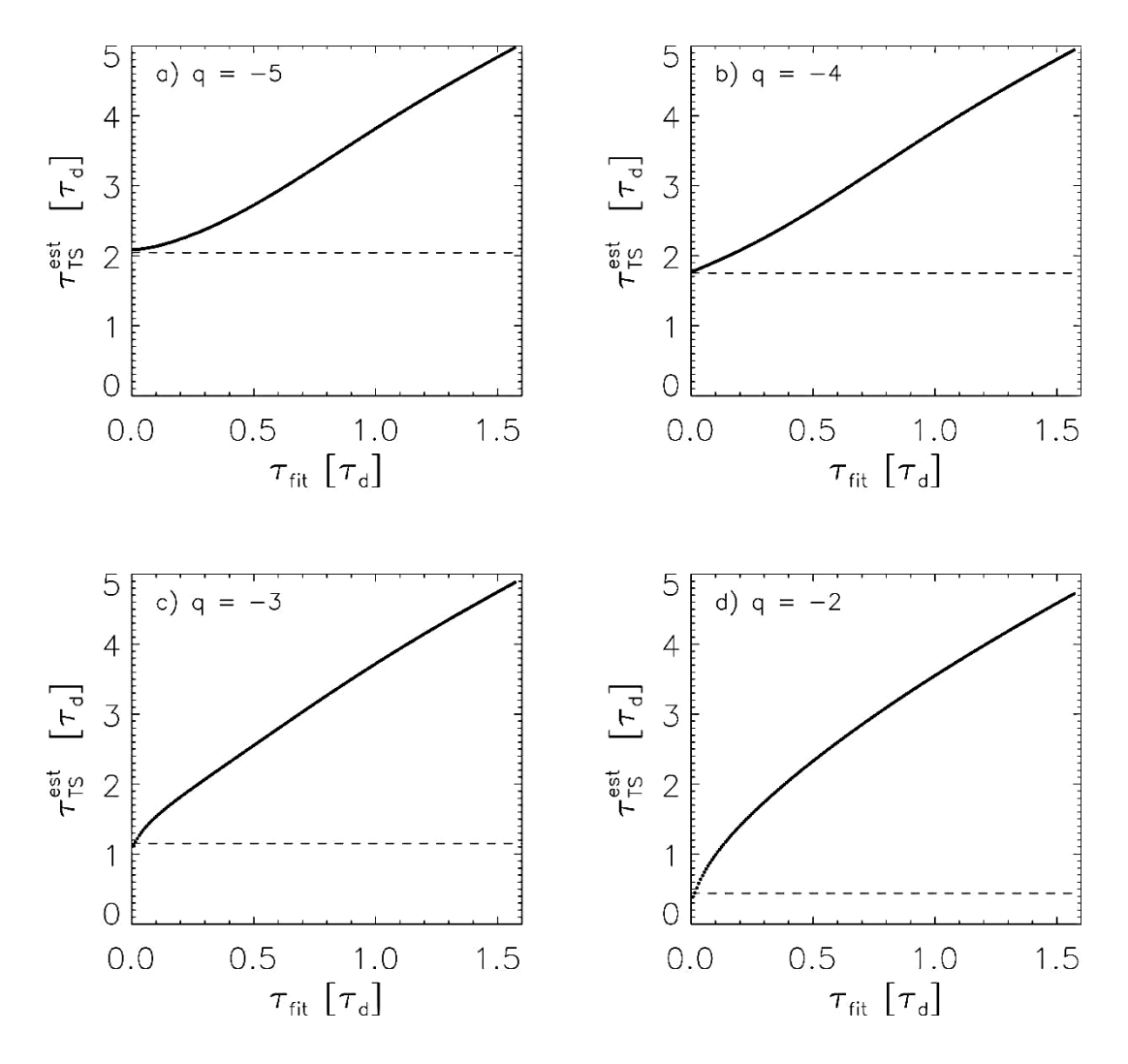


Figure 6.3 Taylor microscale from parabolic fit of the correlation function near the origin for each τ_{fit} for a number of q. Axes are in units of τ_{d} .

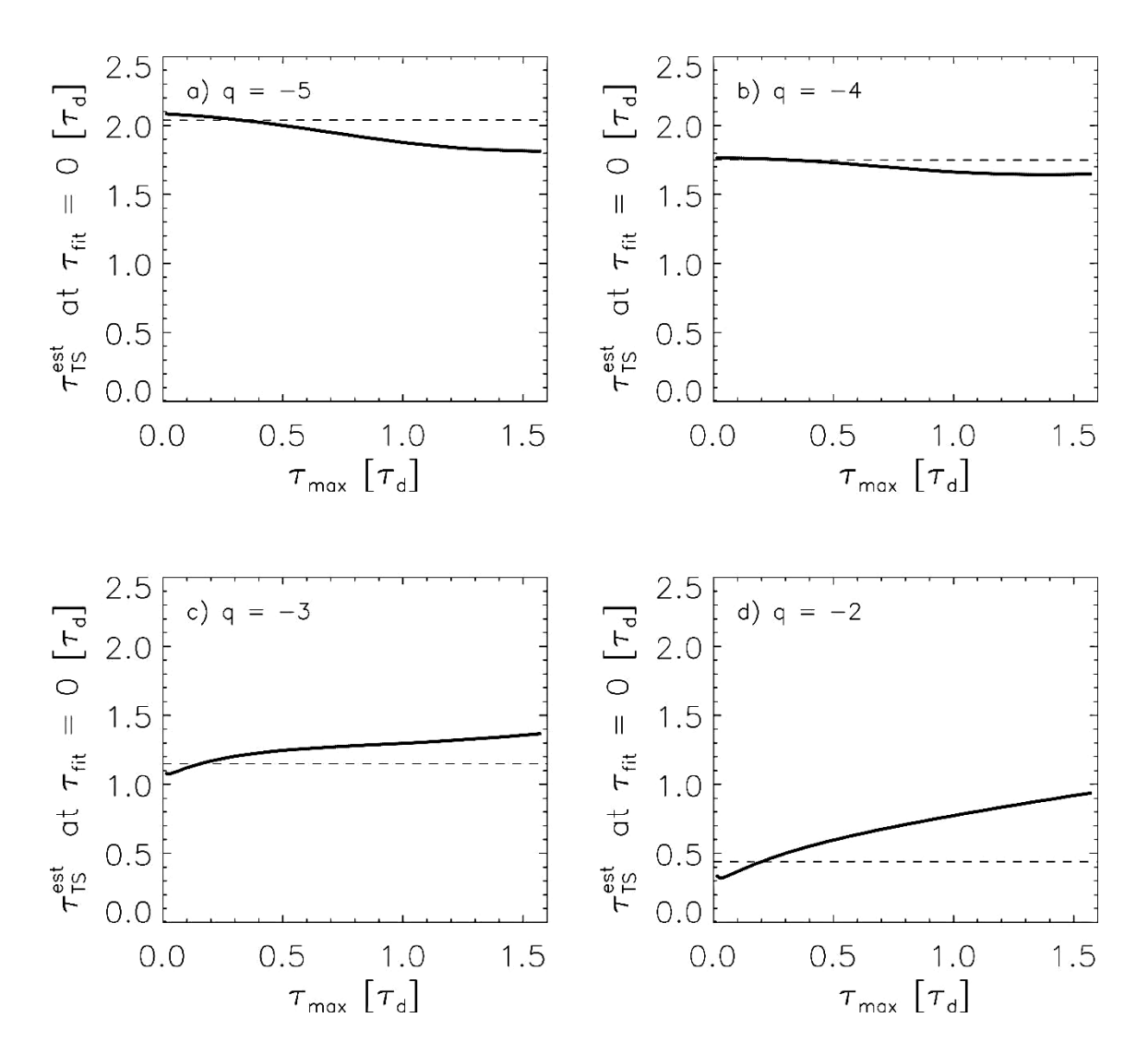


Figure 6.4 Values of τ_{TS} determined by linear extrapolation from the data in Figure 6.3 at the origin (i.e., the intercept). Plotted are the extrapolated Taylor microscale values determined from a range of τ_{max} .

6.3 Correction Ratio

The resolution of the observational data is limited by the instrumentation, the spacecraft data downlink and on board storage. The lower resolution of the data, the less accurate Taylor microscale value will be since it is harder to make measurments that are sensitive to the radius of curvature of the correlation function at the origin. In this section, we examine the effect of the temporal resolution of the data by artificially reducing the resolution of the synthetic time series, and again estimating the Taylor microscale with the same method. The new values for each resolution of the data can be compared with the expected Taylor microscale value to assess the impact of the temporal resolution. In particular, the ratio of these two, $(\tau_{TS}^{expect}/\tau_{TS})$ is of interest. We call this ratio a "correction factor" as it can be employed to estimate the actual Taylor scale given the value computed from finite time resolution data. However this correction must assume knowledge of the spectrum at unresolved frequencies. Here that amounts to knowledge of the value of q.

Figure 6.5 demonstrate the variation of the correction factor when we vary the temporal resolution Δt and the spectral index q. We can see that the correction ratio strongly depends on q. There are three regimes of behavior apparent in the Figure, which we approximate as a piecewise linear function. The model suggested for correction of Taylor scale estimates from finite time resolution data. Accordingly, the empirical correction factor r(|q|) can be written as

$$r(|q|) = \begin{cases} -0.64 \left(\frac{1}{|q|}\right) + 0.72, & \text{when } |q| < 2 \\ -2.61 \left(\frac{1}{|q|}\right) + 1.70, & \text{when } 2 \le |q| < 4.5 \\ -0.16 \left(\frac{1}{|q|}\right) + 1.16, & \text{when } |q| \ge 4.5. \end{cases}$$

$$(6.7)$$

With this model for a given data set and a known value of q it is possible to compute a corrected value of the Taylor microscale using

$$\tau_{TS} \approx r(|q|)\tau_{TS}^{extra} \tag{6.8}$$

where τ_{TS}^{extra} is an estimate obtained by the extrapolation method described in Section 6.2 above.

Clearly this procedure presupposes availability of data such that the estimates of Taylor scale are based on near asymptotic tendencies of the functions that are computed. From a practical perspective this appears to require that information about the functions near the dissipation scale τ_d be included in the analysis. Based on the present numerical experiments, we recommend therefore that the resolution of the data be at least as good as $\Delta t < 0.4\tau_d$.

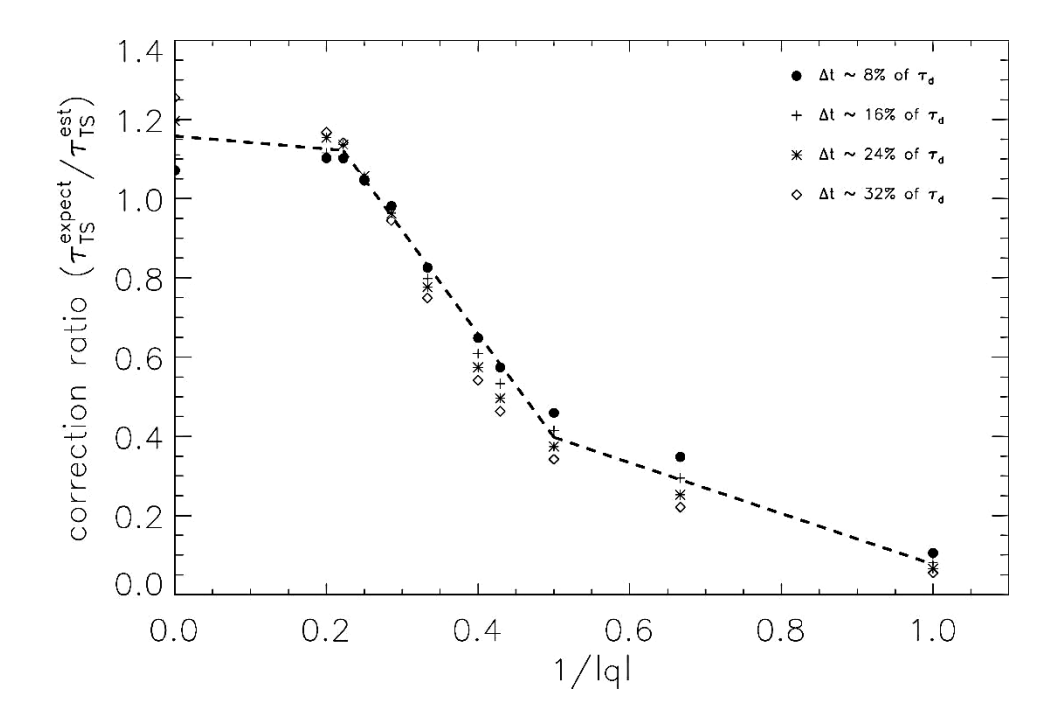


Figure 6.5 Correction ratio versus 1/|q| for number of different Δt values.

6.4 Applying the Technique to Spacecraft Data

From an analysis of the magnetic field data from the ACE spacecraft (Smith et al. 2006a), the Taylor microscales in the left column of Figure 6.6 are determined by employing the extrapolation method described above, but without applying the correction ratio. The time resolution of the ACE data used here is $\delta t = 0.333$ s. The black color shows the data from regions characterized as open magnetic field line regions, and the red color shows the data from magnetic clouds (closed field regions). The Taylor scales have already been converted to spatial scales by using frozen-in approximation.

The values obtained for dissipation range spectral index lie between -5 to -1 and the ratio of Taylor scale (λ_T) to the dissipation scale (λ_d) ranges between 0.1 and 10.

The individual plots show that the red and black points appear to be equally scattered. The right column of Figure 6.6 shows the values of λ_T , after the application of the correction ratio. After the corrections, we can see that the majority of the black points have $\lambda_T' > \lambda_d$ for q < -3 and the red points have $\lambda_T' < \lambda_d$ for q > -3. This indicates a hydrodynamics type of plasma for open magnetic field case and non-hydrodynamics in the magnetic cloud cases. Further discussion of this analysis is found in Matthaeus et al. (2008), where it is argued that the difference in the behavior of these cases points to a difference in relative importance of dissipative processes at ion and electron scales.

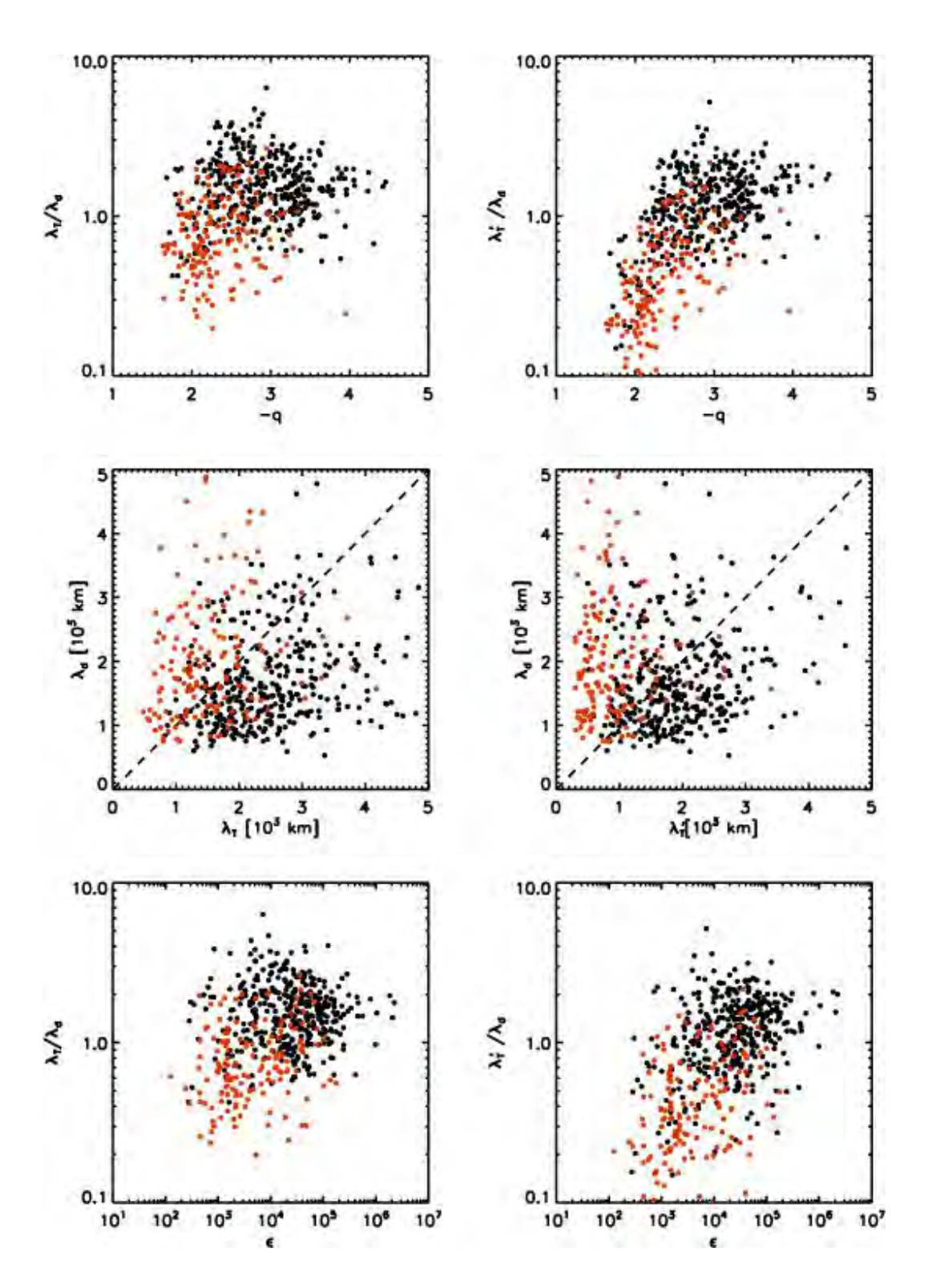


Figure 6.6 The left column shows the plots before applying the correlation ratio to the Taylor mocroscale λ_T and the right column shows the Taylor microscale (λ_T') after applying correlation ratio.

6.5 Conclusions

We have demonstrated a refined technique of calculating the Taylor microscale from a discrete times series by computing correlation functions from structure functions. The method that we employed is based on the definition of the Taylor microscale. To verify this technique we analyze a synthetic time series derived from a defined power density spectrum. We are able to reproduce the Taylor scale values with our technique after applying a correction term, which improves our estimate of the Taylor microscale, estimated from a Richardson extrapolation technique (see Weygand et al. 2009). In addition, we studied the effects of the dissipation range spectral index and the time resolution of the simulated data. Moreover, we show an example of the application of the technique to solar wind magnetic field data (Matthaeus et al. 2005, 2008). This technique is expected to be useful for extracting refined estimates of the Taylor microscale from experimental and observational turbulence data in solar wind and other astrophysical contexts.

References

- Alexandrova, O., J. Saur, C. Lacombe, A. Mangeney, J. MItchell, S. J. Schwartz, and P. Robert (2009), *Phys. Rev. Lett.* **103**, 165,003.
- Bieber, J. W., Matthaeus, W. H., Smith, C. W., Wanner, W., Kallenrode, M.-B., and Wibberenz, G. (1994), *Astrophys. J.* **420**, 294-306.
- Bieber, J. W., Wanner, W., and Matthaeus, W. H. (1996), J. Geophys. Res. 101, 2511-2522.
- Chuychai, P. (2004), Models of random magnetic fields and some implications for turbulence structure and particle transport in the heliosphere, Doctoral Dissertation, Chulalongkorn University, Bangkok.
- Chuychai, P., Ruffolo, D., Matthaeus, W. H. and Rowlands, G. (2005), *Astrophys. J.* **633**, L49-L52.
- Chuychai, P., Ruffolo, D., Matthaeus, W. H. & Meechai, J. (2007), *Astrophys. J.* **659**, 1761-1776.
- Chuychai, P., Weygand, J. M., Matthaeus, W. H., Dasso, S., Smith, C. W., and Kivelson, M. G. (2014), *J. Geophys. Res. Space Physics* **119**, doi:10.1002/2013JA019641.
- Dahlquist, G., and Bjorck, A. (2003), *Numerical Methods*, Courier Dover Publications, Mineola, New York, Prentice-Hall 1974.
- Dalena, S., Chuychai, P., Mace, R. L., Greco, A., Qin, G. & Matthaeus, W. H. (2012), *Computer Physics Comunications* **183**, 1974-1985.
- Dröge, W. (2000), Space Sci. Rev. 93, 121-151.
- Gary, S. P. and Borovsky, J. E. (2004), J. Geophys. Res. 109, 6105.
- Jokipii, J. R., Kóta, J., and Giacalone, J. (1993), Geophys. Res. Lett. 20, 1759.
- Jones, F. C., Jokipii, J. R., and Baring, M. G. (1998), Astrophys. J. 509, 238.

- Leamon, R. J., Matthaeus, W. H., and Smith, C. W. (1998), Astrophys. J. 507, L181.
- Matthaeus, W. H., and M. L. Goldstein (1982), J. Geophys. Res. 87, 10,347-10,354.
- Matthaeus, W. H., Goldstein, M. L., and Roberts, D. A. (1990), J. Geophys. Res. 95, 20673.
- Matthaeus, W. H., Qin, G., Bieber, J. W., and Zank, G. (2003), Astrophys. J. 590, L53.
- Matthaeus, W. H., Weygand, J. M., Chuychai, P., Dasso, S., Smith, C. W., and Kivelson, M. (2008), *Astrophys. J.* **678**, L141.
- Matthaeus, W. H., Dasso, S., Weygand, J. M., Milano, L. J., Smith, C. W., and Kivelson, M. G. (2005), *Phys. Rev. Lett.* **95**, 231,101.
- Press, W. H., Teukolsky, S. A., Vetterling, W. T. & Flannery, B. P. (1992), *Numerical recipes in FORTRAN: The art of scientific computing*, Cambridge: Cambridge University Press.
- Ruffolo, D., Chuychai, P., Wongpan, P., Minnie, J., Bieber, J. W., and Matthaeus, W. H., *Astrophys. J.* **686**, 1231
- Ruffolo, D., Pianpanit, T., Matthaeus, W. H., and Chuychai, P. (2012), *Astrophys. J. Lett.* **747**, L34.
- Sahraoui, F., Goldstein, M. L., Robert, P., and Khotyaintsev, Y. V. (2009), *Phys. Rev. Lett.* 102, 231,102.
- Smith, C. W., K. Hamilton, J. Vasquez, and R. J. Leamon (2006a), Astrophys. J. 645, L85.
- Smith, C. W., B. J. Vasquez, and K. Hamilton (2006b), J. Geophys. Res. 111, A09111.
- Tooprakai, P., Chuychai, P., Minnie, J., Ruffolo, D., Bieber, J.W. & Matthaeus, W.H. (2007), *Geophys. Res. Lett.* **34**, L17015.
- Weygand, J. M., Matthaeus, W. H., Dasso, S., Kivelson, M. G., and Walker, R. J. (2007), *J. Geophys. Res.* **112**, A10201.
- Weygand, J. M., Matthaeus, W. H., Dasso, S., Kivelson, M. G., Kristler, L. M., and Mouikis, C. (2009), *J. Geophys. Res.* **114**, A07213.

- Weygand, J. M., Matthaeus, W. H., El-Alaoui, M., Dasso, S., and Kivelson, M. G. (2010), *J. Geophys. Res.* **115**, A12250.
- Weygand, J. M., Matthaeus, W. H., Dasso, S., and Kivelson, M. G. (2011), *J. Geophys. Res.* **116**, A08102.
- Wikee, C. (2013), *The Effect of The Pitch Angles of Charged Particles on their Separation From Magnetic Field Lines*, Master's Thesis. Mae Fah Luang University, Chiang Rai.

Output

โครงการผลกระทบเนื่องจากสนามแม่เหล็กปั่นป่วนในตัวกลางระหว่างดาวเคราะห์ต่อการเคลื่อนที่ของ อนุภาคพลังงานสูงจากดวงอาทิตย์

(MRG5280239)

1. ผลงานตีพิมพ์ในวารสารวิชาการนานาชาติ

- 1.1. Chuychai, P., Weygand, J. M., Matthaeus, W. H., Dasso, S., Smith, C. W., and Kivelson, M. G. (2014), Technique for measuring and correcting the Taylor microscale, *Journal of Geophysical Research: Space Physics* 119, doi:10.1002/2013JA019641. [Impact factor: 5.602] (เอกสาร แนบหมายเลข 1)
- 1.2 Ruffolo, D., Pianpanit, T., Matthaeus, W. H., and Chuychai, P. (2012), Random Ballistic Interpretation of Nonlinear Guiding Center Theory, Astrophysical Journal Letters 747, L34. [Impact factor: 3.44](เอกสารแนบหมายเลข 2)

2. การนำผลงานวิจัยไปใช้ประโยชน์

เชิงวิชาการ

เนื่องจากงานวิจัยนี้เน้นทางด้านความรู้พื้นฐานทางด้านฟิสิกส์ดาราศาสตร์ จึงยังไม่มีการนำไปใช้ ประโยชน์เชิงพาณิชย์ เชิงนโยบาย และเชิงสาธารณะ อย่างไรก็ตามในเชิงวิชาการงานวิจัยนี้มีส่วนในการผลิต มหาบัณฑิตที่มีความเชี่ยวชาญเฉพาะทางด้านวิทยาศาสตร์เชิงคำนวณ เป็นจำนวน 1 คน คือนายชาติ วิคี ใน หัวข้อ "The Effect of The Pitch Angles of Charged Particles on their Separation From Magnetic Field Lines" ซึ่งเป็นงานวิจัยที่ต่อยอดจากงานวิจัยในโครงการนี้ และยังสามารถสร้างองค์ความรู้ ใหม่ที่เกี่ยวข้องกับสารกลุ่มนี้

3. อื่น ๆ

การเสนอผลงานในที่ประชุมวิชาการระดับนานาชาติ

- Chuychai, P., Ruffolo, D., and Matthaeus, W. H., "Separation of Charged Particles from Magnetic Field Lines in Two-Component Magnetic Turbulence", American Geophysical Union (AGU) Fall Meeting 2010, San Francisco, California, 13-17 December 2010. (poster presentation)
- Chuychai, P., Ruffolo, D., Wikee, C., Seripienlert, A., Matthaeus, W. H., "Separation of Charged Particles from Their Turbulent Magnetic Field Lines at Early Times", AOGS AGU (WPGM) Joint Assembly, 13 17 August, 2012, Resorts World Convention Centre, Singapore. (poster presentation)
- David Ruffolo, Theerasarn Pianpanit, William Matthaeus, Piyanate Chuychai, "Random Ballistic Interpretation of Nonlinear Guiding Center Theory", AOGS AGU (WPGM) Joint Assembly, 13 17 August, 2012, Resorts World Convention Centre, Singapore. (oral presentation)
- Wikee, C., Chuychai, P., Ruffolo, D., and Matthaeus, W. H., "The effect of the initial pitch angles of charged particles to the separation on the turbulent magnetic field lines", Proceedings of the 16th International Annual Symposium on Computational Science and Engineering (ANSCSE 16) 175-180, 23 25 May 2012, Chiang Mai University, Chiang Mai, Thailand. (oral presentation)

การเสนอผลงานในที่ประชุมวิชาการระดับชาติ

• Chuychai, P., Ruffolo, D., Wikee, C., and Matthaeus, W. H., "Effect of Reduced Dimensionality of the Magnetic Field Fluctuations on the Cross-Field Motion of Charged Particles", The 6th Annual Conference of the Thai Physics Society, Siam Physics Congress 2011, March 23-26, 2011, Ambassdor City Jomtien Hotel, Pattaya, Thailand. (oral presentation)

Appendix

เอกสารแนบหมายเลข 1





Journal of Geophysical Research: Space Physics

TECHNIQUE

10.1002/2013JA019641

Key Points:

- Taylor microscale is important in turbulence
- Measurement is hindered by finite time resolution data
- Technique given here improves estimates

Correspondence to:

W. H. Matthaeus, whm@udel.edu

Citation:

Chuychai, P., J. M. Weygand, W. H. Matthaeus, S. Dasso, C. W. Smith, and M. G. Kivelson (2014), Technique for measuring and correcting the Taylor microscale, *J. Geophys. Res. Space Physics*, *119*, doi:10.1002/2013JA019641.

Received 21 NOV 2013 Accepted 4 MAY 2014 Accepted article online 8 MAY 2014

Technique for measuring and correcting the Taylor microscale

P. Chuychai^{1,2}, J. M. Weygand³, W. H. Matthaeus⁴, S. Dasso⁵, C. W. Smith⁶, and M. G. Kivelson³

¹School of Science, Mae Fah Luang University, Chiang Rai, Thailand, ²Thailand Center of Excellence in Physics, CHE, Ministry of Education, Bangkok, Thailand, ³Institute for Geophysics and Planetary Physics, University of California, Los Angeles, California, USA, ⁴Bartol Research Institute, Department of Physics and Astronomy, University of Delaware, Newark, Delaware, USA, ⁵Instituto de Astronomia y Fisica del Espacio (CONICET-UBA) and Departmento de Fisica (FCEN-UBA), Buenos Aires, Argentina, ⁶Space Science Center, University of New Hampshire, Durham, New Hampshire, USA

Abstract We discuss and develop methods to estimate and refine measurements of the Taylor microscale from discrete data sets. To study how well a method works, we construct a time series of discrete data with a known power spectrum and Taylor scale, but with various truncations of the resolution that eliminate higher frequencies in a controlled fashion. We compute the second-order structure function and correlation function, assuming that the unresolved dissipation range spectrum has various values of spectral index. A series of Taylor scale estimates are obtained from parabolic fits to subsets of the correlation function data, and these are extrapolated to the limit of zero separation. The error in this procedure, for finite time resolution sampling, depends on the spectral index in the dissipation range. When the spectral form is known, we can compute a correction factor that improves the estimate of the Taylor microscale value determined from the extrapolation method and band-limited data. Application of this technique to spacecraft observations of solar wind fluctuations is illustrated.

1. Introduction

The motivation of this study comes from recent efforts to measure the Taylor microscale in solar wind turbulence calculated using multispacecraft techniques [Matthaeus et al., 2005; Weygand et al., 2007, 2009, 2010, 2011; Gurgiolo et al., 2013]. The Taylor scale is related to the second derivatives of the data [Batchelor, 1970] (also see below); therefore, it is inherently sensitive to the high-frequency spectral content of the signal. Of course, for idealized time-continuous infinite precision data, the Taylor scale may be computed. Likewise, when very high cadence measurements are available [e.g., Alexandrova et al., 2009; Sahraoui et al., 2009], and the spectrum is steep enough (see below), it may be possible to unambiguously determine the Taylor scale. However, for available data sets with finite time cadence, the values of the Taylor scale obtained by a straightforward evaluation may be sensitive to the data resolution, as the correct value may depend on the physical signal above the sampling Nyquist frequency.

The objective of this study is to understand the accuracy of the Taylor scale estimates using finite resolution data sets, in which the high-frequency spectra may or may not be well known. We develop a method to improve these estimates based on the spectrum of the unresolved data, which can be used when estimates of the high-frequency spectrum of the signal are available in some way, whether it be observations, theory, or an informed guess. Although the main purpose here is to discuss measurement issues, the physical significance of the Taylor scale will be reviewed briefly in section 2.

In a system such as the solar wind, the Taylor microscale can be estimated from single spacecraft analyses. Within the context of the Taylor [1938] frozen-in flow approximation, time t separation is converted to spatial x separation using the relation $x = V_{sw} \times t$. In the latter case, instead of working in the spatial domain, the curvature of the two time correlation near the origin can be estimated. Frozen-in flow is a standard approximation in solar wind observational analysis and in wind tunnels. Dasso et al. [2008] demonstrates the validity of this approximation in the solar wind by comparing values determined from single spacecraft and multispacecraft analysis. With this background in mind, one can define the Taylor microscale (λ_T) by

$$\frac{1}{\lambda_{T}} = \sqrt{\frac{\langle \left(\frac{\partial F}{\partial x}\right)^{2}\rangle}{\langle F^{2}\rangle}} \to \frac{1}{V_{\text{sw}}\tau_{\text{TS}}} = \frac{1}{V_{\text{sw}}} \sqrt{\frac{\langle \left(\frac{\partial F}{\partial t}\right)^{2}\rangle}{\langle F^{2}\rangle}},\tag{1}$$



where F is the function of interest such as the velocity or magnetic field fluctuations. For generality and simplicity, here we will discuss methods for arriving at improved estimates of the Taylor scale under the assumption that the problem of interest is in the time domain or that frozen-in flow is valid. Therefore, the discussion will center on the procedure to extract τ_{TS} from a time series F(t). We will employ a model spectrum in which the inertial range terminates by steepening at a "dissipation scale" (Kolmogorov scale) or its equivalent in the time domain τ_d , which is the equivalent sweeping time of the dissipation length scale past the detector. Thus, in the present paper the term dissipation scale implies only the scale at which the power law cascade range terminates, generally leading to a steeper spectrum. This familiar terminology is used in a purely kinematic sense, without regard for whether this steepening is due to dissipation, dispersion, or some other effect.

Focusing on the time domain, the Taylor microscale can be also viewed as the radius of curvature at the origin of the autocorrelation function

$$R(\tau) = \langle F(t)F(t+\tau) \rangle. \tag{2}$$

From a small τ expansion, and using $R(\tau) = R(-\tau)$, a requirement of time stationarity, the autocorrelation function near the origin, can be determined by

$$R(\tau) \approx 1 - \frac{\tau^2}{2\tau_{TS}^2} + \dots$$
 (3)

Therefore, one way to obtain the Taylor microscale from measurements is to fit $R(\tau)$ at the origin. However, sometimes the observation data do not have sufficient time resolution near the origin to perform an adequate parabolic fit. This is due to the fact that for many reasonable spectra, the quadratic behavior suggested in equation (3) is not apparent until the correlation function is sampled at scales $\tau < \tau_d$. We will study the expected effects on Taylor scale determination using a designed function F(t) that is intentionally undersampled but which is extracted from a signal that has better time resolution and a known spectral index in the dissipation range. This is a useful approach to develop a procedure that reliably determines the Taylor microscale. To develop this technique we construct the time data series based on a specified spectrum. With varying resolution synthetic data, we obtain empirical values of the Taylor microscale and compare with the known "exact" values. We find that it is possible to define a multiplicative correction factor that allows us in some circumstances to adjust and improve the measured Taylor scale based on assumptions about the spectrum of the unresolved high-cadence data.

Before turning to the main content of the paper, we digress briefly concerning the physical significance of the Taylor scale, both in hydrodynamics [Batchelor, 1970] and in the case of collisionless plasma such as the solar wind. In isotropic hydrodynamic turbulence, the Taylor scale may be defined as the radius of curvature at the origin of the two-point velocity (v) correlation $R(r) = \langle \mathbf{v}(0) \cdot \mathbf{v}(\mathbf{r}) \rangle$; that is, $\lambda_T^2 = R(0)/R''(0)$ or equally well as the length associated with the mean square curl of the velocity (the vorticity), $\lambda_T^2 = \frac{\langle |\mathbf{v}|^2 \rangle}{\langle |\nabla \times \mathbf{v}|^2 \rangle}$. For viscous (ν) dissipation in an incompressible medium, the Taylor scale is also related to dissipation, in that (for suitable boundary conditions), $\frac{d(|\mathbf{v}|^2)}{dt} = -v\lambda_T^{-2}\langle |\mathbf{v}|^2 \rangle$. In this sense the Taylor scale is the "equivalent dissipation scale," in that, any instant of time, the dissipation rate is the same as if all the energy were at the Taylor scale. In older turbulence texts [Hinze, 1975] the Taylor scale is sometimes designated simply as "the dissipation scale." However, in more current terminology the latter is usually reserved for the Kolmogorov scale η which signifies the scale (or wave number $1/\eta$) at which the power law inertial range terminates and beyond which lies the dissipation range. For high Reynolds number R and correlation scale L, in hydrodynamics, the Taylor scale is $\lambda_T = L/\sqrt{R}$, while $\eta = L/R^{3/4}$. Therefore, $\lambda_T/\eta = R^{1/4}$, and the two become well separated at very large R. For plasmas the dynamical status of both the Taylor scale and the Kolmogorov scale becomes ambiguous [see, e.g., Matthaeus et al., 2008]. The mechanism of dissipation is not well understood for collisionless plasma and may vary in different parameter regimes. Thus, λ_T cannot be interpreted as connected with the length scale or rate of energy dissipation. Likewise, the termination of the inertial range may not be associated with dissipation, as the onset of kinetic dispersive waves may also be influential. Nevertheless, it is convenient to maintain the kinematic definitions of Taylor scale and "dissipation scale," related respectively to the second derivative of the correlation function at the origin and the termination of the inertial range. In the remainder of the paper we adopt the kinematic meaning of λ_T and the dissipation scale, as well as their time domain counterparts, to be defined below.



2. Generating Discrete Data With a Known Taylor Scale

To develop our method, we use synthetic data generated using a known spectrum and then employ a typical methodology to evaluate the Taylor microscale. The spectrum is constructed with inertial and dissipation ranges that have been independently controlled and have generally different power law indices. To be specific, we let the inertial range have a spectral index of -5/3, while the dissipation range has an adjustable spectral index q. The particular functional form of the spectrum is

$$P(f) = \begin{cases} \frac{c}{\left[1 + (f\tau_0)^2\right]^{5/6}}, & \text{where } f_{\min} < f \le f_d \end{cases}$$

$$\frac{c}{\left[1 + (f_d\tau_0)^2\right]^{5/6}} \left(\frac{f_d}{f}\right)^q, & \text{where } f_d < f \le f_e \end{cases}$$

$$0, & \text{where } f_e < f \le f_{\max},$$

$$(4)$$

where q<0. The reasons for these choices are as follows: First, the flat spectral region at very low frequencies $f\tau_0<<$ 1 is designed to make the signal time stationary. This is unrealistic for the solar wind, which has very low frequency components due to, e.g., solar rotation and solar cycle [see, e.g., Matthaeus and Goldstein, 1982]. However, we are not concerned with very low frequency effects here. Second, the inertial range with Kolmogorov spectral index of $\sim 5/3$ is found for higher frequencies, at $f\tau_0>1$. Third, there is a discontinuous jump at the top of the inertial range at frequency f_d , the slope steepening from -5/3 to -|q|, in qualitative accord with observations [Leamon et al., 1998; Hamilton et al., 2008; Alexandrova et al., 2009; Sahraoui et al., 2009]. Finally, at high frequencies $f>f_e$ we set the spectrum to zero, for numerical rather than physical reasons, to provide a very smooth trigonometric interpolation of the signal at the grid scale.

Adopting illustrative values that are representative of the solar wind at 1 AU, we assume that the spectrum starts from $f_{\rm min}=1.22\times10^{-5}$ Hz and is flat until $f_0=1/ au_0=3.906\times10^{-4}$ Hz, a "bendover" frequency often associated with the correlation scale or coherence time. Thereafter, the spectrum has an inertial range with a 5/3 power law index, until a second breakpoint is encountered at $f_d = 1/\tau_d = 0.4$ Hz. For historical reasons, this breakpoint, which terminates the power law MHD-scale inertial range, is often referred to as the dissipation scale [Leamon et al., 1998], although it is also possible that it characterizes dispersion in addition to dissipation [Gary and Borovsky, 2004]. In the hydrodynamic case the eddy turnover time and viscous dissipation time scales become equal at the dissipation scale. However, for the solar wind or other low-collisionality astrophysical plasmas, it is unclear whether the fluctuations become critically damped at the breakpoint/dissipation scale. For example, the inertial range is typically found to terminate near the proton gyroscales, and while some dissipation may occur at such scales, further kinetic plasma dynamics may transfer energy to higher frequencies until much smaller electron scales are encountered [Alexandrova et al., 2009; Sahraoui et al., 2009]. It has been argued that a substantial fraction of actual dissipation may occur due to electrons. In any case the scale f_d corresponds to the onset of kinetic processes and the end of the Kolmogorov-like inertial range. It is, however, the kinematic properties of the spectrum that come into play in the current study, rather than the dynamical origin of the spectral forms.

In our model beyond the breakpoint f_d , we extend the dissipation range with power law index q until $f_e=16.0$ Hz. This may be considered in the solar wind application to be associated with the electron dissipation scale. The spectrum cuts off completely at $f_{\rm max}=25.6$ Hz. To decide upon these numerical values, here we assume that the dissipation scale and electron dissipation scale correspond to the proton and electron inertial scales, respectively. Thus, we set $f_e/f_d=40$ to be consistent with the ratio of electron and proton inertial scales in MHD, which is about $\sqrt{m_p/m_e}=42.9$ [see, e.g., *Sahraoui et al.*, 2009].

Once we have specified the spectrum, we generate realizations of the signal in the frequency domain, F(f), as

$$F(f) = \sqrt{P(f)} \exp[i\phi] \tag{5}$$

where ϕ is a random phase. Then a fast Fourier transform is used to convert the function F(f) into the real-time domain. In the simulations reported here, we employ this approach to obtain 2^{22} data points for the time series.

Table 1. Showing Index q Which We Vary for Each Case and Their Taylor Scales When We Fix the Dissipation Scale $(\tau_d) = 2.5 \text{ s}$

case	$ au_{ extsf{TS}}^{ ext{expect}} ext{ [s]}$	$ au_{\mathrm{TS}}^{\mathrm{expect}} \left[au_d ight]$
$q = -\infty$	6.569	2.63
q = -5	5.097	2.04
q = -4	4.368	1.75
q = -3	2.869	1.15
q = -7/3	1.607	0.64
q = -2	1.095	0.44
q = -1	0.095	0.028

We next compute the Taylor microscale from the data set we generated by employing the definition equation (1). In Table 1, we give the Taylor microscale values for a range of dissipation scale indices q corresponding to the generic power spectrum shown in Figure 1. (Note that the spectra are given here as Fourier amplitudes squared, which can easily be converted to power spectral density.) We will treat these expected values of the Taylor microscale as the true or exact Taylor microscale values for the synthetic time series data. To examine and test our extrapolation method, we use only one eighth of the original data. The purpose of defining this subset is that any consistent method will provide good (and even convergent) values of $\tau_{\rm TS}$ when the time resolution Δt of the estimates is very fine, i.e., the spectral cutoff is resolved

and $\Delta t f_{\text{max}} < 1/2$. However, our motivation is to obtain reasonably accurate values of τ_{TS} when the effective resolution of the data sampling is adjusted so that we are not in this asymptotic regime—a circumstance that is more likely to be realized in practice when analyzing spacecraft data.

With the subset of our discrete time series, we compute the second-order structure function. This can be used to obtain an estimate of the correlation function. We then determine the radius of curvature from correlation function and an estimate of the Taylor microscale. In the following section, we will demonstrate an extrapolation technique [*Weygand et al.*, 2007, 2009, 2010, 2011] to estimate Taylor microscale from a series of parabolic fits of the correlation function near the origin. The details of the method we use are given in the following subsections.

2.1. Correlation Function and Structure Function

In estimating the correlation function from many samples of data, it is useful to employ the normalized correlation function

$$\hat{R} = \frac{R}{\langle [F(t)]^2 \rangle}.$$
(6)

This reduces errors associated with variability of the variance, i.e., the fluctuation energy. Almost the same information is contained in the second-order structure function S_{2} , given by

$$S_2(\tau) = \langle [F(t+\tau) - F(t)]^2 \rangle. \tag{7}$$

In fact,

$$\hat{R}(\tau) = 1 - \frac{S_2(\tau)}{2\langle F(t)^2 \rangle}.$$
 (8)

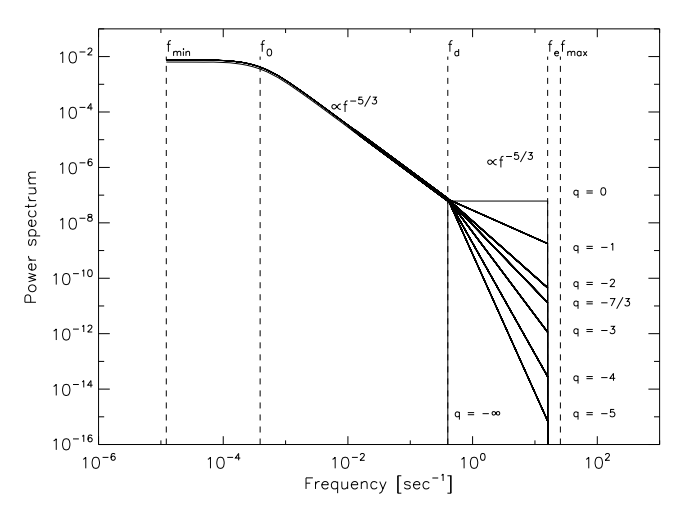


Figure 1. The power spectrum for a number of values of q in the dissipation range.

Figure 2 shows the structure functions for various dissipation range indices q that we generated as described in section 2. Note that values of dissipation range spectral index in the range -5/3 < q < -1 are pathological in that the implied "dissipation range" has either the same or shallower spectral power law than that found in the inertial range. These values are included only for illustration. As q is varied, several regimes are seen:

- 1. For $\tau \gg \tau_d$, which is associated with the inertial range $(f^{-5/3})$ in Fourier space, one expects to find $S_2 \propto \tau^{2/3}$.
- 2. For $\tau \ll \tau_d$ and with q = -5 and -4, one finds (see Figure 2) that $S_2 \propto \tau^2$.

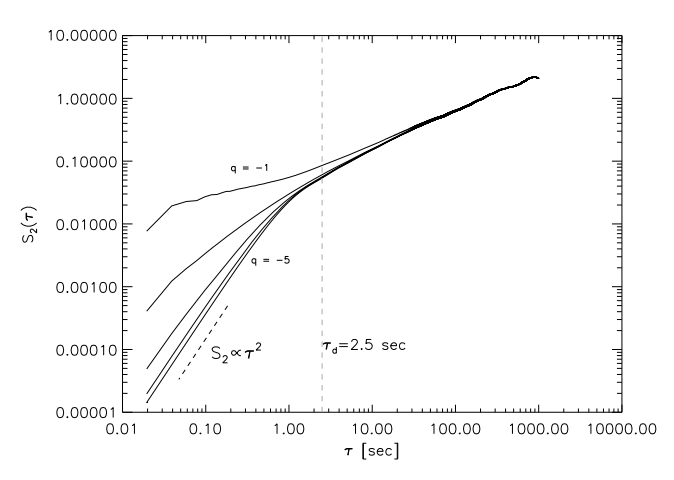


Figure 2. The structure function computed from the time series data for a number of values of q. The bottom curve is associated with a q value of -5, and the higher curves are determined with q = -4, -3, -2, and -1, respectively.

- This is the regime, in accordance with equation (8), in which parabolic curvature of the correlation function is seen near $\tau = 0$.
- 3. For $\tau \ll \tau_{d'}$, but q values of -3 or shallower, the required parabolic behavior is not seen near $\tau_{d'}$, but rather this asymptotic behavior is deferred until $\tau < 1/f_e$. This is due to the fact that the spectrum for this range of q is not steep enough to cause convergence of the Taylor scale estimate. This convergence is now delayed until scales are sampled that are finer than the electron dissipation scale.

This change in behavior of Taylor scale estimates as the dissipation range spectral index is varied and is actually very

relevant to solar wind observations. For scales smaller than ion inertial length, the solar wind spectral slope is found to be quite variable. For example, *Smith et al.* [2006b] estimate that dissipation range magnetic spectral indices are broadly distributed with average values $|q| = 2.61 \pm 0.96$ for intervals lacking magnetic clouds, and $|q| = 2.01 \pm 0.84$ for cloud intervals.

A lesson can be learned from the above simple exercise: the asymptotic form of the correlation function embodied in equations (3) and (8) is not obtained until the sampled spectrum is k^{-4} or steeper. Between spectral indices -4 and -3, the transition to the asymptotic parabolic form migrates toward finer scales, until at k^{-3} , the transition is delayed until separations within the assumed inner cutoff scale are sampled.

From equation (8), we can compute the correlation function from the structure function. Figure 3 displays the correlation function for various q. From these plots, we can see that the correlation function has a parabolic shape at the origin. At this fixed resolution, the characteristic parabolic shape becomes better defined as the values of |q| are increased.

Suppose now we select a known q and we compute the radius of curvature of the correlation function from data over a range of small separations near the origin $0 < \tau \le \tau_{\rm fit}$. While this value is intended to be small, to attempt to capture the parabolic regime (if present), the specific value $\tau_{\rm fit}$ has

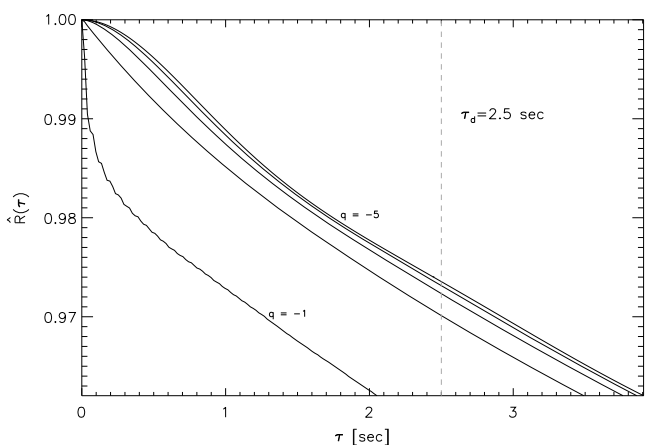


Figure 3. The correlation function near the origin. The top curve is determined from q=-5 and the next curves are calculated using q=-4,-3,-2, and -1, respectively.

no physical significance—it is just a maximum lag to be used in a fitting procedure. This choice of a range of data provides an estimate of τ_{TS} ; let us call it $\tau_{TS}^{est}(\tau_{fit})$. At this point we have obtained an approximate fit, or representation, of the data in this range of τ , given by

$$\hat{R}(\tau) = 1 - \frac{\tau^2}{2 \left[\tau_{TS}^{\text{est}}(\tau_{\text{fit}}) \right]^2}.$$
 (9)

This fit is inexact even if the measurements are perfect, because we expect that the Taylor scale is $\tau_{\rm TS}=\lim_{\tau_{\rm fit}\to 0} \tau_{\rm TS}^{\rm est}(\tau_{\rm fit})$. It is not practical to compute this limit because the data has finite time resolution Δt and because there may be limited data available at the shortest time lags. In another section below we will systematically examine the influence of Δt , the data sampling time.



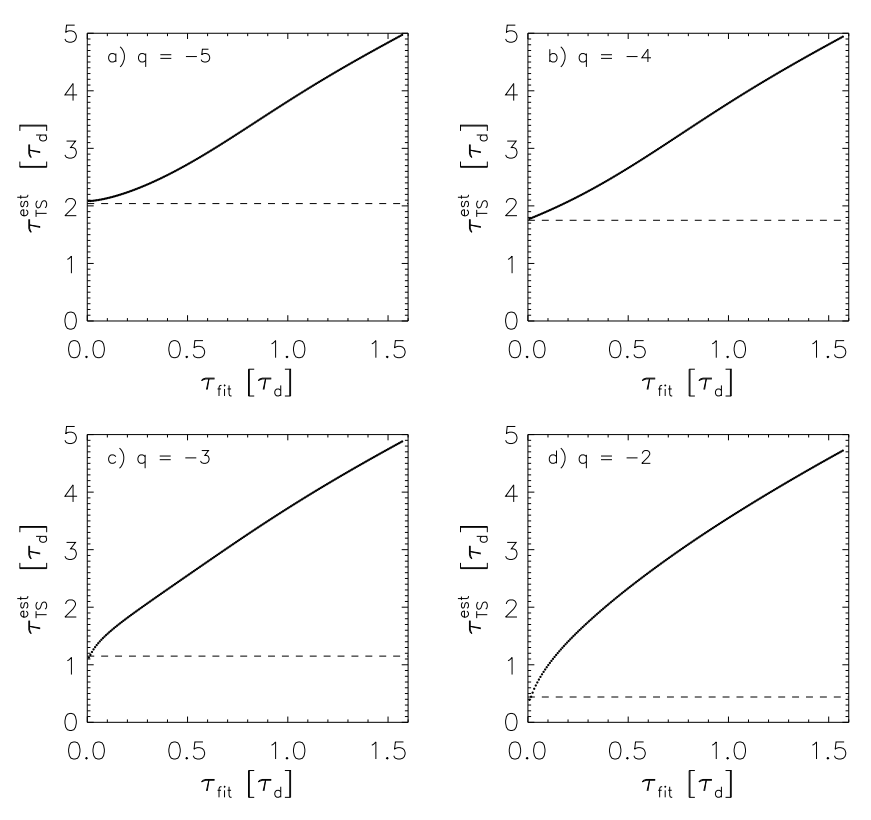


Figure 4. Taylor microscale from parabolic fit of the correlation function near the origin for each $\tau_{\rm fit}$ for a number values of q. Axes are in units of τ_d . Dashed line indicates the exact Taylor microscale.

What can be done, however, is to compute $au_{TS}^{\text{est}}(au_{\text{fit}})$ for a range of au_{fit} and to examine the trend of the corresponding values of au_{TS}^{est} as the maximum lag used in the fit becomes smaller. Figure 4 illustrates sequences of such fits $au_{TS}^{\text{est}}(au_{\text{fit}})$ versus au_{fit} . Each of these curves approaches the exact value of Taylor scale in the limit of zero au_{fit} , as expected. This is for an idealized model times series that can be evaluated at any time separation we wish. Consequently, when a range of au_{TS}^{est} is available, but only for a set of values of au_{fit} that excludes the origin, one can try to recover a more precise value of au_{TS} by an extrapolation technique that provides a refined estimate of the radius of curvature at the origin.

2.2. Extrapolation Method

To obtain a stable value for the Taylor microscale at $\tau=0$, we apply a method based on the Richardson extrapolation technique [see *Dahlquist and Bjorck*, 2003] in analogy with similar procedures employed in numerical analysis. In the first step we compute a series of parabolic fits to data near the origin, and for varying values of $\tau_{\rm fit}$, up to a largest values of $\tau_{\rm fit}$, say, $\tau_{\rm max}$. Using the available estimated values of Taylor microscale $\tau_{\rm TS}^{\rm est}(\tau_{\rm max})$ for this range of $\tau_{\rm max}$, we can compute a straight line extrapolation of the Taylor scale back to the origin ($\tau_{\rm fit}=0$). This extrapolation gives a single estimate of a refined value of the Taylor microscale.

Still, it remains unclear which value of τ_{max} we should use. On the one hand, a larger τ_{max} permits the use of more data in the fit process, but a smaller τ_{max} moves us closer to the asymptotic range in which the formula equation (9) for approximating the radius of curvature at the origin becomes more exact. Therefore, we will look for a stable range of values, as follows.

Figure 5 illustrates the variation of the extrapolated values of Taylor microscale as the value of $\tau_{\rm max}$ is varied. In the next step of the method we examine whether for some range of $\tau_{\rm max}$ we find a stable value of estimated $\tau_{\rm TS}^{\rm est}$. When working with real data with time cadence Δt , this process is constrained by the temporal resolution, i.e., $\tau_{\rm fit} > \Delta t$. The distribution of number of available estimates at each lag τ can also become an issue. In addition, the quality of the refinement of the Taylor microscale value will depend on the steepness of the spectrum (i.e., q) at the high frequencies.

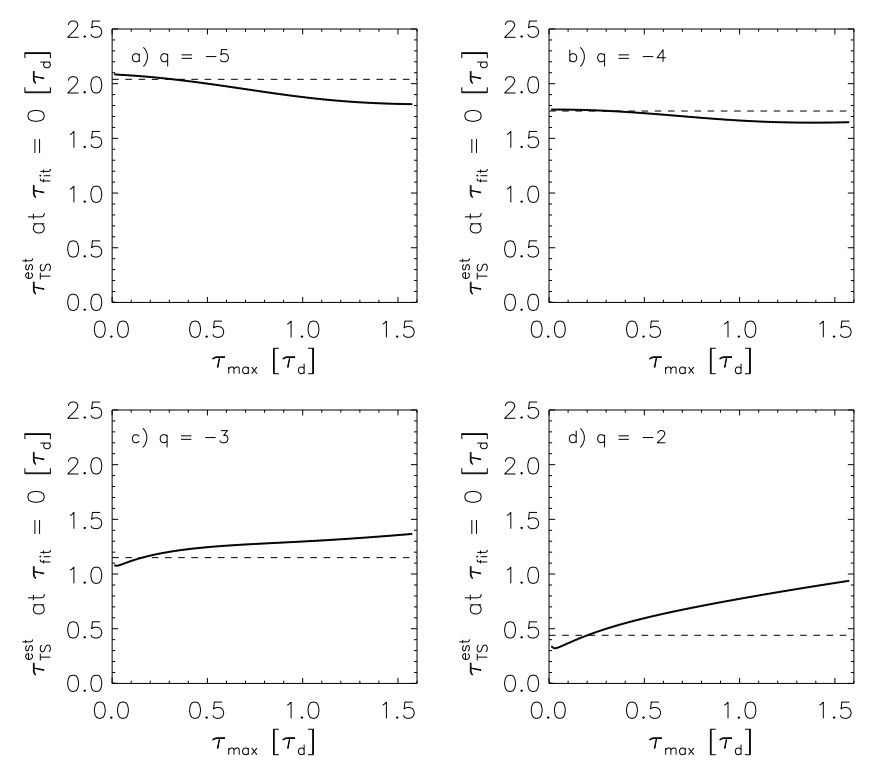


Figure 5. Values of τ_{TS} determined by linear extrapolation from the data in Figure 4 at the origin (i.e., the intercept). Plotted are the extrapolated Taylor microscale values determined from a range of τ_{max} .

In the next section we will discuss more details regarding the effects of data resolution and q. For now, (see Figure 5) we can make some general statements regarding quality of estimation when a range of estimates is available for time lags near the dissipation (spectral steepening) scale. For large values of |q|, where the correlation function has a large radius of curvature at the origin (compared to τ_d), we find a stable value of the Taylor microscale as $\tau_{\rm max}$ approaches zero. In contrast, for small values of |q|, we do not obtain a stable value of $\tau_{\rm TS}$ after the extrapolation.

One can also see by examining Figure 5 how lower time resolution data can have an adverse effect. Larger Δt means that the data close to the origin become unavailable for the extrapolation near $\tau_{\rm fit}=0$. The best we might be able to do in such cases is to choose a stable value in the range of $\tau_{\rm max}$ to τ_d . By trying this out with the graphs, we see that this approach yields an underestimate of the Taylor microscale value when |q| is approximately greater than 4 and an overestimate when |q| is approximately less than 4. Our results suggest that a good estimate of $\tau_{\rm TS}$ is obtained by a linear extrapolation to zero lag using the slope of the curves $\tau^{\rm est}(\tau_{\rm fit})$ evaluated near $\tau_{\rm max}=\tau_d$ (see Figure 4). In the next subsection we will discuss how we can further improve this estimate with a correction ratio that takes into account known information about the spectra at higher frequencies.

2.3. Correction Ratio

The resolution of the observational data is limited by the instrumentation, the spacecraft data downlink, and spacecraft data storage. The lower resolution of the data is the less accurate the Taylor microscale value will be, since the measurements become less sensitive to the radius of curvature of the correlation function at the origin. In this section, we examine the effect of the temporal resolution of the data by artificially reducing the resolution of the synthetic time series and again estimating the Taylor microscale with the same method. The new values for each resolution of the data can be compared with the expected Taylor microscale value to assess the impact of the temporal resolution. In particular, the ratio $\tau_{\rm TS}^{\rm expect}/\tau_{\rm TS}^{\rm est}$ is of interest. We call this ratio a "correction factor" as it can be employed to estimate the actual Taylor scale given the value computed from finite time resolution data. However, this correction must assume knowledge of the spectrum at unresolved frequencies. Here that amounts to knowledge of the value of q.

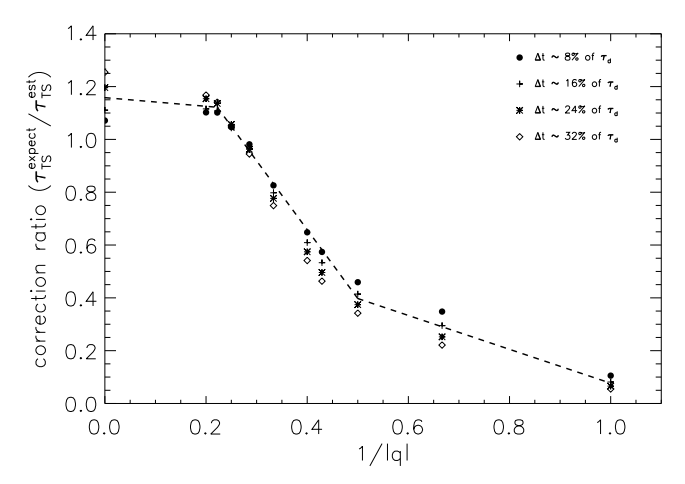


Figure 6 demonstrates the variation of the correction factor when we vary the temporal resolution Δt and the spectral index |q|. We can see that the correction ratio strongly depends on |q|. There are three regimes of behavior apparent in the figure, which we approximate as a piecewise linear function. The model suggests a correction for the Taylor scale estimates obtained from finite time resolution data. Accordingly, the empirical correction factor r(|q|) can be written as

Figure 6. Correction ratio versus 1/q for number of different Δt values.

$$r(|q|) = \begin{cases} -0.64 \left(\frac{1}{|q|}\right) + 0.72, & \text{when } |q| < 2 \\ -2.61 \left(\frac{1}{|q|}\right) + 1.70, & \text{when } 2 \le |q| < 4.5 \\ -0.16 \left(\frac{1}{|q|}\right) + 1.16, & \text{when } |q| \ge 4.5. \end{cases}$$
 (10)

With this model for a given data set and a known value of q, it is possible to compute a corrected value of the Taylor microscale using

$$\tau_{\mathsf{TS}} \approx r(|q|)\tau_{\mathsf{TS}}^{\mathsf{extra}}$$
 (11)

where $au_{\text{TS}}^{\text{extra}}$ is an estimate obtained by the extrapolation method described in section 2.2 above. This procedure presupposes that sufficient data are available to approximately determine the asymptotic tendencies of the correlations. From a practical perspective this appears to require that information about the functions near the dissipation scale au_d be included in the analysis. Based on the present numerical experiments, we recommend therefore that the resolution of the data be at least as good as $\Delta t < 0.4 au_d$.

3. Applying the Technique to Spacecraft Data

From an analysis of the magnetic field data from the ACE spacecraft [Smith et al., 2006a], the Taylor microscales in the left column of Figure 7 are determined by employing the extrapolation method described above but without applying the correction ratio. We use the same data set of ACE observations as was employed by Smith et al. [2006a, 2006b] and Hamilton et al. [2008]. The time resolution of the ACE data used here is $\delta t = 0.333$ s or three vectors per second. The analysis of the ACE proceeds in the following way: The second-order structure function matrix is computed for each interval in the set of intervals studied. The Taylor scale is then estimated using a series of maximum lag approximations from a maximum lag of four data points to a maximum lag of 25. A line is fit to these estimated values of the Taylor scale as a function of maximum lag, and the lag = 0 intercept is computed. This gives the final estimated values shown in the figure. The dissipation scale is computed from the power spectrum as the intercept between two fit lines, one describing the ion inertial range frequencies and the other describing the ion dissipation range frequencies. The dissipation range spectral index q is determined from the short wavelength fit.

The black color shows the data from regions characterized as open magnetic field line regions, and the red color shows the data from magnetic clouds (closed field regions). The Taylor scales have already been converted to spatial scales by using the frozen-in approximation.

The values obtained for dissipation range spectral index lie between -5 and -1, and the ratio of Taylor scale (λ_T) to the dissipation scale (λ_d) ranges between 0.1 and 10. The individual plots show that the red and black

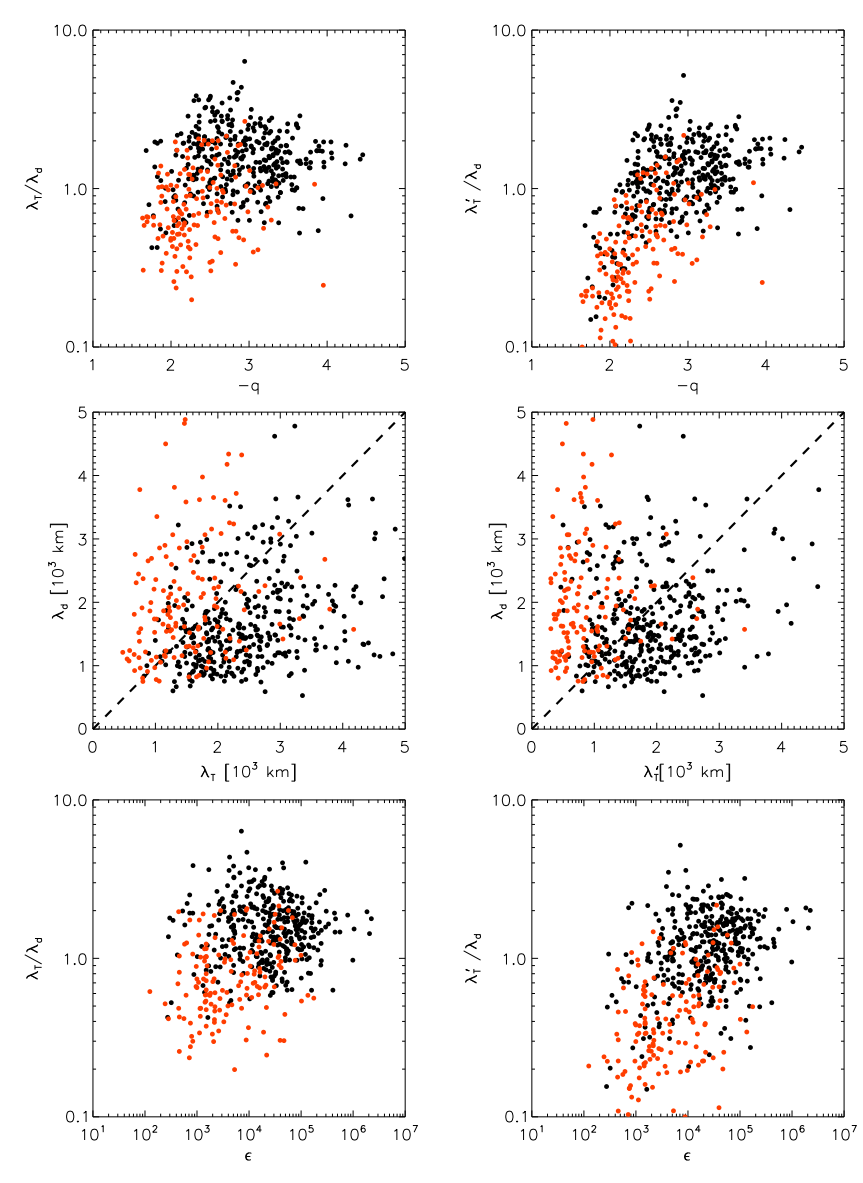


Figure 7. The left column shows the plots before applying the correction ratio to the Taylor microscale λ_T , and the right column shows the Taylor microscale (λ'_T) after applying correction ratio.

points appear to be equally scattered. The right column of Figure 7 shows the values of λ'_T , after the application of the correction ratio. After the corrections, we can see that the majority of the black points have $\lambda'_T > \lambda_d$ for q < -3, and the red points have $\lambda'_T < \lambda_d$ for q > -3. This indicates a hydrodynamics type of plasma for open magnetic field case and nonhydrodynamics in the magnetic cloud cases. Further discussion of this analysis is found in *Matthaeus et al.* [2008], where it is argued that the difference in the behavior of these cases points to a difference in relative importance of dissipative processes at ion and electron scales.

4. Conclusions

We have demonstrated a refined technique of calculating the Taylor microscale from a discrete times series by computing correlation functions from structure functions. The method that we employed is based on the definition of the Taylor microscale. To verify this technique we analyze a synthetic time series derived from a defined power density spectrum. We are able to reproduce the Taylor scale values with our technique after applying a correction term, which improves our estimate of the Taylor microscale, estimated from a Richardson extrapolation technique [see *Weygand et al.*, 2009]. In addition, we studied the effects of the dissipation range spectral index and the time resolution of the simulated data. Moreover, we show an example of the



application of the technique to solar wind magnetic field data [Matthaeus et al., 2005, 2008]. This technique is expected to be useful for extracting refined estimates of the Taylor microscale from experimental and observational turbulence data in solar wind and other astrophysical contexts.

Acknowledgments

P. Chuychai was supported by Thailand Research Fund and Thailand's Commission on Higher Education, Ministry of Education (MRG 5286239). J.M. Weygand was partially supported by NSF SHINE: NSF AGS-1155841 and NASA Heliophysics Guest Investigator program NNX09AG31G. W.H. Matthaeus was partially supported by NSF SHINE AGS-1156094 and NASA under the Heliopsheric GI program NNX09AG31G and the Solar Probe Plus project and the Magnetosphere Multiscale project. C.W. Smith is supported by the Advanced Composition Explorer mission. S.D. acknowledges partial support by the Argentinean grant UBACyT 20020120100220 (UBA).

Philippa Browning thanks D. Roberts and an anonymous reviewer for their assistance in evaluating this paper.

References

- Alexandrova, O., J. Saur, C. Lacombe, A. Mangeney, J. Mltchell, S. J. Schwartz, and P. Robert (2009), Universality of solar-wind turbulent spectrum from MHD to electron scales, *Phys. Rev. Lett.*, 103, 165,003.
- Batchelor, G. K. (1970), Theory of Homogeneous Turbulence, Cambridge Univ. Press, Cambridge, U. K.
- Dahlquist, G., and A. Bjorck (2003), Numerical Methods, Courier Dover Publications, Mineola, New York, Prentice-Hall 1974.
- Dasso, S., W. H. Matthaeus, J. M. Weygand, P. Chuychai, L. J. Milano, C. W. Smith, and M. G. Kivelson (2008), ACE/Wind multispacecraft analysis of the magnetic correlation in the solar wind, in *Proceedings of the 30th International Cosmic Ray Conference. July 3–11, 2007, Mérida, Yucatán, Mexico*, vol. 1, edited by R. Caballero et al., pp. 625–628, Universidad Nacional Autónoma de México, Mexico City, Mexico
- Gary, S. P., and J. E. Borovsky (2004), Alfvén-cyclotron fluctuations: Linear Vlasov theory, J. Geophys. Res., 109, 6105, doi:10.1029/2004JA010399.
- Gurgiolo, C., M. L. Goldstein, W. H. Matthaeus, A. Vinas, and A. N. Fazakerley (2013), Characteristics of the Taylor microscale in the solar wind/foreshock: Magnetic field and electron velocity measurements, *Ann. Geophys.*, 31, 2063, doi:10.5194/angeo-31-2063-2013.
- Hamilton, K., C. W. Smith, B. J. Vasquez, and R. J. Leamon (2008), Anisotropies and helicities in the solar wind inertial and dissipation ranges at 1 AU, *J. Geophys. Res.*, 113, A01106, doi:10.1029/2007JA012559.
- Hinze, J. O. (1975), Turbulence, McGraw-Hill, New York.
- Leamon, R. J., W. H. Matthaeus, and C. W. Smith (1998), Contribution of cyclotron-resonant damping to kinetic dissipation of interplanetary turbulence, *Astrophys. J., 507*, L181, doi:10.1086/311698.
- Matthaeus, W. H., and M. L. Goldstein (1982), Stationarity of magnetohydrodynamic fluctuations in the solar wind, J. Geophys. Res., 87, 10.347–10.354.
- Matthaeus, W. H., S. Dasso, J. M. Weygand, L. J. Milano, C. W. Smith, and M. G. Kivelson (2005), Spatial correlation of solar-wind turbulence from two-point measurements, *Phys. Rev. Lett.*, *95*, 231,101, doi:10.1103/PhysRevLett.95.231101.
- Matthaeus, W. H., J. M. Weygand, P. Chuychai, S. Dasso, C. W. Smith, and M. Kivelson (2008), Interplanetary magnetic Taylor microscale and implications for plasma dissipation, *Astrophys. J.*, 678, L141, doi:10.1086/588525.
- Sahraoui, F., M. L. Goldstein, P. Robert, and Y. V. Khotyaintsev (2009), Evidence of a cascade and dissipation of solar-wind turbulence at the electron gyroscale, *Phys. Rev. Lett.*, 102, 231,102, doi:10.1103/PhysRevLett.102.231102.
- Smith, C. W., K. Hamilton, J. Vasquez, and R. J. Leamon (2006a), Dependence of the dissipation range spectrum of interplanetary magnetic fluctuations on the rate of energy cascade, *Astrophys. J.*, 645, L85, doi:10.1086/506151.
- Smith, C. W., B. J. Vasquez, and K. Hamilton (2006b), Interplanetary magnetic fluctuation anisotropy in the inertial range, *J. Geophys. Res.*, 111, A09111, doi:10.1029/2006JA011651.
- Taylor, G. I. (1938), The spectrum of turbulence, Proc. R. Soc. London, Ser. A, 164, 476–490.
- Weygand, J. M., W. H. Matthaeus, S. Dasso, M. G. Kivelson, and R. J. Walker (2007), Taylor scale and effective magnetic Reynolds number determination from plasma sheet and solar wind magnetic field fluctuations, *J. Geophys. Res.*, 112, A10201, doi:10.1029/2007JA012486.
- Weygand, J. M., W. H. Matthaeus, S. Dasso, M. G. Kivelson, L. M. Kristler, and C. Mouikis (2009), Anisotropy of the Taylor scale and the correlation scale in plasma sheet and solar wind magnetic field fluctuations, *J. Geophys. Res.*, 114, A07213, doi:10.1029/2008JA013766.
- Weygand, J. M., W. H. Matthaeus, M. El-Alaoui, S. Dasso, and M. G. Kivelson (2010), Anisotropy of the Taylor scale and the correlation scale in plasma sheet magnetic field fluctuations as a function of auroral electrojet activity, *J. Geophys. Res.*, 115, A12250, doi:10.1029/2010JA015499.
- Weygand, J. M., W. H. Matthaeus, S. Dasso, and M. G. Kivelson (2011), Correlation and Taylor scale variability in the interplanetary magnetic field fluctuations as a function of solar wind speed, J. Geophys. Res., 116, A08102, doi:10.1029/2011JA016621.

เอกสารแนบหมายเลข 2

RANDOM BALLISTIC INTERPRETATION OF NONLINEAR GUIDING CENTER THEORY

D. Ruffolo^{1,2}, T. Pianpanit¹, W. H. Matthaeus³, and P. Chuychai^{2,4}

Department of Physics, Faculty of Science, Mahidol University, Bangkok 10400, Thailand; scdjr@mahidol.ac.th, th_ee@hotmail.com

² Thailand Center of Excellence in Physics, CHE, Ministry of Education, Bangkok 10400, Thailand

Bartol Research Institute and Department of Physics and Astronomy, University of Delaware, Newark, DE 19716, USA; yswhm@bartol.udel.edu

⁴ School of Science, Mae Fah Luang University, Chiang Rai 57100, Thailand; p.chuychai@sci.mfu.ac.th

Received 2012 January 12; accepted 2012 February 8; published 2012 February 22

ABSTRACT

Nonlinear guiding center (NLGC) theory has been used to explain the asymptotic perpendicular diffusion coefficient κ_{\perp} of energetic charged particles in a turbulent magnetic field, which can be applied to better understand cosmic ray transport. Here we re-derive NLGC, replacing the assumption of diffusive decorrelation with random ballistic decorrelation (RBD), which yields an explicit formula for κ_{\perp} . We note that scattering processes can cause a reversal of the guiding center motion along the field line, i.e., "backtracking," leading to partial cancellation of contributions to κ_{\perp} , especially for low-wavenumber components of the magnetic turbulence. We therefore include a heuristic backtracking correction (BC) that can be used in combination with RBD. In comparison with computer simulation results for various cases, NLGC with RBD and BC provides a substantially improved characterization of the perpendicular diffusion coefficient for a fluctuation amplitude less than or equal to the large-scale magnetic field.

Key words: diffusion - magnetic fields - turbulence

1. INTRODUCTION

While charged particles subject to a magnetic field in a tenuous plasma will mainly gyrate along that field, magnetic turbulence can cause particles to also spread in the directions perpendicular to the large-scale field. Such perpendicular transport involves an interesting interplay between the transport along field lines, the random walk of magnetic field lines perpendicular to the large-scale field direction, and true cross-field transport in which the particle guiding center eventually separates from its original field line.

The classic FLRW theory (Jokipii 1966), in which particles follow magnetic field lines with a fixed pitch angle, directly related the perpendicular diffusion coefficient κ_{\perp} to the field line diffusion coefficient D. Meanwhile another viewpoint in terms of scattering led to a relation between κ_{\perp} and the parallel diffusion coefficient κ_{\parallel} (Axford 1965; Gleeson 1969). Nonlinear guiding center (NLGC) theory (Matthaeus et al. 2003) successfully accounted for both factors, allowing the guiding center motion to decorrelate due to both parallel (pitchangle) scattering and the random walk of the guiding magnetic field line, for transverse magnetic fluctuations with a general power spectrum. This theory has provided a much closer match to observations (Bieber et al. 2004) and computer simulation results for κ_{\perp} (see also Minnie et al. 2007; Ruffolo et al. 2008), and its framework has attracted theoretical interest and inspired numerous related theories (e.g., Shalchi et al. 2004, 2006; le Roux & Webb 2007; Qin 2007; Shalchi 2010).

The original NLGC theory (Matthaeus et al. 2003) used the Taylor–Green–Kubo (TGK) formula (Taylor 1922; Green 1951; Kubo 1957)

$$\kappa_{xx} \equiv \lim_{t \to \infty} \frac{\langle \Delta x^2 \rangle}{2t} = \int_0^\infty \langle \tilde{v}_x(0) \tilde{v}_x(t) \rangle dt \tag{1}$$

for the asymptotic particle diffusion coefficient κ_{xx} along a coordinate x perpendicular to the large-scale magnetic field direction z, based on the guiding center velocity $\tilde{\mathbf{v}}$.

That work used

$$\langle \tilde{v}_x(0)\tilde{v}_x(t)\rangle \approx \frac{a^2}{B_0^2} \langle v_z(0)v_z(t)\rangle \langle b_x(0,0)b_x[\mathbf{x}(t),t]\rangle,$$
 (2)

for the displacement $\mathbf{x}(t)$ of the particle guiding center trajectory in a large-scale magnetic field $B_0\mathbf{\hat{z}}$. The authors set $a^2=1/3$, a factor which effectively accounts for the replacement of \tilde{v}_z with the particle velocity v_z in the correlations. Then the Lagrangian correlation $\langle b_x(0,0)b_x[\mathbf{x}(t),t]\rangle$ was evaluated in terms of the Eulerian correlation function and power spectrum by using Corrsin's independence hypothesis (Corrsin 1959) and setting the displacement distribution to that for asymptotic diffusion (Salu & Montgomery 1977), leading to an implicit formula for κ_\perp in terms of input values of κ_{zz} and the power spectrum of magnetic fluctuations. A related approach was previously used to derive a field line diffusion coefficient (Matthaeus et al. 1995) that is reasonably close to values from direct computer simulations (Gray et al. 1996; Ghilea et al. 2011).

In the present work, we consider an alternate interpretation of NLGC that replaces the diffusive distribution of guiding center trajectories with a random ballistic distribution, for the purpose of calculating the Lagrangian magnetic correlation function $\langle b_x(0,0)b_x[\mathbf{x}(t),t]\rangle$. This approach was recently introduced for calculating the field line diffusion coefficient and led to some substantial improvements in the match with direct simulation results (Ghilea et al. 2011). It is analogous to concepts in random walk theory in which the mean free path is determined by the extent of ballistic motion between scattering events. In this context, note that \tilde{v}_x decorrelates over the decorrelation scale of v_z or b_x , whichever is shorter. This implies that the decorrelation of \tilde{v}_x in the TGK integral (which determines κ_{xx}) takes place over a distance scale for which the parallel motion is approximately constant and the field lines are approximately straight, so the guiding center motion can be treated as ballistic in random directions determined by the distribution of magnetic field directions (Figure 1). (As illustrated in the figure, at longer times the guiding center velocity will change, the particle will reverse its direction along B, and the particle will depart from its original guiding field line.) We demonstrate that this

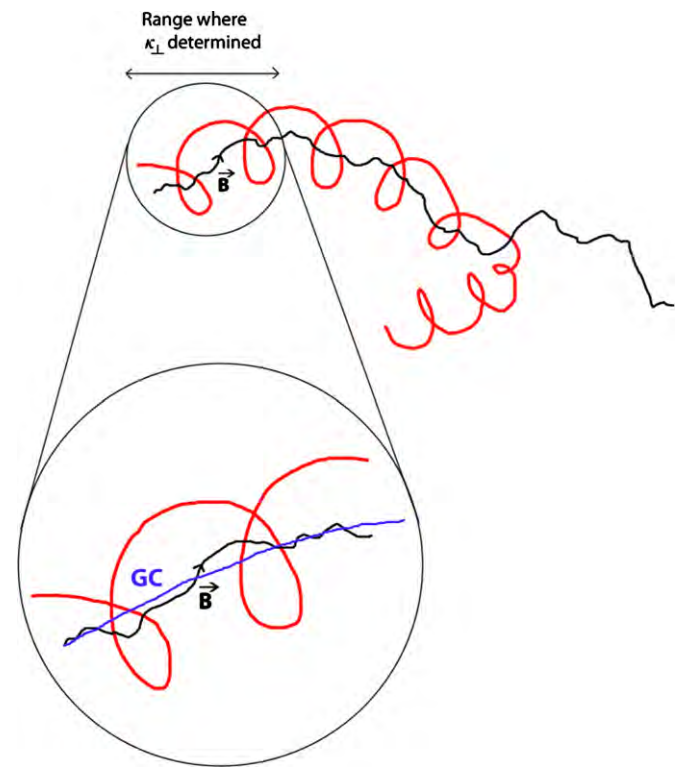


Figure 1. Illustration of the random ballistic interpretation of nonlinear guiding center (NLGC) theory. The diffusion coefficient κ_{\perp} of energetic charged particle motion (red line) perpendicular to the large-scale magnetic field is related to the decorrelation (i.e., change in direction) of a perpendicular component of the guiding center velocity (GC, blue line), which roughly follows a local magnetic field line (black line). Over the relevant distance scale, the guiding center motion can be approximated as ballistic (i.e., with constant velocity) along random directions distributed like the magnetic field directions. Such random ballistic decorrelation (RBD) is determined using the framework of NLGC theory, including the effects of the field line random walk and the parallel scattering of particle trajectories.

approach, together with a backtracking correction (BC), leads to a substantial improvement in the match with direct computer simulations of the perpendicular diffusion of energetic charged particles.

2. RANDOM BALLISTIC DECORRELATION

We consider the application of Corrsin's independence hypothesis (described below) assuming a Gaussian distribution of displacements, where diffusive decorrelation (DD) or random ballistic decorrelation (RBD) is used to describe the variance σ_i^2 along each direction. DD considers that the asymptotic diffusion also governs the displacement distribution at early times during the decorrelation process, so $\sigma_i^2 = 2\kappa_{ii}t$, while RBD assumes the decorrelation is determined by ballistic motion of guiding centers at early times in random directions, at guiding center velocity $\tilde{\mathbf{v}}$, depending on the fluctuating magnetic field, with $\sigma_i^2 = \langle \tilde{v}_i^2 \rangle t^2$.

Let us assume axisymmetry, define the fluctuation amplitude b so that $b^2 = \langle b_x^2 + b_y^2 \rangle = 2 \langle b_x^2 \rangle$, and define v_s as the particle velocity along the local magnetic field. As a special case of Equation (2) for t = 0, we use

$$\langle \tilde{v}_x^2 \rangle = \langle \tilde{v}_y^2 \rangle \approx \frac{a^2}{B_0^2} \langle v_z^2 \rangle \langle b_x^2 \rangle = \frac{a^2 v^2}{6} \frac{b^2}{B_0^2}, \tag{3}$$

where we use $\langle v_z^2 \rangle = v^2/3$ for an isotropic distribution of particle velocities. We also use $\langle \tilde{v}^2 \rangle = v^2/3$ to obtain

$$\langle \tilde{v}_z^2 \rangle = \frac{v^2}{3} \left(1 - a^2 \frac{b^2}{B_0^2} \right).$$
 (4)

Note that for $b/B_0 > a^{-1} = \sqrt{3}$, Equation (4) gives a non-sensical negative value for $\langle \hat{v}_z^2 \rangle$. Thus, we will consider this RBD approach to be limited to $b/B_0 \leqslant \sqrt{3}$. Note that the NLGC framework in general is also limited to magnetic fluctuation amplitudes that are not too great, in the sense that NLGC assumes transverse fluctuations, and if $b \gg B_0$ one would not expect the (weak) mean magnetic field to force the fluctuations to be strongly transverse.

As in the original derivation of NLGC, we use Equations (1) and (2), with $\langle v_z(0)v_z(t)\rangle = (v^2/3)e^{-t/\tau}$ for a pitch-angle scattering time τ , to obtain

$$\kappa_{xx} = \frac{a^2 v^2}{3B_0^2} \int_0^\infty e^{-t/\tau} \langle b_x(0,0)b_x[\mathbf{x}(t),t] \rangle dt.$$
 (5)

We then make use of Corrsin's independence hypothesis to relate the Lagrangian correlation $\langle b_x(0,0)b_x[\mathbf{x}(t),t]\rangle$ to the Eulerian correlation function R_{xx} and the probability of displacement \mathbf{x} at time t, so that

$$\kappa_{xx} = \frac{a^2 v^2}{3B_0^2} \int_0^\infty e^{-t/\tau} \int R_{xx}(\mathbf{x}, t) P(\mathbf{x}|t) d\mathbf{x} dt.$$
 (6)

Following Matthaeus et al. (2003), we use the Fourier transform of the correlation function $R_{xx}(\mathbf{x}, t)$ as the power spectrum $S_{xx}(\mathbf{k}, t) = S_{xx}(\mathbf{k})e^{-\gamma(\mathbf{k})t}$ and assume independent guiding center displacement probability distributions along each coordinate to obtain

$$\kappa_{xx} = \frac{a^2 v^2}{3B_0^2} \int_0^\infty e^{-t/\tau} \int S_{xx}(\mathbf{k}) e^{-\gamma(\mathbf{k})t} \left(\int_{-\infty}^\infty e^{-ik_x x} P(x|t) dx \right) \\
\times \left(\int_{-\infty}^\infty e^{-ik_y y} P(y|t) dy \right) \left(\int_{-\infty}^\infty e^{-ik_z z} P(z|t) dz \right) d\mathbf{k} dt. \tag{7}$$

For a Gaussian displacement distribution P(x|t), we have (Ghilea et al. 2011)

$$\int_{-\infty}^{\infty} e^{-ik_x x} P(x|t) dx = \exp\left(-\frac{1}{2}k_x^2 \sigma_x^2\right)$$
 (8)

and analogous formulas for y and z. For RBD we use $\sigma_i^2 = \langle \tilde{v}_i^2 \rangle t^2$, and substituting Equation (8) into Equation (7) yields

$$\kappa_{xx} = \frac{a^2 v^2}{3B_0^2} \int S_{xx}(\mathbf{k}) T(\mathbf{k}) d\mathbf{k}, \tag{9}$$

where the mean free time $T(\mathbf{k})$ is given by

$$T(\mathbf{k}) = \int_0^\infty \exp\left[-\frac{t}{\tau} - \gamma(\mathbf{k})t - \frac{1}{2}\sum_i k_i^2 \langle \tilde{v}_i^2 \rangle t^2\right] dt. \quad (10)$$

Performing the *t*-integration and using $1/\tau = v/\lambda_{\parallel} = v^2/(3\kappa_{zz})$, we obtain

$$T(\mathbf{k}) = \sqrt{\frac{\pi}{2}} \frac{e^{\alpha^2} \operatorname{erfc}(\alpha)}{\sqrt{\sum_i k_i^2 \langle \tilde{v}_i^2 \rangle}}$$
(11)

and

$$\kappa_{xx} = \frac{a^2 v^2}{3B_0^2} \sqrt{\frac{\pi}{2}} \int \frac{S_{xx}(\mathbf{k})}{\sqrt{\sum_i k_i^2 \langle \tilde{v}_i^2 \rangle}} e^{\alpha^2} \operatorname{erfc}(\alpha) d\mathbf{k}$$
 (RBD), (12)

where

$$\alpha \equiv \frac{v^2/(3\kappa_{zz}) + \gamma(\mathbf{k})}{\sqrt{2\sum_i k_i^2 \langle \tilde{v}_i^2 \rangle}}$$
(13)

and the expressions for $\langle \tilde{v}_i^2 \rangle$ are given by Equations (3) and (4). Note that the original DD interpretation of Matthaeus et al. (2003) used the formula for asymptotic diffusion with κ_{xx} in the displacement distribution, yielding an implicit equation for κ_{xx} . In contrast, the RBD theory uses a predetermined random ballistic formula for the displacement distribution and yields an explicit formula for κ_{xx} , as in analogous theories for the field line diffusion coefficient (Ghilea et al. 2011). For numerical evaluation, NLGC-type theories based on DD typically require an iterative solution, whereas NLGC/RBD can be evaluated without iteration.

3. BACKTRACKING CORRECTION

Previous simulations have shown that the perpendicular transport of energetic charged particles is characterized by ballistic (free-streaming) guiding center motion at short times, followed by subdiffusion (Qin et al. 2002a) and later, if the fluctuations have sufficient transverse complexity, by asymptotic diffusion (Qin et al. 2002b). This subdiffusion is due to a parallel (pitchangle) scattering process that causes a particle to reverse its motion along the local field line and partially retrace its steps. Such "backtracking" leads to a negative v_x -correlation function over a certain time range, hence the reduction in the running perpendicular diffusion coefficient. In some cases this leads to subdiffusion (see Qin et al. 2002b and Section 4 of Ruffolo et al. 2008).

Backtracking was inherent in the original NLGC/DD theory (Matthaeus et al. 2003). The use of diffusive displacements means that the displacements for which the correlation function is sampled can undergo a random walk, including backtracking. It was assumed that backtracking did not completely cancel out the perpendicular guiding center excursions due to other physical effects. This is not the case for the RBD calculation, which is based on ballistic guiding center trajectories.

For RBD theory, we note that Equations (9) and (10) assign a mean free time $T(\mathbf{k})$ to individual **k**-components of the turbulence, which are averaged with weighting according to the power spectrum, to determine κ_{xx} . Conceptually this relates to the v_z - b_x independence hypothesis of Matthaeus et al. (2003). For magnetostatic fluctuations with $\gamma = 0$, Equation (11) gives $T \approx \tau$ for low k and t decreases for higher t. Thus, for modes of low t, the mean free time is determined by the parallel scattering, whereas for higher t it is determined by the field line random walk.

This random ballistic calculation of the mean free time does not account for backtracking. Consider low k, for which the decorrelation in Equation (10) is dominated by the scattering term (first term in the exponential) while \mathbf{b} is nearly constant. Then the perpendicular displacement associated with $T(\mathbf{k})$ will be largely canceled out by subsequent backtracking. A similar effect leads to subdiffusion in simulation results (i.e., running κ_{xx} decreases with increasing t) for fluctuations with insufficient transverse complexity (Qin et al. 2002a), whereas NLGC yields

a much larger asymptotic value of κ_{xx} (see Run 12 of Ruffolo et al. 2008).

Therefore, we introduce a heuristic BC for RBD that reduces the influence of such low-k modes by reducing $T(\mathbf{k})$ and therefore their contribution to the overall κ_{xx} . We multiply $T(\mathbf{k})$ by $e^{-\alpha^2}$, which simplifies Equation (11) to yield

$$T(\mathbf{k}) = \sqrt{\frac{\pi}{2}} \frac{\operatorname{erfc}(\alpha)}{\sqrt{\sum_{i} k_{i}^{2} \langle \tilde{v}_{i}^{2} \rangle}}$$
(14)

and

$$\kappa_{xx} = \frac{a^2 v^2}{3B_0^2} \sqrt{\frac{\pi}{2}} \int \frac{S_{xx}(\mathbf{k})}{\sqrt{\sum_i k_i^2 \langle \tilde{v}_i^2 \rangle}}$$

$$\times \operatorname{erfc} \left[\frac{v^2 / (3\kappa_{zz}) + \gamma(\mathbf{k})}{\sqrt{2\sum_i k_i^2 \langle \tilde{v}_i^2 \rangle}} \right] d\mathbf{k} \quad (RBD/BC). \quad (15)$$

This BC is related to the terms that are linear and quadratic in t, in the exponential of Equation (10). Here, $e^{-\alpha^2}$ serves as a simple "switch" that is close to 0 when k is sufficiently low that the linear term dominates, suggesting a strong effect of backtracking, while it approaches 1 for higher k. Note also that for a given \mathbf{k} , there is a time t when the linear and quadratic terms are equal, i.e., the field line random walk becomes important. At that time we have $t/\tau \sim \alpha^2$, and substitution into the parallel velocity correlation term $e^{-t/\tau}$ suggests the use of $e^{-\alpha^2}$ to account for backtracking effects.

4. NUMERICAL EVALUATION OF ANALYTIC THEORIES USING 2D+slab TURBULENCE

To numerically evaluate analytic theories for comparison with computer simulation results, we need to specify the power spectrum. We employ a two-component 2D+slab model of transverse magnetic fluctuations in which the power spectrum is a sum of a two-dimensional (2D) power spectrum, depending on k_x and k_y , and a slab power spectrum depending on k_z . The latter represents parallel Alfvénic fluctuations and the former idealizes the quasi-2D structures, including "flux tubes," that can develop from interactions of such waves (Shebalin et al. 1983; see also Borovsky 2008; Seripienlert et al. 2010; and references therein). The two-component model was motivated by observations of interplanetary magnetic fluctuations, indicating quasi-slab and quasi-2D components (Matthaeus et al. 1990; Weygand et al. 2009), which can be modeled using a ratio of slab:2D fluctuation energies of approximately 20:80 (Bieber et al. 1994, 1996). This model has provided a useful description of the parallel transport of particles in the inner heliosphere (Bieber et al. 1994), and was used by most studies that implemented and/or tested NLGC

For the special case of 2D+slab fluctuations, Equations (12) and (15) and their DD equivalent split into two terms using S_{xx}^{slab} and S_{xx}^{2D} . However, Shalchi (2006) has proposed that the direct contribution of slab fluctuations to the perpendicular transport should be subdiffusive, and that the S_{xx}^{slab} term should not be included in the equation of κ_{\perp} . (Note that slab fluctuations can still play a role as a key determinant of λ_{\parallel} , which enters into the 2D contribution.) We refer to this proposal as the Shalchi slab hypothesis. We employ this in the present work, and a detailed evaluation of its accuracy will be presented in a future publication (D. Ruffolo et al., in preparation).

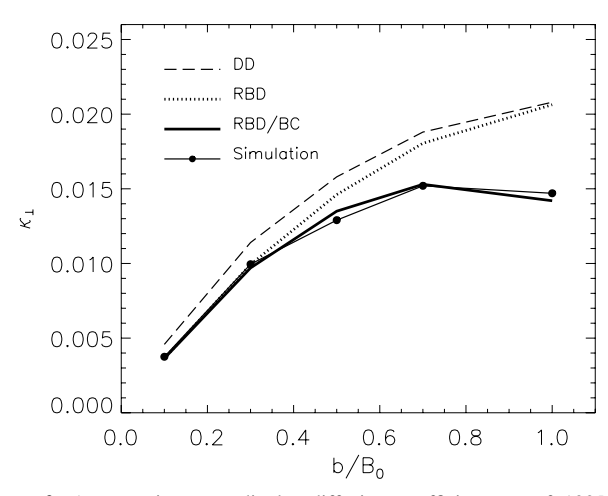


Figure 2. Asymptotic perpendicular diffusion coefficient κ_{\perp} of 100 MeV protons in 2D+slab turbulence with a slab fraction $f_s = 0.2$ as a function of the magnetic fluctuation amplitude b/B_0 . Using the NLGC framework, random ballistic decorrelation with backtracking correction (RBD/BC, thick line) provides a closer match with computer simulation results (solid circles) than the original DD theory (long-dashed line) and uncorrected RBD (short-dashed line). In the present work we also employ the Shalchi slab hypothesis (Shalchi 2006).

Therefore, when using the 2D+slab model of magnetic turbulence, in Equation (12) or Equation (15) we include only the 2D portion of the power spectrum, which is concentrated at $k_z = 0$. We also assume the fluctuations to be magnetostatic, with $\gamma = 0$, and axisymmetric. For RBD without the BC, we have

$$\kappa_{xx} = \frac{a^2 v^2}{3B_0^2} \sqrt{\frac{\pi}{2}} \int_{-\infty}^{\infty} \int_{-\infty}^{\infty} \times \frac{S_{xx}^{\text{2D}}(k_x, k_y)}{k_{\perp} \sqrt{\langle \tilde{v}_x^2 \rangle}} e^{\alpha^2} \operatorname{erfc}(\alpha) dk_x dk_y \qquad \text{(RBD)}, \quad (16)$$

and with the BC we have

$$\kappa_{xx} = \frac{a^2 v^2}{3B_0^2} \sqrt{\frac{\pi}{2}} \int_{-\infty}^{\infty} \int_{-\infty}^{\infty} \times \frac{S_{xx}^{\text{2D}}(k_x, k_y)}{k_{\perp} \sqrt{\langle \tilde{v}_x^2 \rangle}} \operatorname{erfc}(\alpha) dk_x dk_y \qquad \text{(RBD/BC)}, \quad (17)$$

where

$$\alpha = \frac{v^2}{3\kappa_{zz}k_{\perp}\sqrt{2\langle\tilde{v}_x^2\rangle}}\tag{18}$$

and $k_{\perp}^2 = k_x^2 + k_y^2$.

For comparison, we also consider the original DD theory, and for our model assumptions we obtain

$$\kappa_{xx} = \frac{a^2 v^2}{3B_0^2} \int_{-\infty}^{\infty} \int_{-\infty}^{\infty} \frac{S_{xx}^{\text{2D}}(k_x, k_y) dk_x dk_y}{v^2 / (3\kappa_{zz}) + k_\perp^2 \kappa_{xx}}$$
(DD). (19)

The analytic theory expressions were evaluated numerically using the MATHEMATICA program (Wolfram Research, Inc.) to perform continuous **k**-space integrals. For the input value of κ_{zz} , we used the simulation value.

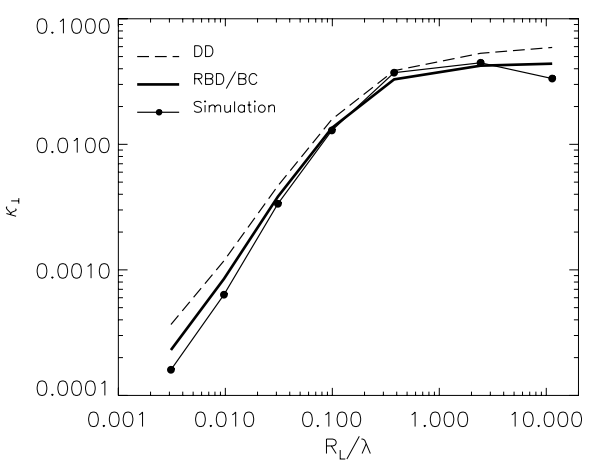


Figure 3. Asymptotic perpendicular diffusion coefficient κ_{\perp} in 2D+slab turbulence with $f_s = 0.2$ and $b/B_0 = 0.5$ as a function of the proton gyroradius in units of the turbulence bendover scale. The simulation values shown here (solid circles) correspond to proton energies ranging from 0.1 MeV to 50 GeV for $B_0 = 5$ nT and $\lambda = 0.02$ AU. In most cases, the RBD/BC theory (thick line) provides a better explanation of the computer simulation results (solid circles) than the original DD theory (dashed line).

5. COMPARISON WITH COMPUTER SIMULATIONS

We have also performed direct computer simulations to trace particle orbits in 2D+slab magnetic turbulence. While the simulations inevitably involve some discretization and statistical errors, they do avoid key assumptions of the analytic work, and thus provide an independent check of their validity.

The computer simulations were performed using the methods, power spectra, and parameter values described by Ruffolo et al. (2008). In particular, all distances are in units of $\lambda = 0.02$ AU, the slab and 2D turbulence bendover scale, ⁵ and velocities are in units of the speed of light c. Simulations were performed over a sufficient time for all κ_{ii} to approach asymptotic values, within statistical errors. We assume axisymmetry about the large-scale field direction, so κ_{xx} and κ_{yy} should be the same within statistical errors, which we verified in all cases. We report $\kappa_{\perp} \equiv (\kappa_{xx} + \kappa_{yy})/2$, which can be compared directly with κ_{xx} from theories. In some contexts, we use κ_{\perp} as a synonym for κ_{xx} .

Figure 2 shows the dependence of κ_{\perp} (in units of $c\lambda$) on the overall fluctuation amplitude b/B_0 , using $f_s \equiv b_{\rm slab}^2/(b_{\rm slab}^2 + b_{\rm 2D}^2) = 0.2$. It is apparent that the RBD/BC version (thick lines) agrees with computer simulation results (solid circles) better and over a wider range of b/B_0 values than either the DD theory (long-dashed lines) or RBD without the BC (short-dashed lines), over the range of applicability of RBD ($b/B_0 \le 1/a = \sqrt{3}$). We have also examined the dependence on the proton gyroradius (Figure 3), which is related to its energy, for fixed $f_s = 0.2$ and $b/B_0 = 0.5$. The seven simulations were for protons of kinetic energy 0.1, 1, 10, and 100 MeV as well as 1, 10, and 50 GeV. The RBD results, not shown, nearly match DD at $R_L/\lambda < 1$, nearly match RBD/BC at $R_L/\lambda > 1$, and are intermediate at $R_L/\lambda \approx 1$. Overall, the RBD/BC theory again provides the best explanation of the computer simulation results.

⁵ Ruffolo et al. (2008) incorrectly specified $\lambda = 0.027$ AU; their simulations actually used $\lambda = 0.02$ AU, and calculations were performed for the same parameters as the simulations.

6. DISCUSSION

In the present work, we interpret NLGC theory in terms of particle guiding center trajectories that are ballistic with constant velocity over the distance scale leading up to their decorrelation (Figure 1), a standard assumption in random walk theory based on scattering concepts. Such RBD stands in contrast to the previous assumption of DD in which the displacements were taken to spread according to asymptotic diffusion. The use of Corrsin's hypothesis for RBD is similar in spirit to a Fokker-Planck approach in which the unperturbed trajectory has a constant but random velocity whose directional distribution is related to the distribution of magnetic fluctuations. It is also related to the Langevin-equation approaches of Balescu et al. (1994). Our use of a heuristic BC that is specific to RBD leads to a substantial improvement in the match with direct computer simulation results, compared with DD and RBD without BC.

Note that RBD theory does not require a small fluctuation amplitude, and indeed RBD/BC matches computer simulation results very well for amplitudes up to $b/B_0 \sim 1$ (Figure 2). The inapplicability for $b/B_0 > 1/a = \sqrt{3}$ indicates room for future improvements to obtain a truly non-perturbative theory. At the same time, we should note that the NLGC framework treats only transverse magnetic fluctuations. In the interplanetary medium of the inner heliosphere, transverse fluctuations account for $\sim 90\%$ of the magnetic fluctuation energy (Belcher & Davis 1971), so NLGC is well justified in this case. However, for large amplitudes with $b/B_0 \gg 1$ there is little reason for the fluctuations to be so strongly anisotropic, and the NLGC framework itself may have limited applicability.

Considering the dependence of κ_{\perp} on the proton Larmor radius, R_L , as shown in Figure 3, a discrepancy remains between NLGC theory and simulation results for the two lowest energies, 0.1 and 1 MeV. The discrepancy is substantially reduced for RBD/BC. For energies of 10 MeV to 10 GeV (i.e., $R_L/\lambda = 0.031-2.4$), RBD/BC theory matches the simulation results very well. The increase with R_L/λ saturates in this range because κ_{\perp} is roughly proportional to v (Minnie et al. 2009), which saturates at c.

The NLGC framework in general could break down when $R_L/\lambda \gg 1$. In this weak scattering limit NLGC considers that guiding center motion tracks the local field line random walk, whereas such a large gyroradius implies that particles experience fluctuations independent from those at the guiding center, and low-wavelength fluctuations should have less influence on perpendicular diffusion when they are averaged over such a large gyroradius. In the interplanetary magnetic field near Earth of about 5 nT with $\lambda \sim 0.02$ AU (Jokipii & Coleman 1968), we have $R_L \sim \lambda$ for a proton energy of about 4 GeV, and in the local galactic magnetic field of about 0.4 nT (Opher et al. 2009), where $\lambda \sim 100$ pc (Armstrong et al. 1995; Dyson & Williams 1997), we have $R_L \sim \lambda$ for a proton energy of \sim 4 × 10^{17} eV.

We have searched for and found this effect at the highest proton energy considered, 50 GeV, which corresponds to $R_L/\lambda=11$ for our parameter values of $B_0=5$ nT, $b/B_0=0.5$, and $f_s=0.2$, which are applicable to the interplanetary medium near Earth. The perpendicular diffusion coefficient κ_{\perp} decreases, presumably due to cancellation of low-wavelength fluctuations

over the gyro-orbit, while all NLGC theories predict a slight increase. In any case, the above energies where $R_L \sim \lambda$ for interplanetary and interstellar propagation are sufficiently high that NLGC theories remain applicable to a wide range of cosmic ray and energetic particle transport problems.

This work was partially supported by the Development and Promotion of Science and Technology Talents Project of the Royal Thai Government, the U.S. NSF (AGS-1063439 and SHINE AGS-1156094), NASA (Heliophysics Theory NNX11AJ4G), the Solar Probe Plus/ISIS project, and the Thailand Research Fund and Thailand's Commission on Higher Education, Ministry of Education (MRG 5286239). We thank Achara Seripienlert for technical assistance.

REFERENCES

```
Armstrong, J. W., Rickett, B. J., & Spangler, S. R. 1995, ApJ, 443, 209
Axford, W. I. 1965, Planet. Space Sci., 13, 115
Balescu, R., Wang, H.-D., & Misguich, J. H. 1994, Phys. Plasmas, 1, 3826
Belcher, J. W., & Davis, L., Jr. 1971, J. Geophys. Res., 76, 3534
Bieber, J. W., Matthaeus, W. H., Shalchi, A., & Qin, G. 2004, Geophys. Res.
Bieber, J. W., Matthaeus, W. H., Smith, C. W., et al. 1994, ApJ, 420, 294
Bieber, J. W., Wanner, W., & Matthaeus, W. H. 1996, J. Geophys. Res., 101,
Borovsky, J. E. 2008, J. Geophys. Res., 113, A08110
Corrsin, S. 1959, in Atmospheric Diffusion and Air Pollution, ed. F. Frenkel &
   P. Sheppard (Advances in Geophysics, Vol. 6; New York: Academic), 161
Dyson, J. E., & Williams, D. A. (ed.) 1997, in The Graduate Series in Astronomy,
   The Physics of the Interstellar Medium (2nd ed.; Bristol: Institute of Physics
   Publishing)
Ghilea, M. C., Ruffolo, D., Chuychai, P., et al. 2011, ApJ, 741, 16
Gleeson, L. J. 1969, Planet. Space Sci., 17, 31
Gray, P. C., Pontius, D. H., Jr., & Matthaeus, W. H. 1996, Geophys. Res. Lett.,
Green, M. S. 1951, J. Chem. Phys., 19, 1036
Jokipii, J. R. 1966, ApJ, 146, 480
Jokipii, J. R., & Coleman, P. J. 1968, J. Geophys. Res., 73, 5495
Kubo, R. 1957, J. Phys. Soc. Japan, 12, 570
le Roux, J. A., & Webb, G. M. 2007, ApJ, 667, 930
Matthaeus, W. H., Goldstein, M. L., & Roberts, D. A. 1990, J. Geophys. Res.,
   95, 20673
Matthaeus, W. H., Gray, P. C., Pontius, D. H., Jr., & Bieber, J. W. 1995, Phys.
   Rev. Lett., 75, 2136
Matthaeus, W. H., Qin, G., Bieber, J. W., & Zank, G. 2003, ApJ, 590, L53
Minnie, J., Bieber, J. W., Matthaeus, W. H., & Burger, R. A. 2007, ApJ, 663,
   1049
Minnie, J., Matthaeus, W. H., Bieber, J. W., Ruffolo, D., & Burger, R. A. 2009, J.
   Geophys. Res., 114, A01102
Opher, M., Alouani Bibi, F., Toth, G., et al. 2009, Nature, 462, 1036
Qin, G. 2007, ApJ, 656, 217
Qin, G., Matthaeus, W. H., & Bieber, J. W. 2002a, Geophys. Res. Lett., 29, 7
Qin, G., Matthaeus, W. H., & Bieber, J. W. 2002b, ApJ, 578, L117
Ruffolo, D., Chuychai, P., Wongpan, P., et al. 2008, ApJ, 686, 1231
Salu, Y., & Montgomery, D. C. 1977, Phys. Fluids, 20, 1
Seripienlert, A., Ruffolo, D., Matthaeus, W. H., & Chuychai, P. 2010, ApJ, 711,
Shalchi, A. 2006, A&A, 453, L43
Shalchi, A. 2010, ApJ, 720, L127
Shalchi, A., Bieber, J. W., Matthaeus, W. H., & Qin, G. 2004, ApJ, 616, 617
Shalchi, A., Bieber, J. W., Matthaeus, W. H., & Schlickeiser, R. 2006, ApJ, 642,
Shebalin, J. V., Matthaeus, W. H., & Montgomery, D. 1983, J. Plasma Phys.,
   29, 525
Taylor, G. I. 1922, Proc. London Math. Soc. Ser. 2, 20, 196
Weygand, J. M., Matthaeus, W. H., Dasso, S., et al. 2009, J. Geophys. Res., 114,
   A07213
```